

AzTEC and Spitzer Investigations of High Redshift Submillimetre Galaxies

Stephen Flynn

2011

Cardiff University

School of Physics & Astronomy

A thesis submitted in partial fulfilment of the
requirement for the degree of Doctor of Philosophy

Declaration

This work has not previously been accepted in substance for any degree and is not concurrently submitted in candidature for any degree.

Signed (candidate)

Date

Statement 1

This thesis is being submitted in partial fulfilment of the requirements for the degree of PhD.

Signed (candidate)

Date

Statement 2

This thesis is the result of my own independent work/investigation, except where otherwise stated. Other sources are acknowledged by explicit references.

Signed (candidate)

Date

Statement 3

I hereby give consent for my thesis, if accepted, to be available for photocopying and for inter-library loan, and for the title and summary to be made available to outside organisations.

Signed (candidate)

Date

In memory of Paddy Flynn (1953-2010).
And all those satellites...

Abstract

Submillimetre galaxies are an important element in the history of the universe. There have been great advances in technology in the last ten years that have enabled deeper and more detailed investigations of these distant objects. In this thesis I describe investigations of the properties of high redshift submillimetre galaxies made using data from multiple surveys and multiple instruments. Firstly I describe the process involved in reducing AzTEC data to produce images. I then present the reduced maps and compare them, along with a source catalogue, to those produced by the AzTEC instrument team. I found both reductions produce broadly similar results with some differences that can be explained by slightly different sets of input maps. I then present an analysis of the fainter objects in one of the AzTEC fields using a stacking technique. This analysis determines the contribution Spitzer detected galaxies make to the background at 1.1mm, the redshift dependence of this contribution and the average dust mass that can be associated with it. I also describe an analysis of the flux ratios Eales et al. (2003) found using the available AzTEC data and Spitzer IRAC imaging. In the penultimate chapter I describe the frequentist identification technique I used to determine counterparts to SCUBA submillimetre sources in the CUDSS three hour field using Spitzer infrared data.

Acknowledgements

As with any large endeavour, there are quite a few people whose assistance I would like to acknowledge. Without the assistance, insights and guidance of my supervisor Prof Steve Eales, I have no doubt that this thesis would not have been completed. His patient and flexible approach to supervision provided a working environment that helped reduce the stress and pressure a PhD entails. Without his help, and the help of his red pen(s), this thesis would not be as complete as it is.

I benefited greatly from the answers Robbie Auld and Simon Dye had to questions that were regularly not as intelligent as I had initially thought they were. I would like to thank the rest of the Cardiff Galaxies group for the help and insights I gained through group meetings and presentations. Our office would not have been as productive as it was without Gwen Raymond's musical accompaniment.

The guidance my second supervisor Phil Maukoff and his former student Douglas Haig gave me in my initial attempts at reducing and using the AzTEC data were invaluable as was the advice from the AzTEC instrument team, Grant Wilson and Jayson Austermann among them. I would like to thank the staff at the Joint Astronomy Centre and at the James Clerk Maxwell Telescope for the help and assistance I received during the AzTEC observing run.

I'd like to thank Louise Winter and the rest of the admin staff for making all the paperwork as painless as possible.

Without the support and assistance I received from my parents, through long years of school and then college, I would never have gotten this far. I would like to thank, Alysia, my Aunt Margret, for finding the many spelling and grammar mistakes that managed to elude me. I'd also like to thank Alysia for putting up with me during this 'really enjoyable' writing up period.

And finally, my sister would never forgive me if I failed to mention her, so: hi Bec.

Contents

1	Introduction	1
1.1	Galaxy Formation	2
1.1.1	Submillimetre Galaxies	4
1.1.2	Luminous Infrared Galaxies	8
1.2	Submillimetre and Millimetre Sky	9
1.2.1	Bolometers	12
1.3	Submillimetre/Millimetre Resolution	13
1.4	The Cosmic Infrared Background	14
1.5	Thesis Structure	16
2	Aztec Observations	18
2.1	Introduction	18

2.1.1	SHADES	19
2.2	Observations	20
2.2.1	Fields	20
2.2.2	AzTEC and the JCMT	21
2.2.3	Mapping Strategies	22
2.2.4	Observation Details	26
2.3	Map Making	27
2.3.1	Cleaning and Calibration	28
2.3.2	Co-adding	32
2.3.3	Noise Estimation	33
2.3.4	Filtering	35
2.4	Final Maps and Sources	38
2.5	Discussion	50
3	Stacking Analysis	51
3.1	Introduction	51
3.2	Data	53
3.2.1	AzTEC Map	53

3.2.2	Spitzer Source Lists	54
3.3	Stacking Method	55
3.4	Stacking the Full Catalogue	57
3.4.1	Full Catalogue CIB Contribution	58
3.5	Stacking By Redshift	59
3.5.1	Redshift Dependence of Average Flux	60
3.5.2	CIB Contribution by Redshift	61
3.5.3	Dust-Mass	62
3.6	Summary	64
4	Flux Ratio Analysis	66
4.1	Introduction	66
4.2	Estimating Redshifts	67
4.2.1	Spectroscopic Measurement	67
4.2.2	Photometric Technique	68
4.2.3	Submm to Radio Ratio	68
4.2.4	Submm to Millimetre Ratio	69
4.2.5	Spitzer IRAC Colours	71

4.3	Abell 2125 Observations	71
4.3.1	MAMBO	71
4.3.2	SCUBA	72
4.3.3	IRAC	72
4.3.4	IRAC Image Production	73
4.3.5	Counterparts	77
4.3.6	Flux Ratios	81
4.4	Lockman Hole Observations	83
4.4.1	AzTEC	84
4.4.2	SCUBA	84
4.4.3	Flux Ratios	85
4.5	Discussion	90
5	CUDSS Source Identifications	92
5.1	Introduction	92
5.2	Observations	93
5.2.1	SCUBA Observations	93
5.2.2	Optical and Near-Infrared Observations	94

5.2.3	Spitzer IRAC Observations	95
5.3	Counterpart Identification	101
5.4	Results, All Channels	103
5.4.1	Secure IRAC detections	109
5.4.2	Comparison with C04	115
5.4.3	IDs from the IRAC data only	116
5.4.4	Photometric Redshift Analysis	116
5.5	Results, $3.6\mu\text{m}$ and $4.5\mu\text{m}$ Combined	118
5.5.1	Secure IRAC detections	121
5.5.2	Comparison with C04	130
5.5.3	IDs from the IRAC data only	131
5.6	Discussion	131
5.6.1	Individual Catalogues	131
5.6.2	Combined Catalogue	132
6	Conclusion	134
6.1	Introduction	134
6.2	AzTEC Observations and Analysis	135

6.3	Stacking Analysis	136
6.4	Eales et al. 2003; High z or Cold Dust	137
6.4.1	Lockman Hole 1.1mm Observations	138
6.4.2	Abell 2125 IRAC Observations	138
6.4.3	Unusual but not at Extreme Redshift	139
6.5	CUDSS Identifications	139
6.6	A Complex Picture	141
6.7	Future Work	141
6.7.1	1.1mm Flux Deboosting	141
6.7.2	Sample Size	142
6.7.3	IRAC Colour Analysis	143

List of Figures

1.1	The flux density as a function of redshift for different passbands . . .	6
1.2	Atmospheric transmission measured from Mauna Kea	11
1.3	The Cosmic Optical Background in blue and the Cosmic Infrared Background in Red	16
2.1	The positions of the working AzTEC bolometers	22
2.2	AzTEC scanning strategies.	24
2.3	PCA Example	29
2.4	AzTEC 1.1mm Lockman Hole (top) and SXDF (bottom) signal maps	34
2.5	AzTEC 1.1mm Lockman Hole S/N (top) and Weight (bottom) maps.	36
2.6	AzTEC 1.1mm SXDF S/N (top) and Weight (bottom) maps.	37
2.7	The Aztec Lockman Hole (top) and SXDF (bottom) signal maps. .	39
2.8	AU10 Flux Against This Reductions Flux.	49

3.1	The plots of flux produced by stacking 1.1mm flux	56
3.2	Redshift stacking postage stamps.	60
4.1	Abell 2125 3.6 μ m postage stamps	78
4.2	Abell 2125 4.5 μ m postage stamps	79
4.3	Abell 2125 8 μ m postage stamps	80
4.4	IRAC AB magnitude against the redshift	83
4.5	A histogram of the 850 μ m to 1.2mm and the 850 μ m to 1.1mm flux ratios	88
5.1	IRAC 3.6 μ m image of the CUDSS 3hr field	97
5.2	IRAC 4.5 μ m image of the CUDSS 3hr field	98
5.3	IRAC 5.8 μ m image of the CUDSS 3hr field	99
5.4	IRAC 8 μ m images of the CUDSS 3hr field	100
5.5	IRAC 3.6 μ m postage stamp images centred on the Webb et al. (2003a) SCUBA position.	104
5.6	IRAC 4.5 μ m postage stamp images centred on the Webb et al. (2003a) SCUBA position.	105
5.7	IRAC 5.8 μ m postage stamp images centred on the Webb et al. (2003a) SCUBA position.	106

5.8	IRAC $8\mu\text{m}$ postage stamp images centred on the Webb et al. (2003a)	
	SCUBA position.	106
5.9	IRAC $3.6\mu\text{m}$ postage stamp images centred on the Webb et al.	
	(2003a) SCUBA position.	120
5.10	IRAC $4.5\mu\text{m}$ postage stamp images centred on the Webb et al.	
	(2003a) SCUBA position.	122

List of Tables

2.1	LH sources with $S/N > 4.0$	41
2.2	SXDF sources with $S/N > 4.0$	43
2.3	Matched LH sources with $S/N > 4.0$	46
2.4	Matched SXDF sources with $S/N > 4.0$	48
3.1	The average 1.1mm flux values found using the full catalogues.	58
3.2	Background contribution from the full catalogue stacking.	59
3.3	Redshift stacking data.	61
3.4	The contribution to the background and dust mass within the individual redshift bins.	63
4.1	IRAC associations for SCUBA/MAMBO sources.	81
4.2	The Magnitudes of the IRAC counterparts to the Eales et al. (2003) sources.	82

4.3	Redshift estimates using $1.4\text{GHz}/1200\mu\text{m}$ and $1200\mu\text{m}/850\mu\text{m}$ flux ratios.	84
4.4	SCUBA detections with robust radio identifications	86
5.1	Counterparts to the Webb et al 2003 sources in the IRAC fields. . .	107
5.2	Multiband Photometry (AB Magnitudes) for the Redshift Analysis.	117
5.3	Photometric Redshifts for the IRAC Identifications.	119
5.4	Counterparts to the Webb et al 2003 sources in the IRAC fields. . .	123

Acronyms

2dFGRS 2dF Galaxy Redshift Survey

ACS Advanced Camera for Surveys

AGN active galactic nuclei

APEX Astronomical Point source EXtractor for MOPEX

AzTEC Astronomical Thermal Emission Camera

BLAST Balloon-borne Large-Aperture Submillimeter Telescope

BCD Basic Calibrated Data

CCD Charge Coupled Device

CDM cold dark matter

CFDF Canada-France Deep Fields

CFHT Canada-France-Hawaii Telescope

CFHT-IR Canada-France-Hawaii Telescope-Infrared

CFH12K Canada-France-Hawaii 12 Kilo-pixel

CIB Cosmic Infrared Background

CMB Cosmic Microwave Background

COB Cosmic Optical Background

COBE Cosmic Background Explorer

COSMOS Cosmic Evolution Survey

CSO Caltec Submillimeter Observatory

CUDSS Canada UK Deep Submillimetre Survey

DIRBE Diffuse Infrared Background Experiment

EGB Extragalactic Background

FJ Faber-Jackson

FIRAS Far Infrared Absolute Spectrophotometer

FIRB Far Infrared Background

FWHM full width half maximum

GNIRS GEMINI Near InfraRed Spectrography

H-ATLAS Herschel Astrophysical Terahertz Large Area Survey

HDF Hubble Deep Field

HDR High Dynamic Range

HLIRG Hyper Luminous Infrared Galaxy

HST Hubble Space Telescope

IFU Integral Field Unit

IRAC InfraRed Array Camera

IRAM Institut de Radioastronomie Millimétrique

IRAS Infrared Astronomical Satellite

JCMT James Clerk Maxwell Telescope

KS Kolmogorov-Smirnov

LH Lockman Hole

LIRG Luminous Infrared Galaxy

LMT Large Millimeter Telescope

MAMBO Max-Planck Millimeter Bolometer

MIPS Multiband Imaging Photometer for Spitzer

MOPEX MOsaicker and Point source EXtractor

NICMOS Near Infrared Camera and Multi-Object Spectrometer

NTT New Technology Telescope

PCA principle component analysis

PSD power spectral density

PWV precipitable water vapor

SCUBA Submillimetre Common User Bolometer Array

SDWFS Spitzer Deep, Wide-Field Survey

SED spectral energy distribution

SHADES SCUBA Half Degree Extragalactic Survey

SFR star formation rate

SLUGS SCUBA local universe galaxy survey

SURF SCUBA User Reduction Facility

SXDF Subaru XMM-Newton Deep Field

UH8K University of Hawaii 8 Kilo-pixel

UKIRT United Kingdom Infrared Telescope

ULIRG Ultra Luminous Infrared Galaxy

USIT UKIRT Imager-Spectrometer

VLA Very Large Array

Chapter 1

Introduction

~~Aagh! you are over-interpreting.~~

Prof. S. Eales. (2010)

The night sky presents a varied tapestry of stars, galaxies, nebulae and other phenomena that astronomy and astrophysics strive to understand. How this universe and multitude of objects in the sky developed from the big bang to the present day is a question that has had various answers over the centuries. With today's advanced telescopes and detectors, we are closer than ever to an accurate understanding of the universe around us.

This thesis will attempt to investigate some of the most distant galaxies with the aim of adding to the current understanding of them. In particular this work will focus on those that have been detected in submillimetre and millimetre surveys. These particular galaxies are thought to be some of the largest sources of young stars in the early universe.

1.1 Galaxy Formation

The established view of galaxy formation is described as the cold dark matter (CDM) hierarchical model. This model normally includes the cosmological constant (Λ) to account for the accelerating expansion of the universe and is generally referred to as the Λ CDM model. As the name suggests this model assumes that initially in the high redshift universe small galaxies formed after the epoch of re-ionisation and these progressively got larger through mergers. It incorporates the expansion of the universe along with an early inflationary phase of rapid expansion and dark matter in a non-relativistic or cold form. Baugh (2006) provides a detailed review of current hierarchical galaxy formation theory.

This theory suggests that the dark matter in the early universe initially had a slightly non-uniform distribution due to small density differences in the very early universe which can be seen in the Cosmic Microwave Background (CMB). Because of this non-uniformity the dark matter collapsed into halos. It is suggested that cold dark matter can only interact with itself and baryonic matter through the gravitational force. This gravitational influence would cause clouds of ordinary baryonic matter to form within these halos. This baryonic matter would then collapse leading to the first stars and galaxies. Through mutual gravitation the dark matter halos are thought to have merged with each other leading to the large scale structure seen in the the universe today. Through mutual gravitation the galaxies within these halos would also have collided and merged into progressively larger and larger conglomerations of stars and dust. This process would eventually leave the low redshift universe with its current galaxy distribution in the form of strings and clusters of galaxies and largely empty voids on large scales as seen in, for instance, the 2dF Galaxy Redshift Survey (2dFGRS) (Colless, 1999). Since

the dark matter only interacts through gravity, it is possible to make computer simulations of the gradual growth of this structure (For example, the Millennium Simulation (Springel et al., 2005)). One of the pieces of evidence for the model is that the simulations do produce a network of filaments and voids similar to that seen in the redshift surveys.

This model of the formation of galaxies has been shown to explain a significant proportion of the observational properties of the galaxies and phenomena seen in observations. However there are some issues with it. Giant elliptical galaxies for instance appear to predominately host old red stellar populations. If continual merging was to produce these galaxy types one would expect that new stellar populations would be produced with each merger. Studies of giant ellipticals, however, show that their stellar populations form quickly and at high redshift. Thomas et al. (2005), for instance, concluded, using absorption-line indices of 124 early type galaxies, that a significant amount of star formation in massive galaxies occurred at $z \sim 2-5$ and that elliptical galaxies may have formed by a redshift of one (or earlier for ellipticals in higher density environments). Mancone et al. (2010) found, using $3.6\mu\text{m}$ and $4.5\mu\text{m}$ luminosity functions for cluster galaxies from the Spitzer Deep, Wide-Field Survey (SDWFS), that while there may be mass assembly at high redshift ($z \gtrsim 1.3$) in massive cluster galaxies there does not appear to be similar mass assembly at lower redshifts. These factors clearly pose a problem for standard hierarchical models. How did such a massive collection of stars form quickly and what stopped the star formation at relatively early times?

If these ellipticals did form quickly at high redshift there should be some evidence in high redshift galaxies of this massive star formation activity. A decade ago, the first submillimetre surveys found objects in the early universe that do appear to have very high star formation rates. With such high star formation rates in high

redshift submillimetre galaxies more weight has been added to the suggestion that at least some large galaxies form early in the development of the universe. This has been dubbed anti-hierarchical galaxy formation or cosmic downsizing because in the hierarchical model big galaxies are expected to form after small galaxies.

1.1.1 Submillimetre Galaxies

In the fields of optical and UV astronomy interstellar dust is the ever-present enemy. This is due to the absorption of UV and optical photons by the dust grains, causing extinction and reddening of sources at these wavelengths. With star formation producing large amounts of optical and UV radiation, this extinction introduces uncertainties in studies of the universe using observations in these wavebands, and considerable effort has been spent on understanding and removing this extinction effect. However the energy from those photons that are absorbed by dust has to obey the law of conservation of energy and thus is not lost. The dust grains that absorb these photons are heated and this dust then re-radiates photons but at longer wavelengths.

It was only during the 1980s that technology advanced to a point that allowed astronomers to explore the submillimetre region of the electromagnetic spectrum with early detectors such as UKT14, a single element detector. These advances in technology have also been used to carry out observations at wavelengths greater than 1mm with detectors operating at 1.1 and 1.2mm. A brief description of the type of detectors used can be found in §1.2.1.

The reason that this band has only relatively recently been opened to astronomical observations is due to the serious technical challenges associated with both the

equipment and the observing conditions. These challenges are described below in §1.2. The difficulty in observing at these bands is such that one of the most significant discoveries in this waveband, submillimetre galaxies, were only detected after many hours of observations.

Two of the cameras that have contributed most to observations in this band are the Submillimetre Common User Bolometer Array (SCUBA) (Holland et al., 1999), operating at $450\mu\text{m}$ and $850\mu\text{m}$, and the Max-Planck Millimeter Bolometer (MAMBO) (Kreysa et al., 1998) operating at $1200\mu\text{m}$. These have over the last decade detected significant numbers of luminous submillimetre and millimetre sources in both targeted surveys of sources detected by other instruments and blind surveys of blank fields. Hughes et al. (1998) record some of the earliest detections of high redshift submillimetre sources in the Hubble Deep Field (HDF) with redshift estimates for their sources stretching up to a z of 4. Smail et al. (1997) used clusters as gravitational lenses to perform another early study of bright submillimetre galaxies, finding that they are much more numerous than had been expected. Using both photometric and spectroscopic redshifts, it has been shown the median redshift of submillimetre sources is $z \sim 2$ or possibly slightly higher (Chapman et al., 2003, 2005; Aretxaga et al., 2007).

Submillimetre observations probe the emission from cold dust at high redshifts. It is believed that these dust grains are heated by star formation activity that is heavily obscured in the optical by this dust. X-ray surveys (Waskett et al., 2003; Alexander et al., 2005; Hill & Shanks, 2010) have shown that the submillimetre flux from the majority of these sources is generated by bursts of star formation heating interstellar dust and that it is not primarily due to active galactic nuclei, although a fraction of submillimetre galaxies are thought to house obscured active galactic nuclei (AGN). Studies have shown that submillimetre galaxies commonly have

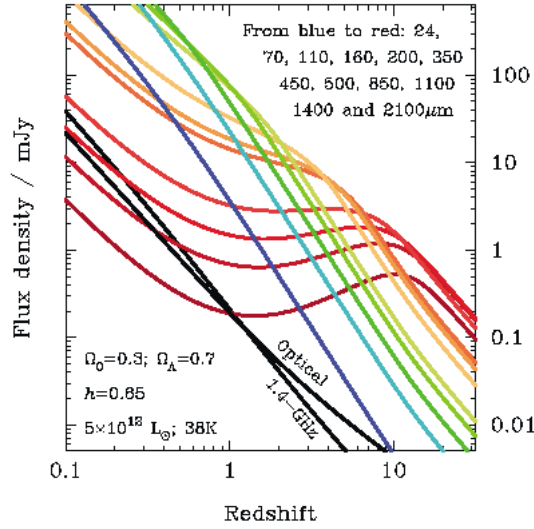


Figure 1.1: Taken from Blain et al. (2002)(their Fig 4). The flux density as a function of redshift for different passbands showing the K correction seen at mm and submm.

disturbed morphologies. This disturbance, could be due to galaxy mergers, which might have triggered the star formation activity. Conselice et al. (2003) found that up to 61% of the submillimetre sources in their sample show some indication of being a merger, albeit with a large error range. Swinbank et al. (2006) deduced from their Hubble Space Telescope (HST) images, along with spectroscopy, that submillimetre galaxies have morphologies that are consistent with mergers. Lilly et al. (1999) also showed that submillimetre galaxies have disturbed morphologies, Swinbank et al. (2006) noted that 5 of 8 of their high-redshift submillimetre objects appeared to be mergers with spectroscopy suggesting two or more subcomponents per submillimetre object. They suggested that this agrees with simulation results indicating merger events. This evidence of merging is possibly the mechanism fuelling one of the more notable features of submillimetre galaxies, massive star formation rates.

Investigations into the star formation rate (SFR) required to produce such submillimetre luminosities have concluded that a SFR of up to $1000 M_\odot$ is needed (Dye

et al., 2008; Alexander et al., 2005). In the local universe a typical SFR for a spiral galaxy is approximately $1M_{\odot}$ a year. The inferred SFRs for these SCUBA discovered galaxies are thus extremely high. This massive amount of star formation would be capable of producing, in a relatively short space of time, the mass of stars seen in massive low redshift ellipticals. This is a conclusion supported by Swinbank et al. (2006) using optical spectroscopy of albeit a small number of spectroscopically identified submillimetre sources. Their analysis of these sources suggests that a dust enshrouded star burst of 300Myr would allow submillimetre galaxies to evolve onto the Faber-Jackson (FJ) relation for local ellipticals. Further evidence for the belief that these high redshift sources may be the ancestors of ellipticals is found in the evolution of the dust-mass function, the space-density of galaxies as a function of dust mass. Dunne et al. (2003) came to the conclusion that local submillimetre sources are not the descendants of these dusty high redshift galaxies and that ellipticals are the more likely candidates.

The importance of submillimetre and millimetre bands for advancing our knowledge of galaxy formation is heightened by the potential for detection of galaxies at very high redshifts. The possibility of discovering high redshift dusty objects is due to favourable K-correction and distance effects (Blain & Longair, 1993; Blain et al., 2002). Normally observing objects with the same intrinsic luminosity at greater redshifts would lead to a reduction in measured flux, that is the further away something is the dimmer it will appear. For a dust-enveloped source at low redshift, however, the peak of its emission is at wavelengths shorter than those observed by SCUBA and other submillimetre detectors. When redshifted, the source will have its peak shifted closer to the observation wavelength. This causes an effective negative K-correction, in which the increase in flux is countered by the increasing distance to the source. The result of this effect can be seen in Figure 1.1. For

optical and radio wavelengths, we see the expected fall off in flux with increasing redshift but the submillimetre and shorter millimetre bands clearly demonstrate a negative K correction, with a suggestion that the flux from a given source might increase at very high redshifts ($z \sim 10$). In chapters 2 and 3 of this thesis I discuss 1.1mm Astronomical Thermal Emission Camera (AzTEC) observations of fields previously observed at submillimetre wavelengths. The strong negative K-correction associated with this wavelength may possibly allow detection of galaxies at higher redshifts than those seen in the submillimetre.

1.1.2 Luminous Infrared Galaxies

There are in the local universe galaxies with an extreme excess of infrared emission when compared to their total luminosity which would appear to be likely candidates for local analogues to high redshift submillimetre galaxies. These galaxies have been dubbed Luminous Infrared Galaxies (LIRGs), Ultra Luminous Infrared Galaxies (ULIRGs) and Hyper Luminous Infrared Galaxies (HLIRGs) according to their infrared output; LIRGs are defined as a source with an infrared luminosity $L_{ir} \gtrsim 10^{11} L_{\odot}$, galaxies with an infrared luminosity $L_{ir} \gtrsim 10^{12} L_{\odot}$ are ULIRGs and HLIRGs are those galaxies with an infrared luminosity $L_{ir} \gtrsim 10^{13} L_{\odot}$. The energy output in the infrared from these sources is greater than the output in all other bands combined.

There are differences between these local infrared bright galaxies and distant submillimetre galaxies. These galaxies appear much more compact than distant submillimetre galaxies. Chapman et al. (2004) find that submillimetre galaxies have diameters of approximately 10kpc (in sensitive radio observations, which they use as a proxy for the far-infrared emission). Swinbank et al. (2006) find, using the

GEMINI Near InfraRed Spectrography (GNIRS) Integral Field Unit (IFU) and the UKIRT Imager-Spectrometer (USIT) IFU along with Advanced Camera for Surveys (ACS) and Near Infrared Camera and Multi-Object Spectrometer (NICMOS) HST imaging, submillimetre galaxies have features at 8-16kpc. In contrast, local infrared galaxies have sizes of the order of 800-900pc (Downes & Solomon, 1998). This suggests that submillimetre galaxies may not be the ancestors of LIRGs seen in the nearby universe. The surface density on the sky of low-redshift ULIRGs is also much lower than that of high redshift submillimetre galaxies. Infrared Astronomical Satellite (IRAS) studies have shown that if the local population of bright infrared galaxies was representative of the high redshift population there would be approximately 0.25 SCUBA sources per square degree when in fact studies show there are greater than 100 submillimetre galaxies per square degree (Blain et al., 2002). These two factors have been taken as evidence that the submillimetre galaxy population has evolved strongly from the high-redshift to the low-redshift universe.

1.2 Submillimetre and Millimetre Sky

Observing faint astronomical objects presents technological challenges at all wavelengths. The difficulties are particularly pronounced however when observing at submillimetre and shorter millimetre wavelengths ($\sim 1\text{mm}$) from the ground. This is partly due to the opacity of the atmosphere at these wavelengths. Figure 1.2 taken from Duncan et al. (1990) shows the percentage atmospheric transmission in the submillimetre to millimetre range for three different amounts of atmospheric water vapour (Naylor et al. (2000) produce similar results using solar observations with a Fourier transform spectrometer at the James Clerk Maxwell Tele-

scope (JCMT)¹). This figure however does show that there are transmission windows over this wavelength range where a greater fraction of the incident radiation reaches the surface ($350\mu\text{m}$ $450\mu\text{m}$ $740\mu\text{m}$ and $850\mu\text{m}$). While optical bands can be affected by the presence of large amounts of precipitable water vapor (PWV) in the atmosphere in the form of clouds, it is clear from Figure 1.2 that the amount of submillimetre/millimetre radiation reaching the surface is greatly reduced when the PWV content is only 0.1mm, even within the transmission windows. The most obvious way to improve this situation is to place submillimetre and millimetre observatories at high altitude to observe above the inversion layer and above some of the PWV in the lower atmosphere. Figure 1.2 was produced using high altitude data from the peak of Mauna Kea, highlighting the fact that even at high altitude the transmission of submillimetre radiation through the atmosphere is adversely affected by atmospheric water vapour.

While positioning the detectors at high altitude significantly improves the atmospheric transmission, a second difficulty arises due to the fact that there is atmospheric emission at these wavelengths which is orders of magnitude greater than the flux from astronomical sources. Duncan et al. (1995) discuss this emission and investigate the different approaches that can be used to minimise it. This emission noise, coupled with the distortions produced by convective cells in the upper atmosphere, leads to large scale correlated noise. This sky noise easily swamps the faint astronomical signal. When observing point sources in blank fields this correlated noise can be removed with careful analysis (as described in §2.2.3), because the highly correlated components are the large scale sky variations (with possibly some extended astronomical signals) while the point sources are largely (assuming that

¹The James Clerk Maxwell Telescope is operated by The Joint Astronomy Centre on behalf of the Science and Technology Facilities Council of the United Kingdom, the Netherlands Organisation for Scientific Research, and the National Research Council of Canada

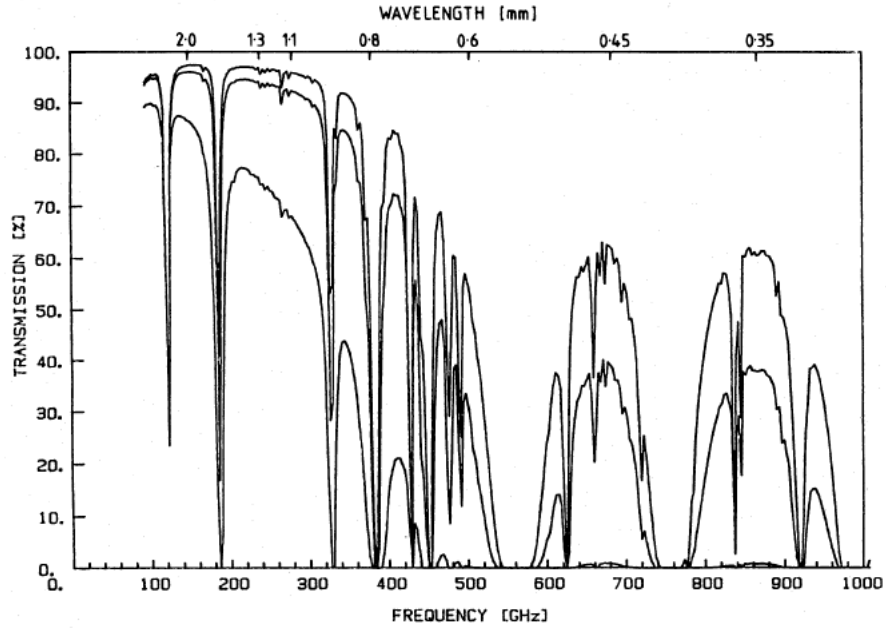


Figure 1.2: Taken from Duncan et al. (1990) (their Fig 1). Atmospheric transmission measured from Mauna Kea for PWV values of 0.1mm 0.5mm and 1mm.

there is no significant clustering) randomly distributed and so exhibit considerably less correlation than the sky signal. Mapping extended submillimetre sources requires a different approach as the principle component analysis (PCA) described in §2.2.3 would severely attenuate the correlated flux from the object of interest. The primary aim of this study is detection of high redshift galaxies and so removing the flux from extended objects, while leaving the point sources largely unchanged, is an advantage rather than a drawback as high redshift submillimetre galaxies are essentially point sources.

More recently with the advent of the Herschel space telescope (Pilbratt et al., 2010) the problem of atmospheric noise has been removed completely and the first results from this new observatory dramatically display the advantage that is gained from taking the atmosphere out of the equation.

1.2.1 Bolometers

The 1.1mm observations described in chapter 2 were taken using the AzTEC camera fitted to the JCMT. This camera is composed of 144 detectors called Bolometers. Bolometers were invented in 1880 by Samuel P. Langley. They are wide band detectors that rely on the temperature change created by the absorption of a photon to register a detection of that photon. A thermometer (thermistor) connected to the bolometer registers this change and the incident radiation is detected. The material the thermometer is constructed from is chosen so that the small temperature changes induced by the incident radiation will cause a relatively large change in the resistivity of the thermometer. In the infrared, submillimetre and millimetre bands neutron transmutation doped germanium thermistors are used as the thermistor and more complex micro-mesh structures are used as absorbers (Mauskopf et al., 1997).

While bolometers are suitable for observations over a wide range of wavelengths, the submillimetre and short wavelength millimetre bands are distinct from both optical and radio bands in terms of the technology required to observe objects at those wavelengths effectively. This led to the development of so called quasi-optical systems. This approach uses mirrors and in some cases lenses to guide the radiation from the secondary mirror to a feed horn. This feed horn then channels the radiation down a wave-guide to the bolometer.

1.3 Submillimetre/Millimetre Resolution

Another distinct problem associated with observations at submillimetre and millimetre wavelengths is the large beam associated with these instruments. AzTEC, for instance, has a beam of 18 arcseconds and SCUBA had a beam full width half maximum (FWHM) at $850\mu\text{m}$ of 15 arcseconds. This poses problems for identifying the positions of objects in images at these wavelengths. It has been shown that there can be errors of several arcseconds in positions of objects as measured from AzTEC or SCUBA positions (Scott et al., 2002). This makes follow up observations at optical, radio and other wavelengths more difficult as a given submillimetre galaxy could have several possible counterparts in an optical or radio image. There are statistical methods that can be used to identify submillimetre galaxies in other wavebands (I describe the application of one of these techniques in chapter 5). These techniques are particularly useful for identifying radio sources with submillimetre/millimetre sources because the surface density of submillimetre/millimetre sources is much lower than that of optical galaxies. The accurate radio position can then be used to identify the optical galaxy responsible for the submillimetre emission. This does, however, introduce a selection bias as studies have shown not all submillimetre galaxies are visible at radio wavelengths (Ivison et al., 2002) and submillimetre objects with detectable radio emission are likely to be at redshifts less than three due to the lack of a negative K-correction in the radio portion of the spectrum. Mid-infrared observations can also be used to get accurate position submillimetre galaxies but these studies might also introduce a bias as not all submillimetre objects are detected in the mid-infrared (Pope et al., 2006).

1.4 The Cosmic Infrared Background

A glance at the night sky or the results from the many optical surveys will show that there is a significant amount of astronomical radiation in the visible portion of the electromagnetic spectrum. This produces a peak in the Extragalactic Background (EGB) which is called the Cosmic Optical Background (COB). The light producing this peak is mainly unobstructed star light. However, as mentioned above, there are galaxies where this optical radiation is absorbed by dust and re-radiated at longer wavelengths. Some of this radiation has been detected as discrete sources in the submillimetre bands. These sources also produce a significant peak in the extragalactic background. This second peak, dubbed the Cosmic Infrared Background (CIB) or the Far Infrared Background (FIRB), was first detected by Puget et al. (1996) using data from the Far Infrared Absolute Spectrophotometer (FIRAS) (Mather et al., 1993) instrument on the Cosmic Background Explorer (COBE) (Boggess et al., 1992). Hauser et al. (1998) subsequently presented results from the Diffuse Infrared Background Experiment (DIRBE) (Silverberg et al., 1993) instrument, also on COBE that show the detection of the CIB at $140\mu\text{m}$ and $240\mu\text{m}$ and place upper limits on the infrared background in the $1.2\mu\text{m}$ to $100\mu\text{m}$ bands. Fixsen et al. (1998) used the FIRAS instrument on COBE to investigate the spectrum of the CIB. They discovered that it peaks in the far infrared at a wavelength of approximately $200\mu\text{m}$. These peaks can be seen in Figure 1.3

The significance of these far-infrared and submillimetre bands, stretching from $\sim 30\mu\text{m}$ to 1mm , is shown by the fact that the amount of electromagnetic radiation in the CIB is comparable to that seen within the visible spectrum. This implies that a very significant proportion of the star formation history of the universe is

hidden from optical and UV observations, either completely, or partially behind obscuring dust. Figure 1.3, taken from Dole et al. (2006), plots the extra galactic background radiation from $0.1\mu\text{m}$ to $1000.0\mu\text{m}$ using measurements from multiple different instruments to show the two peaks, with the COB in blue and the CIB in red. The grey shaded region is an upper limit on the extragalactic background light obtained by using the interaction between very high energy gamma-ray photons from blazars and the infrared photons of the CIB. This plot clearly illustrates how significant the amount of radiation making up the CIB is in comparison to the COB.

While the detection of the CIB and the determination of its spectral energy distribution (SED) are useful scientifically, the background as its name suggests is an unresolved source of radiation that is largely uniform across the sky and this contains hidden information. One way to get more information is to resolve the background into individual sources and determine the types of objects that are producing this huge repository of energy. This is one of the projects I will undertake in this thesis, although it is important to note that at 1.1mm , the operating wavelength of AzTEC (chapter 2), the level of the CIB is much less than at its peak.

It is worth noting that the CIB and COB are not the only peaks seen in the Extragalactic Background (EGB). The CMB is probably the best known of the features in the extragalactic background. It is believed to be a relic of the Big Bang having formed during the period known as recombination when the early universe had cooled enough to allow neutral atoms to form, reducing the population of free electrons and drastically increasing the mean free path for photons. Thus the CMB is a feature in the EGB that is not directly related to the galaxies that are studied in this thesis.

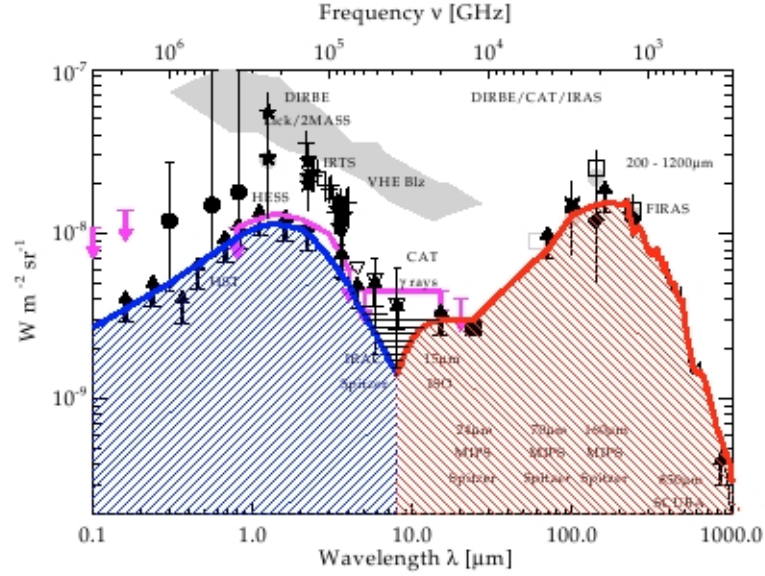


Figure 1.3: Taken from Dole et al. (2006)(their Fig 13). The Cosmic Optical Background in blue and the Cosmic Infrared Background in Red with data points from different instruments labelled. The grey areas is an upper limit taken from the gamma-ray spectrum of blazars.

1.5 Thesis Structure

This thesis is divided into six chapters. In chapter 2 I discuss the AzTEC observations of the Lockman Hole (LH) field and the Subaru XMM-Newton Deep Field (SXDF) and subsequent reduction of this data-set. In chapter 3 I discuss the use of a stacking technique to detect emission from Spitzer² sources in the 1.1mm AzTEC LH image and to determine the contribution Spitzer galaxies make to the CIB in the 1.1mm band. I also describe an estimate of the mass of dust associated with the Spitzer galaxies. In chapter 4 I describe my attempt to determine the effectiveness of using the ratio of 850μm SCUBA flux to 1.1mm AzTEC and 1.2mm MAMBO flux as a redshift indicator. In chapter 5 I describe an attempt to identify Spitzer InfraRed Array Camera (IRAC) sources in the Canada UK Deep Submillimetre Survey (CUDSS) 3hr field. The conclusions of these different inves-

²The Spitzer Space Telescope, which is operated by the Jet Propulsion Laboratory, California Institute of Technology under a contract with NASA.

tigations and some suggestions of possible future work are summarised in chapter 6.

Chapter 2

Aztec Observations

2.1 Introduction

In this chapter I will be discussing the use of the AzTEC camera (Wilson et al., 2008), a 1.1 millimetre instrument on the JCMT, to image two fields, the Lockman Hole (LH) field and the Subaru XMM-Newton Deep Field (SXDF) as part of a study into the properties of the high redshift submillimetre universe. I will also describe the data reduction process used to produce maps from these observations. The data reduction was carried out using an IDL¹ pipeline developed by the team that built the detector at the University of Massachusetts (Amherst).

¹<http://www.itvis.com/ProductServices/IDL.aspx>

2.1.1 SHADES

The observations described in this chapter were undertaken to conclude a previous study that had been interrupted by the decommissioning, in July of 2005, of the SCUBA detector that had been installed on the JCMT. This study, the SCUBA Half Degree Extragalactic Survey (SHADES), was undertaken to image a half square degree of sky using the SCUBA camera on the JCMT using both of SCUBA's primary bands, $450\mu\text{m}$ and $850\mu\text{m}$. The results of this project can be found in a series of papers written by the SHADES consortium (Mortier et al., 2005; Coppin et al., 2006; Ivison et al., 2007; Aretxaga et al., 2007; Takagi et al., 2007; Coppin et al., 2008; Dye et al., 2008; Serjeant et al., 2008; Clements et al., 2008). The survey was planned to observe, as the name suggests, a half square degree of sky over two fields, the LH field and the SXDF area.

These two fields are highly studied regions of sky with a significant amount of multi-wavelength coverage available in radio, optical, submillimetre and infrared bands. Both have little galactic cirrus contamination allowing for deep observations in which faint sources are not obscured by gas and dust located within the vicinity of the Milky Way. They are also largely devoid of bright nearby galaxies and clusters, which would create difficulties for observations of distant sources. This, coupled with the fact the observations do not target specific objects, is why the observations of these regions and others like them are called blank field studies.

Due to technical problems with SCUBA the survey was not completed as originally planned. With this curtailment of the survey in mind, follow up observations were taken using AzTEC, which was installed on the JCMT as a visiting instrument in place of SCUBA while SCUBA's successor (aptly named SCUBA 2) was under development. In effect the camera was then used to complete the survey at 1.1mm

instead of the $850\mu\text{m}$ and $450\mu\text{m}$ SCUBA bands previously used. AzTEC also observed the areas previously surveyed by SCUBA, so it actually covered a larger area of sky to a similar depth, approximately 0.6 square degrees compared to 0.2 square degrees for the SCUBA observations. This forced change of observing band is fortuitous in another way, as in Chapter 4 it is exploited to investigate the use of submillimetre to millimetre fluxes as a redshift estimator.

Austermann et al. (2010) (hereafter AU10) also reduced the data and produced a set of maps which will be compared below with those produced for this chapter. The purpose of the dual reduction was to check that the source catalogues and maps did not depend on the subjective decisions made during the data reduction process. The SCUBA $850\mu\text{m}$ maps were similarly reduced independently by several groups (Coppin et al., 2006).

2.2 Observations

2.2.1 Fields

As mentioned above, the regions observed with the AzTEC instrument while it was installed on the JCMT for the SHADES project were the Lockman Hole field and the Subaru XMM-Newton Deep Field. These are centred on $10^h 52^m, +57^\circ 00'$ and $02^h 18^m, -05^\circ 00'$ respectively.

2.2.2 AzTEC and the JCMT

The JCMT is a submillimetre telescope with a 15 metre diameter primary mirror situated at an altitude of approximately 4 kilometres on the dormant Mauna Kea volcano on Hawaii's Big Island.

AzTEC is a 144 bolometer detector operating in the millimetre wavelength range which was built for operation on the Large Millimeter Telescope (LMT) (Kaercher & Baars, 2000). Its initial observing runs were however undertaken on the JCMT on Mauna Kea as construction of the LMT was ongoing. The detector consists of 144 silicon-nitride micro-mesh bolometers, that are arranged in a close packed hexagonal formation. The detectors are kept at an operating temperature of 250mK with a 3 stage closed cycle Helium refrigerator.

It was designed to observe at 1.1mm, 1.4mm and 2.1mm wavelengths. However the filters are not interchangeable during an observing run with the detector installed on a telescope. During the JCMT observations the detector had its shortest wavelength filter fitted (1.1mm). This filter was chosen to enable observations of submillimetre galaxies through re-radiated emission from dust grains (the 1.4mm and 2.1mm pass bands are better suited to studies of the Sunyaev-Zel'dovich effect (Sunyaev & Zeldovich, 1980)).

During commissioning of AzTEC on the JCMT it was noticed that the detector had 37 non-responsive bolometers which were largely clustered together. This can be seen in Figure 2.1 which shows the position on the sky of each operational bolometer (this was constructed using beam map observations). The most significant effect of this was on the jiggle mapping of the pointing, calibration and focus sources where the object being imaged could be lost in the low coverage portion of the jiggle map

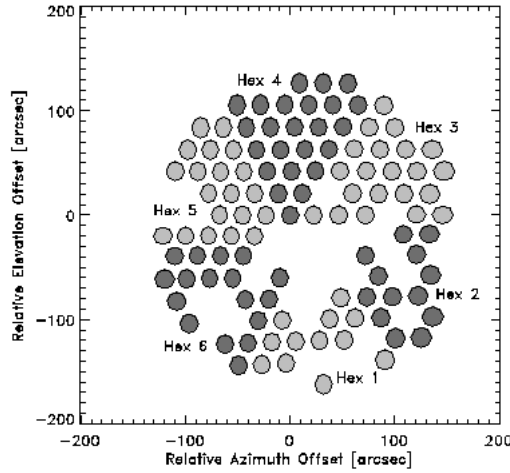


Figure 2.1: Taken from Wilson et al. (2008) (their Fig 11). The positions of the working AzTEC bolometers are represented by ellipses while the size of each ellipse represents the beam full-width half-maximum. (The shading indicates the manner in which the bolometers in the different segments are connected to the instrument’s electronics in 6 different *hexants*)

as the jiggle procedure was not changed to account for the missing bolometers. This was easily remedied by slightly shifting the centre position of the pointing observation and repeating it to ensure that the source remained outside the low coverage section. This clearly increased the overheads of each science observation. The main mapping effort used a raster scanning technique and was much less affected by this issue. These two types of mapping are discussed below.

2.2.3 Mapping Strategies

Mapping strategies for observations at submillimetre and shorter millimetre wavelengths are designed to mitigate two of the most significant problems associated with the detectors and the sky. The first problem is clearly visible in Figure 2.1. This image shows the actual bolometer pattern on the sky for AzTEC. The individual beams of the bolometers do not fully sample the sky. A telescope with a bolometer array can not be operated in the same fashion as a telescope equipped

with a Charge Coupled Device (CCD), for example, as the images produced in a single pointing would be under sampled. The second issue is the correlated sky noise described in §1.2.

Jiggle Mapping

One of the observation strategies traditionally used at submillimetre wavelengths is an approach called *jiggle mapping*. This method produces a fully sampled map by moving the secondary mirror of the telescope to different positions ensuring that the gaps in the image due to the bolometer spacing are fully filled in at the end of this jiggle sequence.

During the jiggle process the secondary mirror is also used to move the beam off source so that the bolometers are only observing the background and what ever instrumental effects are present. Subtracting this off-source data from the on-source data helps remove the sky and instrument related signals. This process is called chopping. When a full jiggle sequence is completed the telescope is *nodded*. The telescope primary mirror is moved such that the initial on-source beam is moved off-source and the initial off-source chop beam becomes the on-source beam and the jiggle mapping sequence is repeated. This can be seen on the left hand side of Figure 2.2 where circle (A) represents the initial off-target pointing and (B) the second off-target pointing after the telescope is noddied, with the centre circle representing the telescope beam on target.

The primary reason for nodding is to deal with any gradients across the area being imaged which would create a spurious signal if the secondary mirror was just chopped in one direction on the sky. Wilson et al. (2008) suggest that nodding also deals with scattering from the JCMT's secondary mirror support structure.

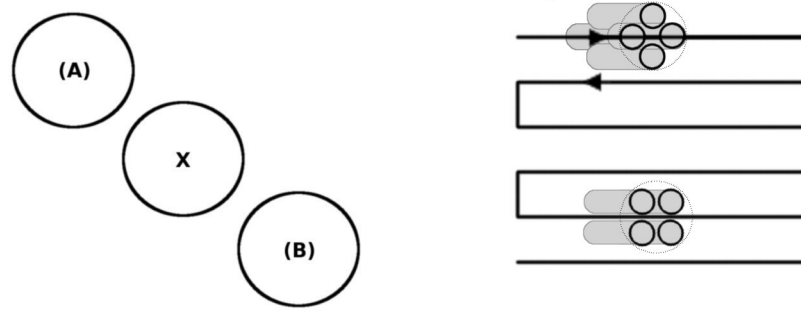


Figure 2.2: AzTEC scanning strategies. (A) and (B) represent off-source positions for the jiggle mapping approach with the centre circle representing the on-source beam. The ‘ladder’ on the right hand side demonstrates the raster scanning strategy.

The only observations in the AzTEC/SHADES observing run that made use of jiggle mapping were the focus, pointing and secondary calibration observations as they were of point sources smaller than the beam size. These observations were carried out with a jiggle map frequency of one hertz and a chopping frequency of between two and four hertz. Primary calibration observations were taken at the start of each night’s observing while the secondary observations were taken roughly halfway through the night.

This approach is obviously most suited to small fields due to the overheads associated with carrying out a full jiggle sequence and then repeating it for the second nod position. The overall coverage (the integration time per pixel) produced by this method is also not very even when compared with other observing techniques such as raster scanning. Another complication in the case of AzTEC is that the coverage in jiggle map mode is much more affected by the unresponsive bolometers than the raster scan approach.

Raster Scanning

The scientific, beam map and primary calibration observations undertaken during the AzTEC JCMT observation run used a mapping technique referred to as raster scanning. This type of observation involves simply scanning the detector across the target line by line. The telescope then steps up or down perpendicular to the scan direction and then reverses direction to scan back across the field. This is repeated producing a map that is scanned line by line. This approach has much lower overheads than the jiggle mapping technique, particularly with AzTEC as the detectors are stable enough to avoid the need to chop the secondary mirror as would have been done with SCUBA. Another advantage of this approach for the observing run at the JCMT is that the inoperative bolometers do not introduce uneven coverage; they just slightly reduce the sensitivity of the final map. Raster scanning is not immune to the under-sampling problem associated with the bolometer beam pattern if the detector is scanned across the sky such that the gaps in the beam pattern are not taken into account. The right hand side of Figure 2.2 shows the raster scan ‘ladder’ along with a beam pattern of a fictional four element bolometer detector. The detector is shown at two angles. The top detector is angled in such a way that the four bolometers produce a fully sampled map. The grey area shows the area covered as the detector scans across. The angles that allow for a fully sampled scan map are normally called *magic angles*. A second portion of a scan is shown towards the end of the ‘ladder’. Here the detector is rotated through 45 degrees compared to the earlier position. In this position the top two and bottom two detectors are aligned leaving a gap between them. This detector angle would produce a stripy or under-sampled raster scanned image.

This technique unlike jiggle mapping does not remove any sky contamination from

the beam and so removing this noise has to be done after the observation. The AzTEC pipeline does this using a mathematical technique called PCA which I describe below.

2.2.4 Observation Details

The actual observations were taken over a period of approximately three months, from November 2005 to January 2006. The two fields were initially observed using ~ 20 minute exposures, covering a $15' \times 15'$ region, but midway through the observing run the decision was made to extend the individual exposures to ~ 55 minutes, covering a $35' \times 35'$ region, to improve mapping efficiency by reducing overheads. Analysis of the early part of the observing run showed that the larger maps could be imaged using a faster scan speed which helped reduce the level of atmospheric contamination (Wilson et al., 2008). The area observed in the LH field is ~ 0.30 square degrees and ~ 0.36 square degrees in the SXDF field. The reason for the larger area covered by the SXDF observations was an error during the observation run that shifted the centre position of the observations in declination. As is noted below, and can be seen in Figure 2.6, this error creates less even coverage across the SXDF map than the LH map, and the final image is not as deep as the LH map which has, as intended, largely even coverage.

Focus observations were carried out at the start of a night's observing and half way through the night. The purpose of these focusing observations was to account for changes in the geometry of the primary and secondary mirrors during the observing run due to temperature and telescope orientation changes. Pointing observations were taken approximately every hour, although when the smaller areas were being observed pointings were sometimes taken more frequently. These observations were

used to determine the drift in the telescope's tracking. These were carried out using jiggle-map observations and a two-dimensional Gaussian was then fitted to the source in the map to determine the pointing offset. These individual pointing offsets were interpolated to determine how the pointing changed during the night's observing run. The observations and process used to calibrate the bolometer time-streams are described below in §2.3.1.

2.3 Map Making

This section will describe the process I used to produce the 1.1mm maps which are shown at the end of this chapter. The software and method used in this reduction were developed by the AzTEC instrument team and more details can be found in Wilson et al. (2008); Scott et al. (2008); Austermann et al. (2010); Perera et al. (2008).

The individual steps in the pipeline are as follows:

1. Cleaning and Calibration of raw time streams and converting them to maps.
2. Co-adding the cleaned individual maps into a large unfiltered single image.
3. Producing Jackknife realisations of the cleaned time streams.
4. Produce an average power spectral density (PSD) from the noise realisations.
5. Co-addition of individual noise realisations into a single large Weiner filtered noise map.
6. Determination of the average noise level in the co-added noise realisations.

7. Wiener filtering of the unfiltered single image from item 2.

2.3.1 Cleaning and Calibration

The first processes in the pipeline involves de-spiking the data, cleaning the time streams and calibrating them.

Despiking

The initial step in the map-making process was to remove any obvious spikes in the data. These are generated by cosmic rays interacting with the detector or its electronics. They can also be generated by random fluctuations in the instrument itself. These generally manifest themselves as a large short-duration jump in flux seen in a single detector's time-stream. Those that are above the detection threshold (in the AzTEC pipeline those greater than $+7\sigma$ or less than -7σ of their neighbouring samples) are removed from the time-stream with their magnitude used to estimate how large a section of the time-stream to remove. The section of the time-stream that has been deleted is replaced with Gaussian noise so as not to adversely effect the atmospheric noise removal carried out later in the pipeline.

Sky Subtraction

With these spikes dealt with, the next step in the pipeline is the removal of the noise contribution due to the atmosphere. The primary method in the AzTEC pipeline for blank-field surveys where large scale structure is of no interest is to use principle component analysis (PCA). This technique was used successfully with the 1.1mm

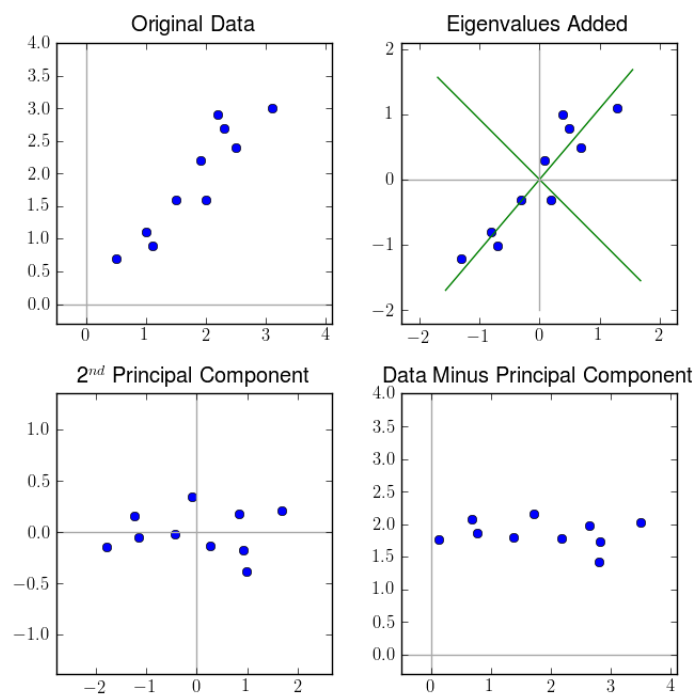


Figure 2.3: This is a simple 2 dimensional example of Principal Component Analysis. The units are arbitrary. In the top two figures and the last image the axis represent the independent (x) and dependent (y) variables. In the bottom left figure the data is transformed so that one of the first eigenvector is on the x-axis and the second on the y-axis.

Bolocam detector on the Caltech Submillimeter Observatory (CSO) (Laurent et al., 2005) and the mathematics behind PCA is described in detail in F. Murtagh & A. Heck (1987).

The PCA technique exploits the fact that the atmospheric noise in this portion of the spectrum is highly correlated while the astronomical signals under study are not very tightly correlated within the telescope beam. PCA transforms the data such that the correlations within the data can be studied.

In the case of the AzTEC pipeline, the data from a single scan is placed in a matrix in which one axis of the matrix represents the bolometers and the other the measurements in each time sample. A scan is a single line of the ‘ladder’ shown in Figure 2.2. From this matrix the eigenvectors and eigenvalues are found. The analysis then determines which eigenvectors have large eigenvalues. These are the most correlated portions of the data. The eigenvector with the largest eigenvalue is referred to as the principal component. The principal component is removed and the data is transformed back into time streams.

A basic two dimensional example² of this process can be seen in Figure 2.3. The first figure shows the raw data with a very clear correlation in it. The second plot on the top row shows the data with its x and y means subtracted (PCA requires data with a zero mean) and the two eigenvectors plotted. The lower left figure is a plot of the second principal component. This is effectively the data minus the most correlated component, which is analogous to removing the most correlated sky contamination. And finally the last figure is the data minus the most significant correlations transformed back into its original form.

²This example was adapted from the example found at: http://www.dfanning.com/code_tips/pca.html.

In the AzTEC pipeline a form of adaptive PCA analysis is implemented. That is, the process is repeated until a desired amount of correlation is removed from the bolometer time-streams. This is done by finding the mean and standard deviation of the eigenvalues in log form. Those eigenvalues that are outside 2.5σ of the mean are removed and the PCA is repeated until there are no significant eigenvalue outliers ($> 2.5\sigma$).

Laurent et al. (2005) and Scott et al. (2008) both note that a side effect of PCA cleaning is the attenuation of the the signal from point sources. This is due to the fact that some of the power from point sources in the time-stream is seen at the same scale as correlated atmospheric noise and so gets removed when those principal components are extracted.

The AzTEC pipeline deals with this problem by creating an empty noiseless set of time-streams and inserting a 1Jy Gaussian point source into them. The principal components that are identified and removed from the real time-streams are also removed from the simulated data. This data is then converted from the time domain into a map in the same way as described below for the real time streams. As the correlated data from the real sky removal has been removed from this image, the artificial point source is attenuated in the same fashion as a real point source. The size of the reduction in flux can then be determined and applied to the real data. This so called *point source kernel* is used later in the pipeline as part of the filtering process.

Calibration

The calibration of the instrument is described in detail in Wilson et al. (2008). The main calibration source used during the observing run was Uranus. The calibration

process results in an error on the calibrated flux of between 6 and 13%.

2.3.2 Co-adding

With the sky contribution removed from the time-streams, the data for each of the individual observations is then mapped onto a grid that is a tangent to the celestial sphere to produce a set of cleaned maps. The point where this grid is a tangent to the celestial sphere was chosen to be $10^h51^m59^s$, $+57^\circ21'43''$ in the LH field and $02^h18^m01^s$, $-04^\circ59'54''$ in the SXDF. These positions were chosen as they coincided with those used in the SHADES $850\mu\text{m}$ maps of both regions, making future comparisons between the earlier SCUBA maps and these AzTEC maps easier. The pixel size of the grid was chosen to be $3''$ by $3''$ for the same reason.

Each detector's contribution to each pixel has to be estimated to allow for each detector's different sensitivities and noise levels. For AzTEC the value for a given pixel is given by the weighted average of all the samples from all the bolometers that contribute to that pixel. Each sample from a given bolometer is weighted using the inverse variance of all the samples from the scan the sample resides in (a scan is a single line of the 'ladder' shown in Figure 2.2). The portions of each scan where the telescope starts decelerating to turn around and commence a return scan are ignored as the rapid acceleration would reduce the accuracy of the pointing estimate and it is possible that the detector noise would increase due to increased telescope vibrations etc.

With the individual observations converted from temporal to spatial co-ordinates, they are then co-added into a single large map using the following relation (found

in Scott et al. (2008)):

$$S = \frac{\sum_{i=0}^n W_i S_i}{\sum_{i=0} W_i} \quad (2.1)$$

Where S is the weighted average flux value for each pixel in the co-added map, W_i is the weight value for that pixel in the individual map i , S_i is the flux value for the pixel in the individual map and n is the total number of individual observations to be co-added.

2.3.3 Noise Estimation

The AzTEC pipeline uses a *jack-knife* approach to creating noise maps. This exploits the fact that real objects and features should be consistently present in the individual observations and across the different bolometers. The signals from each individual bolometer in each scan were randomly multiplied by ± 1 . The real objects (including the contribution from unresolved sources as these should appear in more than one time stream from one bolometer) are effectively removed from the data leaving the noise properties essentially unchanged. This is true because the noise (sky contamination remaining after the PCA cleaning and the remaining instrument fluctuations) should be uncorrelated between the individual observations which were taken at different times over different nights in the observing run.

Scott et al. (2008) determined that for their data set of AzTEC observations in the Cosmic Evolution Survey (COSMOS) (Scoville et al., 2007) field the standard deviation of the individual jack-knifed observations differed from that of the actual

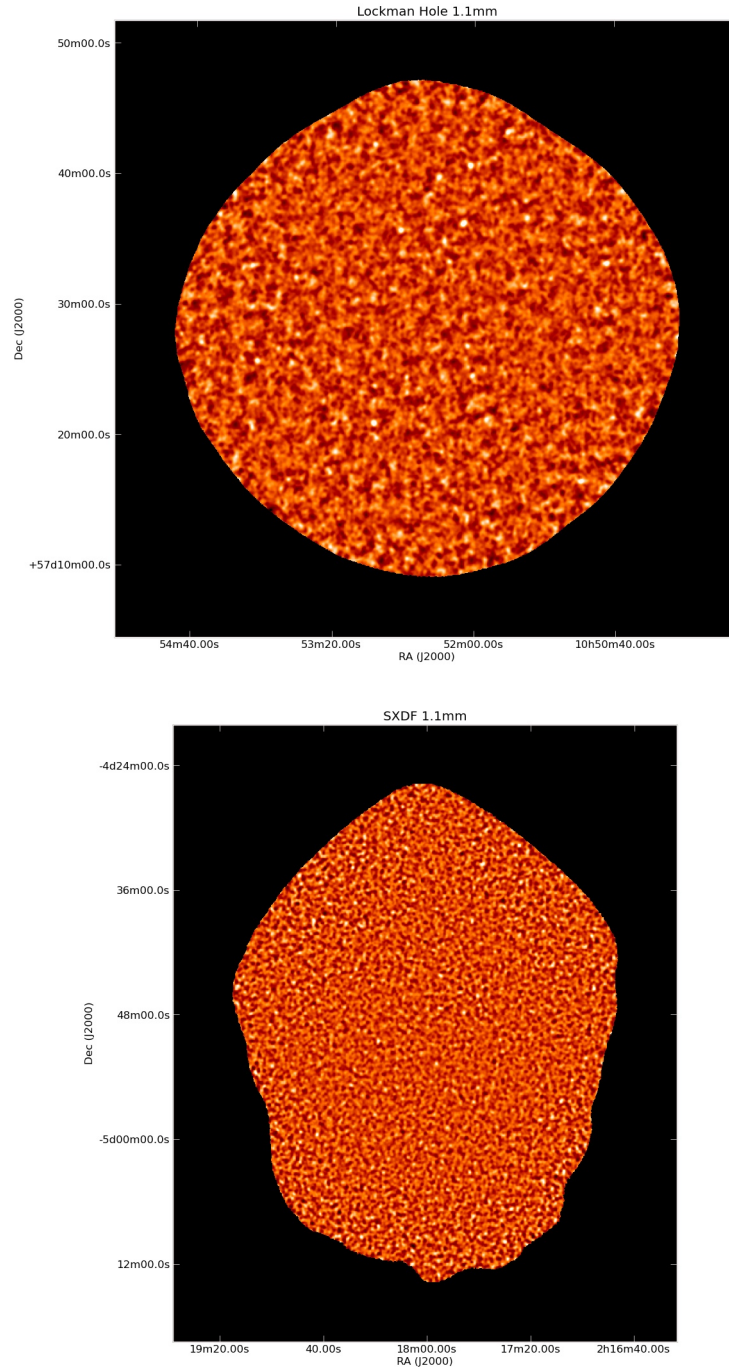


Figure 2.4: AzTEC 1.1mm Lockman Hole (top) and SXDF (bottom) signal maps. The brighter the colour the greater the flux ($(Jy/Beam)$).

individual observations by less than 0.6% implying that the noise properties in the noise maps have not been changed by the jack-knife process. The COSMOS observations are similar to the SHADES observations in that they target blank fields and so it is reasonable to assume that the properties of the noise maps in this reduction would not be significantly altered either.

In the reduction, five jack-knife realisations are produced for each individual observation and then one of these five jack-knife realisations is chosen at random for each individual observation and co-added together to produce a large co-added noise map. This coaddition is repeated 100 times and then a 1-dimensional power spectral density (PSD) for each of the 100 co-added noise realisations is found. The average of these 100 PSD is determined and used below as a whitening filter.

2.3.4 Filtering

After the noise estimation step the map is then filtered using an optimal filter that is described in Scott et al. (2008). This filter makes use of the *point source kernel* described above. The purpose of this filter is to remove pixel to pixel variations in flux that can not be related to the incident flux due to the fact that the size of the pixels (3 arcsec by 3 arcsec) is much smaller than the beam size (which is approximately 18 arcsecs). This maximises the signal-to-noise from point sources. Both the signal map and the point source kernel are high-pass filtered using a filter with a response that is the inverse square root of the average PSD which was generated earlier from the noise maps. The purpose of this step is to remove the extra noise that is seen at low spatial frequencies in the Fourier transforms of noise maps. The filtered map is then convolved with the filtered point source kernel and then scaled to account for the attenuation in the point source kernel due to the

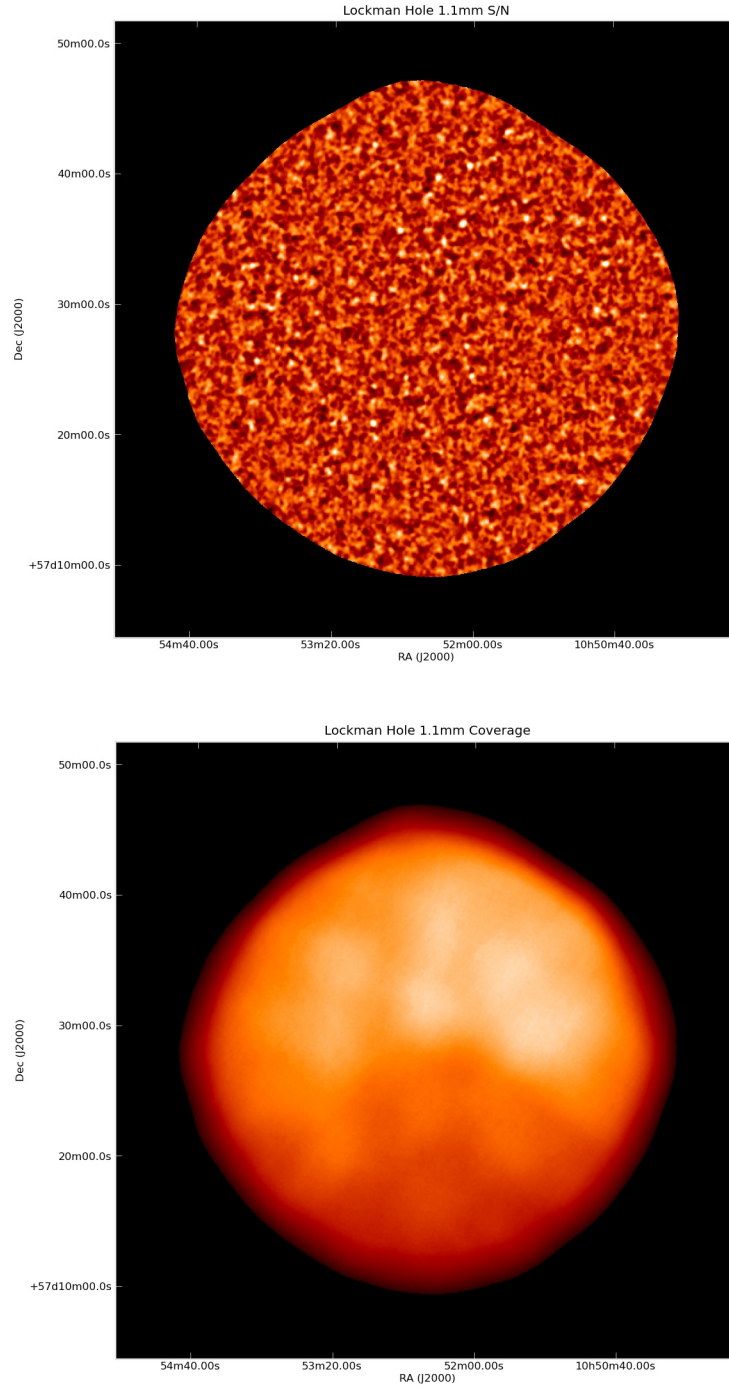


Figure 2.5: AzTEC 1.1mm Lockman Hole S/N (top) and Weight (bottom) maps. The brighter the colour in the S/N map the greater the S/N and in the weight map the lower the noise $((\frac{J_y}{Beam})^{-1})$. The weight map is proportional to $\frac{1}{\sigma^2}$.

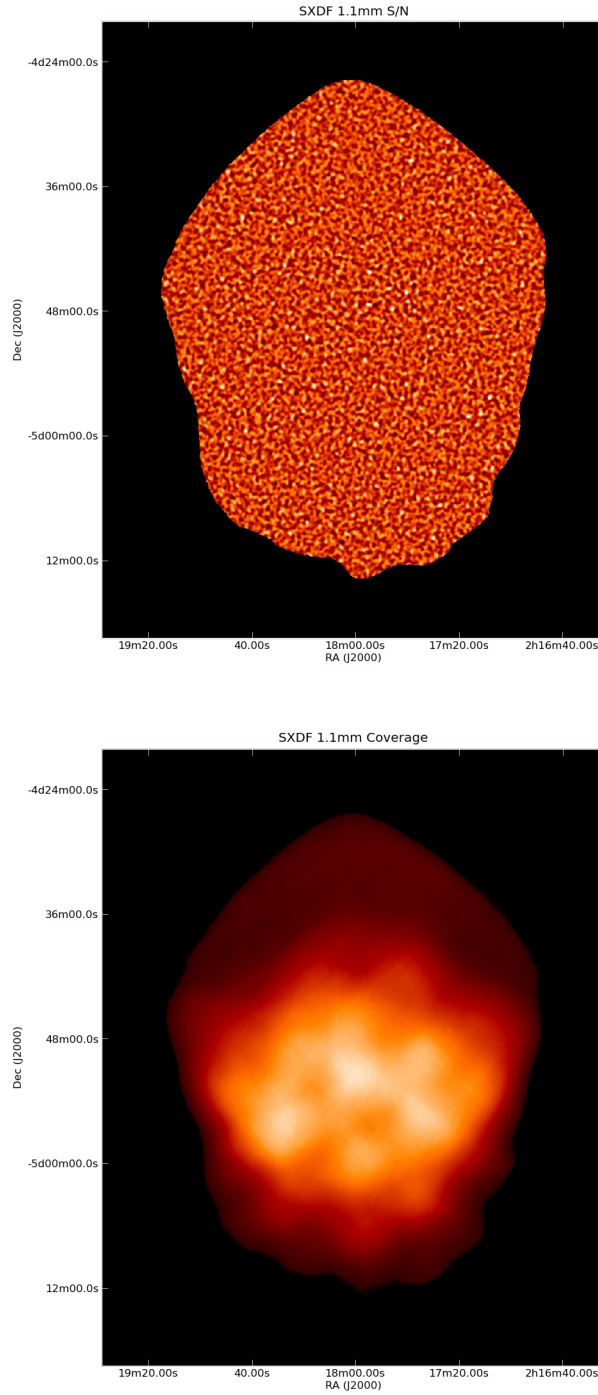


Figure 2.6: AzTEC 1.1mm SXDF S/N (top) and Weight (bottom) maps. The brighter the colour in the S/N map the greater the S/N and in the weight map the lower the noise ($(\frac{J_y}{Beam})^{-1}$). The weight map is proportional to $\frac{1}{\sigma^2}$.

PCA cleaning.

2.4 Final Maps and Sources

The final co-added signal maps can be seen in Figure 2.4. These images have had a cut applied to them so that only those areas of the map are shown which have a noise level within $\sqrt{2}$ of the noise level of the central low noise region, thereby removing the noisy low-coverage outer regions. Figures 2.5 and 2.6 show the corresponding signal-to-noise maps and the weight maps for each field. Immediately apparent from these images is the greater non-uniformity in the SXDF map. This is due to an error in the observing scripts that occurred approximately half way through the observing run. This shifted the centre of the observations and had the overall effect of reducing the depth of the SXDF image in comparison to the LH image. When the error was discovered, the observations plan was altered to try and create as large an area of uniform coverage within the SXDF field as possible.

The AU10 reduction differs from my reduction in that the list of individual observations was compiled independently. While the set of observations is largely the same there are some differences due to corrupted observations and different decisions on whether or not to include marginal maps. This slightly different set of observations has led to maps of slightly different depths. The AU10 maps have a noise level of between 0.9mJy and 1.3mJy for the Lockman Hole field and 1.0mJy to 1.7mJy for the Subaru XMM-Newton Deep Field field, while my maps have a noise level of between 0.8mJy and 1.2mJy for the LH field and 1.0mJy and 1.6mJy for the SXDF region. While the noise range from the deepest regions to the shallower edges of the maps is not identical, it is however largely similar.

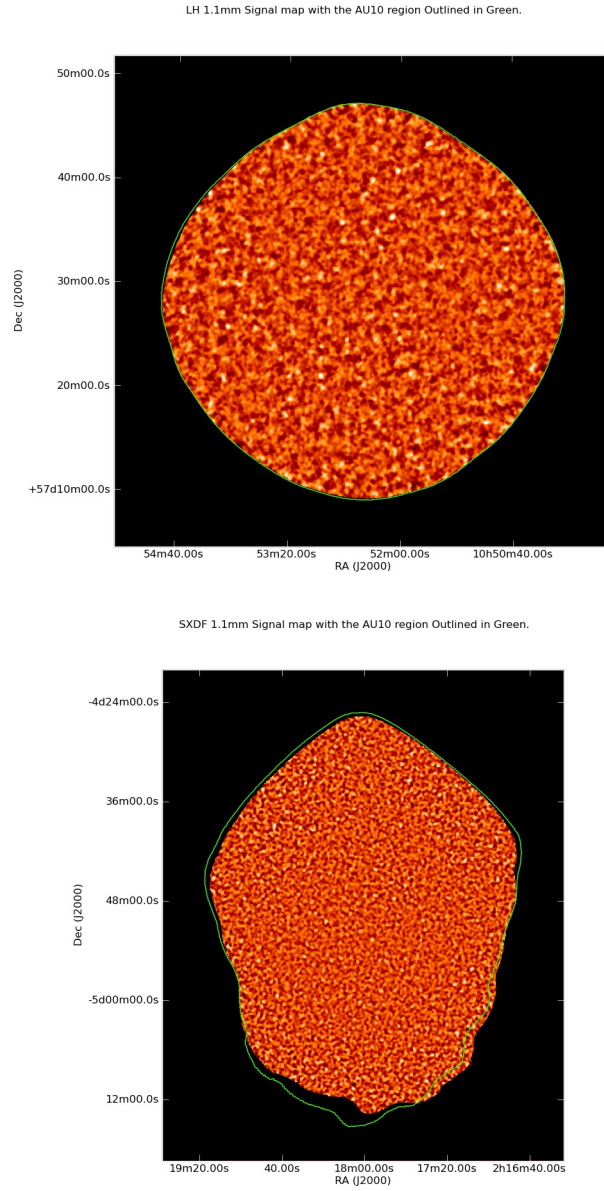


Figure 2.7: The Aztec Lockman Hole (top) and SXDF (bottom) signal maps from the reduction discussed here with the areas mapped by AU10 outlined in green.

Both reductions produce maps of similar size with those I produced covering 0.303 square degrees and 0.360 square degrees in the LH and SXDF regions respectively while AU10 published maps with areas of 0.304 square degrees and 0.367 square degrees for their LH and SXDF images using the same noise cut as was used on the maps in Figure 2.4. The two images in Figure 2.7 show my signal maps for both fields with the area mapped by AU10 outlined in green. The LH maps agree much more closely than the SXDF maps. This is to be expected as the SXDF observations consisted of more short exposures spread over a larger area so any difference in the input observations would be more obvious.

AU10 carry out a source extraction from their versions of these maps and use a flux deboosting technique to account for any boosted flux where flux boosting is the preferential upward bias in measured source flux seen submillimetre/millimetre images due to weak sources coinciding with positive noise features in the map. Here I created a catalogue of sources with a signal to noise greater than 4 as seen in the S/N map by measuring the peak flux for each of these sources in order to make a comparison with the objects AU10 detected. As these are not flux deboosted the only useful information that can be gleamed from this comparison is the knowledge that the sources are visible in both reductions with similar non-deboosted fluxes.

The catalogues for each field for this reduction can be seen in Table 2.1 and Table 2.2, with the columns being: the identifier used (*ID*), the right ascension (*RA*) and declination (*Dec*) of the source, the peak flux for that source (*Flux*), the noise associated with it (*Noise*) and the corresponding signal to noise (*S/N*). There are 65 sources in the LH map and 44 in the SXDF map from the reduction above with a signal to noise of 4 or greater while AU10 detect 43 and 21 in the LH and SXDF fields respectively with a signal to noise of 4 or greater.

Table 2.1: LH sources with $S/N > 4.0$.

ID	RA	Dec	Flux (mJy)	Noise (mJy)	S/N
1	10:52:42.24	+57:12:38.17	3.90	0.97	4.0
2	10:51:52.56	+57:13:32.88	4.21	0.96	4.4
3	10:52:04.32	+57:13:40.80	4.43	0.95	4.7
4	10:50:59.76	+57:16:36.84	5.90	1.00	5.9
5	10:53:45.36	+57:16:42.96	4.24	0.95	4.5
6	10:53:21.84	+57:17:16.44	4.46	0.92	4.8
7	10:53:21.84	+57:17:16.44	4.46	0.92	4.8
8	10:53:18.96	+57:18:50.40	4.36	0.90	4.8
9	10:52:55.68	+57:19:55.56	4.60	0.91	5.0
10	10:54:06.24	+57:20:43.80	4.78	0.94	5.1
11	10:52:57.12	+57:21:03.61	8.35	0.91	9.2
12	10:51:53.28	+57:21:20.88	5.16	0.90	5.7
13	10:53:13.20	+57:21:26.99	4.00	0.89	4.5
14	10:50:41.28	+57:21:30.23	4.46	0.93	4.8
15	10:50:27.36	+57:21:45.73	4.48	1.03	4.3
16	10:53:25.68	+57:22:44.04	3.68	0.88	4.2
17	10:52:38.16	+57:23:24.00	4.21	0.90	4.7
18	10:52:38.64	+57:24:36.00	4.46	0.89	5.0
19	10:52:18.24	+57:24:36.71	3.88	0.89	4.4
20	10:52:01.20	+57:24:42.84	5.71	0.89	6.4
21	10:53:16.56	+57:25:10.57	3.62	0.87	4.1
22	10:53:43.92	+57:25:39.01	4.40	0.87	5.0
23	10:54:03.84	+57:25:48.00	6.26	0.88	7.1
24	10:53:51.60	+57:26:44.53	3.96	0.88	4.5
25	10:52:04.08	+57:26:58.92	5.22	0.89	5.9
26	10:54:35.28	+57:27:09.35	4.91	0.99	5.0
27	10:53:40.56	+57:27:49.32	3.76	0.86	4.4
28	10:51:00.96	+57:28:12.72	3.71	0.84	4.4
29	10:54:29.28	+57:29:09.96	3.78	0.94	4.0
30	10:50:23.52	+57:29:17.52	3.79	0.93	4.1
31	10:53:29.52	+57:29:30.12	3.76	0.85	4.4
32	10:50:49.92	+57:29:48.48	4.51	0.85	5.3
33	10:54:06.72	+57:29:53.52	4.38	0.88	5.0
34	10:53:07.20	+57:30:29.15	3.79	0.85	4.5

Table 2.1: Continued

ID	RA	Dec	Flux (mJy)	Noise (mJy)	S/N
35	10:53:51.36	+57:30:54.73	3.83	0.86	4.5
36	10:52:46.80	+57:31:19.93	3.59	0.85	4.2
37	10:51:31.44	+57:31:35.05	4.39	0.83	5.3
38	10:53:32.88	+57:31:45.84	3.49	0.85	4.1
39	10:53:10.56	+57:31:57.00	3.52	0.85	4.2
40	10:51:16.56	+57:32:08.88	3.95	0.83	4.8
41	10:53:41.76	+57:32:11.40	4.74	0.86	5.5
42	10:54:11.76	+57:32:55.31	3.91	0.90	4.4
43	10:54:06.72	+57:33:05.77	5.12	0.89	5.8
44	10:50:44.64	+57:33:18.36	6.72	0.86	7.8
45	10:52:14.40	+57:33:26.64	4.60	0.83	5.5
46	10:52:41.76	+57:34:06.24	3.65	0.84	4.3
47	10:53:49.68	+57:34:30.72	3.68	0.87	4.2
48	10:52:17.28	+57:35:00.60	5.00	0.83	6.0
49	10:52:42.00	+57:35:49.91	6.31	0.85	7.4
50	10:52:06.48	+57:36:23.04	7.46	0.83	8.9
51	10:51:30.00	+57:36:48.97	4.97	0.83	6.0
52	10:54:25.44	+57:37:00.12	5.03	1.17	4.3
53	10:52:25.44	+57:38:36.60	4.15	0.83	5.0
54	10:54:17.28	+57:38:34.81	4.80	1.19	4.0
55	10:52:20.40	+57:39:54.72	5.20	0.84	6.2
56	10:52:02.40	+57:40:49.09	7.64	0.84	9.1
57	10:51:48.24	+57:41:22.92	3.66	0.84	4.3
58	10:51:40.80	+57:43:23.16	5.57	0.94	5.9
59	10:52:15.60	+57:45:38.88	4.11	1.02	4.0
60	10:51:30.24	+57:38:07.08	3.90	0.84	4.6
61	10:52:56.16	+57:42:27.36	5.30	1.06	5.0
62	10:53:19.44	+57:21:05.03	4.25	0.91	4.4
63	10:52:56.40	+57:23:56.76	4.04	0.89	4.5
64	10:50:44.88	+57:36:50.39	4.25	0.97	4.4
65	10:51:16.32	+57:32:09.60	3.62	0.77	4.7

Table 2.2: SXDF sources with $S/N > 4.0$.

ID	RA	Dec	Flux (mJy)	Noise (mJy)	S/N
1	02:17:30.07	-05:09:50.94	6.70	1.44	4.6
2	02:18:25.30	-05:09:23.98	6.05	1.47	4.1
3	02:18:18.67	-05:08:24.00	5.74	1.40	4.1
4	02:18:01.39	-05:07:39.00	5.49	1.26	4.3
5	02:17:42.12	-05:07:23.99	5.40	1.35	4.0
6	02:17:27.46	-05:06:41.94	6.32	1.36	4.7
7	02:18:09.84	-05:04:45.01	5.07	1.22	4.1
8	02:17:43.54	-05:03:11.99	4.86	1.14	4.3
9	02:18:02.40	-05:00:18.00	4.84	1.04	4.6
10	02:18:42.36	-04:59:32.93	5.78	1.17	4.9
11	02:17:52.18	-04:58:54.01	4.47	1.04	4.3
12	02:17:16.44	-04:58:08.90	5.63	1.14	4.9
13	02:17:11.81	-04:57:50.90	4.96	1.20	4.1
14	02:18:20.06	-04:57:38.99	4.37	1.03	4.2
15	02:18:32.11	-04:56:29.94	4.12	1.01	4.1
16	02:17:42.12	-04:56:24.00	5.01	1.03	4.9
17	02:17:08.21	-04:56:17.88	5.77	1.21	4.8
18	02:18:16.06	-04:55:12.00	4.55	1.03	4.4
19	02:17:40.54	-04:55:02.96	4.34	1.01	4.3
20	02:18:29.30	-04:54:47.95	4.96	1.01	4.9
21	02:19:06.24	-04:53:32.82	7.17	1.52	4.7
22	02:18:27.89	-04:53:17.95	4.64	1.02	4.5
23	02:17:56.38	-04:52:45.01	4.74	1.00	4.7
24	02:18:18.86	-04:50:33.00	5.61	1.03	5.4
25	02:17:31.90	-04:50:26.95	4.72	1.02	4.6
26	02:17:45.74	-04:47:47.98	5.07	1.07	4.8
27	02:17:55.18	-04:47:24.00	4.85	1.05	4.6
28	02:17:39.94	-04:47:06.00	4.46	1.08	4.1
29	02:17:40.54	-04:46:12.00	5.13	1.10	4.7
30	02:19:01.42	-04:45:53.86	5.30	1.32	4.0

Table 2.2: Continued

ID	RA	Dec	Flux (mJy)	Noise (mJy)	S/N
31	02:17:47.35	-04:45:54.00	4.46	1.09	4.1
32	02:16:55.78	-04:45:32.80	6.47	1.35	4.8
33	02:17:38.71	-04:45:20.99	4.68	1.12	4.2
34	02:18:51.38	-04:44:56.90	5.28	1.28	4.1
35	02:17:54.77	-04:44:17.99	5.54	1.10	5.0
36	02:18:27.29	-04:43:38.96	4.73	1.18	4.0
37	02:16:56.59	-04:40:26.83	5.90	1.45	4.1
38	02:18:43.73	-04:38:56.94	6.27	1.43	4.4
39	02:18:13.25	-04:38:12.01	5.24	1.30	4.0
40	02:18:27.70	-04:37:14.99	5.83	1.41	4.1
41	02:17:23.88	-04:35:17.95	5.90	1.42	4.2
42	02:17:15.86	-04:34:08.94	5.84	1.44	4.1
43	02:18:28.68	-04:33:51.01	5.81	1.42	4.1
44	02:17:38.52	-04:33:30.02	6.84	1.39	4.9

Table 2.3 and Table 2.4 show those sources in this reduction that are also seen in AU10 with a signal to noise of 4 or greater. The columns of the table are the *ID* for comparison with the tables above of the full catalogue, the right ascension (*RA*) and declination (*Dec*) of the sources in this reduction, the non-deboosted peak flux (*Flux*), the noise (*Noise*) associated with that pixel and its signal to noise value (*S/N*) taken from this reduction, the name (*AU10 Name*) given to the source by AU10, the signal to noise value for that source in their map (S/N_{AU10}), the peak flux they found (S_{AU10}), the deboosted flux they calculated ($S_{deboost}$), the distance between the source positions in the two reductions (*Sep*). The final column is the ratio of AU10 flux to the flux I determined for source seen in both reductions. 29 of the LH detections and 15 of the SXDF sources seen in this reduction are within 9 arc-seconds or three pixel widths of an AU10 source. This leaves $\sim 19\%$ of the LH sources and $\sim 29\%$ of the SXDF sources, detected by AU10, undetected in this reduction. The higher fraction of LH sources detected is probably indicative of the lower noise levels in those maps when compared to the SXDF maps. It is worth

noting that the missing AU10 sources are detected in my maps but at signal to noise ratios in the 3.0 to 4.0 range. This seems to suggest that the differences in LH field are largely due to slightly different noise properties in the maps, while the two maps of the SXDF field are not as comparable because the larger number of smaller input observations over a larger area amplifies the affect of slightly differing sets of input observations.

The AU10 catalogues do not include 24 of the sources I detected at greater than four times the signal to noise in the LH field while they did not detect 29 of the sources in my catalogue in the SXDF field. That is 37% of my LH sources and 66% of the SXDF sources I detected. This is interesting as the reduction methods used the same pipeline and similar but not identical set of input observations. It is also possible that some of the parameters used in the reduction were marginally different such as the amount of sky noise removed by the PCA cleaning. AU10, however, did not just take the signal to noise of a source into account when compiling their catalogue they also calculated the probability that a source after deboosting would have had a negative flux ($P(S_{1100<0})$). Those sources with $P(S_{1100<0}) < 0.1$ were not included in the catalogues. This extra cut would explain at least some, if not all, of the extra sources seen in my catalogues.

The average difference in non-deboosted flux between the sources detected at $> 4\sigma$ seen in the AU10 reduction and my reduction is 0.19mJy for the LH field and 0.09mJy for SXDF. This is interesting as the SXDF map with its shallower depth appears to present more consistent results. The differences in flux are, with only a few exceptions, less than 1mJy and so at the suggested map noise levels or below them. Figure 2.8 is a plot of the non-deboosted flux taken from AU10 against the flux derived from the analysis in this chapter for the 4σ sources common to both catalogues. The LH sources are in blue while the SXDF sources are in green. The

Table 2.3: Matched LH sources with $S/N > 4.0$.

ID	RA	Dec	Flux (mJy)	Noise (mJy)	S/N	AU10 Name (AzTEC_)	S/N _{AU10}	S _{AU10} (mJy)	S _{deboost} (mJy)	Sep ($''$)	Flux Ratio
2	10:51:52.56	+57:13:32.88	4.21	0.96	4.4	105152.72+571334.5	4.07	4.12	2.65	2.1	0.98
4	10:50:59.76	+57:16:36.84	5.90	1.00	5.9	105059.75+571636.7	4.35	4.55	3.07	0.1	0.77
5	10:53:45.36	+57:16:42.96	4.24	0.95	4.5	105345.53+571647.0	4.69	4.71	3.37	4.3	1.11
6	10:53:21.84	+57:17:16.44	4.46	0.92	4.8	105321.96+571717.8	4.51	4.40	3.13	1.7	0.99
11	10:52:57.12	+57:21:03.61	8.35	0.91	9.2	105257.18+572105.9	7.50	7.25	6.21	2.4	0.87
12	10:51:53.28	+57:21:20.88	5.16	0.90	5.7	105153.10+572122.7	3.96	3.79	2.35	2.4	0.73
14	10:50:41.28	+57:21:30.23	4.46	0.93	4.8	105041.16+572129.6	4.22	4.15	2.73	1.1	0.93
17	10:52:38.16	+57:23:24.00	4.21	0.90	4.7	105238.35+572324.4	4.14	3.96	2.65	1.7	0.94
18	10:52:38.64	+57:24:36.00	4.46	0.89	5.0	105238.46+572436.8	4.49	4.26	3.01	1.6	0.96
20	10:52:01.20	+57:24:42.84	5.71	0.89	6.4	105201.14+572443.0	5.99	5.65	4.65	0.5	0.99
23	10:54:03.84	+57:25:48.00	6.26	0.88	7.1	105403.76+572553.7	6.36	5.92	4.91	5.8	0.95
25	10:52:04.08	+57:26:58.92	5.22	0.89	5.9	105203.89+572700.5	6.01	5.66	4.75	2.2	1.08
36	10:52:46.80	+57:31:19.93	3.59	0.85	4.2	105245.93+573121.2	4.19	3.75	2.51	7.1	1.04
37	10:51:31.44	+57:31:35.05	4.39	0.83	5.3	105131.41+573134.1	4.68	4.09	3.07	0.9	0.93
40	10:51:16.56	+57:32:08.88	3.95	0.83	4.8	105116.44+573209.9	4.04	3.54	2.35	1.4	0.90
41	10:53:41.76	+57:32:11.40	4.74	0.86	5.5	105341.50+573215.9	5.16	4.68	3.65	5.0	0.98
43	10:54:06.72	+57:33:05.77	5.12	0.89	5.8	105406.44+573309.6	5.51	5.14	4.15	4.5	1.00
44	10:50:44.64	+57:33:18.36	6.72	0.86	7.8	105044.47+573318.3	6.71	6.15	5.27	1.4	0.92
45	10:52:14.40	+57:33:26.64	4.60	0.83	5.5	105214.22+573327.4	5.70	4.98	4.09	1.6	1.08
46	10:52:41.76	+57:34:06.24	3.65	0.84	4.3	105241.87+573406.1	3.95	3.50	2.25	0.9	0.95
48	10:52:17.28	+57:35:00.60	5.00	0.83	6.0	105217.23+573501.4	5.37	4.69	3.79	1.0	0.94
49	10:52:42.00	+57:35:49.91	6.31	0.85	7.4	105241.89+573551.7	6.24	5.57	4.75	2.0	0.88
50	10:52:06.48	+57:36:23.04	7.46	0.83	8.9	105206.08+573622.6	8.21	7.23	6.43	3.2	0.97
51	10:51:30.00	+57:36:48.97	4.97	0.83	6.0	105129.55+573649.2	4.81	4.25	3.19	3.6	0.86
52	10:54:25.44	+57:37:00.12	5.03	1.17	4.3	105425.31+573707.8	4.22	5.18	3.13	7.7	1.03
53	10:52:25.44	+57:38:36.60	4.15	0.83	5.0	105225.16+573836.7	4.84	4.25	3.19	2.2	1.02
55	10:52:20.40	+57:39:54.72	5.20	0.84	6.2	105220.24+573955.1	5.18	4.58	3.61	1.3	0.88

Table 2.3: Continued

ID	RA	Dec	Flux (mJy)	Noise (mJy)	S/N	AU10 Name (AzTEC_)	S/N _{AU10}	S _{AU10} (mJy)	S _{deboost} (mJy)	Sep ($''$)	Flux Ratio
56	10:52:02.40	+57:40:49.09	7.64	0.84	9.1	105201.98+574049.3	8.24	7.39	6.63	3.4	0.97
58	10:51:40.80	+57:43:23.16	5.57	0.94	5.9	105140.64+574324.6	5.28	5.33	4.15	2.0	0.96
60	10:51:30.24	+57:38:07.08	3.90	0.84	4.6	105130.29+573807.2	5.39	4.80	3.79	0.4	1.23
61	10:52:56.16	+57:42:27.36	5.30	1.06	5.0	105256.32+574227.5	5.18	4.76	3.73	1.4	0.90
62	10:53:19.44	+57:21:05.03	4.25	0.91	4.4	105319.47+572105.3	5.05	4.75	3.61	0.4	1.12
63	10:52:56.40	+57:23:56.76	4.04	0.89	4.5	105256.49+572356.7	4.67	4.48	3.19	0.8	1.11
64	10:50:44.88	+57:36:50.39	4.25	0.97	4.4	105045.11+573650.4	4.28	4.09	2.73	1.9	0.96
65	10:51:16.32	+57:32:09.60	3.62	0.77	4.7	105116.44+573209.9	4.04	3.54	2.35	1.1	0.98

Table 2.4: Matched SXDF sources with $S/N > 4.0$.

ID	RA	Dec	Flux (mJy)	Noise (mJy)	S/N	AU10 Name AzTEC_	S/N _{AU10}	S _{AU10} (mJy)	S _{deboost} (mJy)	Sep ($''$)	Flux Ratio
5	02:17:42.12	-05:07:23.99	5.40	1.35	4.0	021742.13-050723.4	3.99	5.71	2.93	0.6	1.06
7	02:18:09.84	-05:04:45.01	5.07	1.22	4.1	021809.81-050444.8	3.99	5.04	2.63	0.3	0.99
10	02:18:42.36	-04:59:32.93	5.78	1.17	4.9	021842.39-045932.7	4.64	5.82	3.99	0.6	1.01
12	02:17:16.44	-04:58:08.90	5.63	1.14	4.9	021716.24-045808.4	4.13	5.03	2.93	2.9	0.89
16	02:17:42.12	-04:56:24.00	5.01	1.03	4.9	021742.10-045626.7	4.68	5.09	3.57	2.7	1.02
17	02:17:08.21	-04:56:17.88	5.77	1.21	4.8	021708.04-045615.3	4.25	5.52	3.29	3.6	0.96
18	02:18:16.06	-04:55:12.00	4.55	1.03	4.4	021816.07-045512.2	4.31	4.67	3.07	0.4	1.03
20	02:18:29.30	-04:54:47.95	4.96	1.01	4.9	021829.13-045448.2	4.15	4.42	2.83	2.6	0.89
21	02:19:06.24	-04:53:32.82	7.17	1.52	4.7	021906.24-045333.4	4.03	6.49	3.28	0.6	0.91
26	02:17:45.74	-04:47:47.98	5.07	1.07	4.8	021745.76-044748.8	4.85	5.44	3.99	0.4	1.07
27	02:17:55.18	-04:47:24.00	4.85	1.05	4.6	021754.97-044723.9	4.81	5.30	3.75	3.0	1.09
29	02:17:40.54	-04:46:12.00	5.13	1.10	4.7	021740.55-044609.1	4.14	4.81	2.93	2.8	0.93
32	02:16:55.78	-04:45:32.80	6.47	1.35	4.8	021655.80-044532.2	4.58	6.33	3.99	0.7	0.98
35	02:17:54.77	-04:44:17.99	5.54	1.10	5.0	021754.76-044417.5	4.14	4.78	2.93	0.4	0.86
44	02:17:38.52	-04:33:30.02	6.84	1.39	4.9	021738.52-043330.3	5.21	7.41	5.29	0.3	1.08

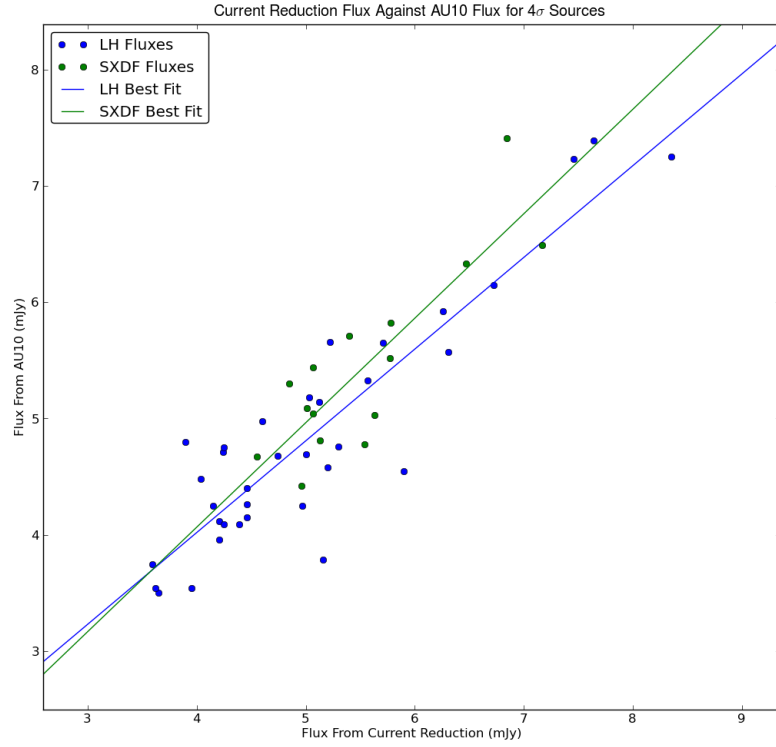


Figure 2.8: AU10 Flux Against This Reductions Flux for both the LH and SXDF fields with a line of best fit for each.

two lines are corresponding least squares fits to the two data-sets. There is a clear correlation between the measured fluxes. The slopes of the linear fits are 0.79 ± 0.06 and 0.89 ± 0.15 for the LH and SXDF fields respectively. This indicates that the flux for a given source recorded in the AU10 reduction is marginally lower than the flux for the same source as determined from the maps I produced. This might also help explain the extra sources I discovered assuming the signal to noise ratio was also slightly better in my reduction.

2.5 Discussion

In this chapter I describe the reduction of the AzTEC 1.1mm observations of the LH and SXDF areas. The intention was first to produce reliable maps of these two fields and second to provide an independent check of the reduction carried out by the team that developed the device. The noise levels of the maps in both reductions are similar as is the area of the maps covered by the 50% weight cut. There are differences in the number of sources seen in both reductions with more detected in this reduction. This would suggest that small differences and the data reduction procedure, such as slightly differing numbers of input maps can lead to significant changes in the numbers of detected sources. Those sources that are seen in both reductions however have similar non-deboosted fluxes. These points suggest that the my reduction produced maps with similar properties independently of the AzTEC instrument teams reduction if it is assumed that a significant number of the extra sources I detected were also detected by AU10 but ignored due to their extra analysis.

Chapter 3

Stacking Analysis

3.1 Introduction

In this chapter I will focus on faint sources detected in the AzTEC observations at 1.1mm of the Lockman Hole (LH) field, which were discussed in detail in the previous chapter. The negative K-correction at 1.1 millimetre and submillimetre wavelengths was introduced in chapter 1 with the suggestion that 1.1 millimetre observations, when compared with $850\mu\text{m}$ SCUBA observations, may allow detection of sources at greater redshifts. Another benefit that the AzTEC observations have over the previous SCUBA observations of this field by the SHADES collaboration is the larger area of the maps produced.

However, identifying counterparts for AzTEC sources from surveys at other wavelengths is difficult due to the large beam associated with observations at short millimetre and submillimetre wavelengths (SCUBA beam ~ 14 arcsec at $850\mu\text{m}$, Holland et al. (1999), AzTEC beam ~ 18 arcsec at 1.1mm, Wilson et al. (2008)). A

common technique for finding the counterparts is to use deep radio observations, due to the low surface density of radio sources, which makes it possible to unambiguously associate the radio and submillimetre/millimetre sources. The accurate radio position then makes it possible to find the optical/near-infrared counterpart. This approach has serious selection effects. Unlike in the submillimetre/millimetre, there is no helpful K-correction in the radio. For submillimetre/millimetre sources at redshifts greater than $z \approx 3$ there are few radio counterparts.

I use this approach, using other wavebands to identify submillimetre objects, in Chapter 5 to identify submillimetre and millimetre sources. With the noise characteristics of submillimetre/millimetre maps, sources have to be luminous in the submillimetre/millimetre to be detected and so are possibly not representative of the full population of galaxies at high redshift. The approach I describe in this chapter avoids these problems by looking at the average 1.1mm properties of sources identified in other wavebands. The luminous submillimetre galaxies detected in SCUBA surveys only contribute a few percent to the background (Chapman et al., 2005). This, coupled with the high SFRs seen in these luminous submillimetre galaxies (Dye et al., 2008), highlights the fact that this population may not be truly representative of the high redshift galaxy population and so may not be representative of the sources making up the FIRB.

The low signal-to-noise sources that are too faint to detect individually may be more representative of the galaxy population at high redshift. This chapter's primary aim is to investigate these fainter, harder to detect sources. To overcome the difficulties of detecting these low signal-to-noise objects, I use a technique known as stacking. In a stacking analysis, the average properties of the high redshift population are found by adding together small postage stamp images taken from the AzTEC image centred on the coordinates of known sources (in this case Spitzer

sources). The nature of the process does mean that while the average properties are discovered, the individual locations and other properties of the individual constituent sources are not determined.

Stacking of both optical and submillimetre images has been successfully used in the past to detect sources within images where no significant individual sources had been detected. Peacock et al. (2000) used this technique to probe the unresolved submillimetre background in Hubble images of the HDF. Serjeant et al. (2004) and Dye et al. (2006) used Spitzer source catalogues in a stacking analysis of SCUBA maps. Dye et al. (2007) used stacking to determine the contribution of $24\mu\text{m}$ and $8\mu\text{m}$ Spitzer sources and SCUBA sources to the CIB at $70\mu\text{m}$ and $160\mu\text{m}$.

In this chapter I will also investigate how the 1.1mm properties of Spitzer sources change with redshift. The redshifts used in this analysis are photometric redshifts determined by Dye et al. (2008) and described in more detail below. This chapter concludes with an estimation of the dust masses of the Spitzer sources.

3.2 Data

3.2.1 AzTEC Map

The AzTEC observations used for this analysis are discussed in Chapter 2. For commonality with analysis being carried out in other institutions the actual images used in this analysis were produced at the University of Massachusetts Amherst by the AzTEC instrument team (Austermann et al., 2010). The reduction process was similar to the steps I described in chapter 2. The map has a noise level of between 0.9mJy and 1.4mJy and covers an area of 0.31 square degrees.

3.2.2 Spitzer Source Lists

The IRAC (Fazio et al., 2004) source catalogue used in this work is taken from Dye et al. (2008). Images of the Lockman Hole were acquired in all four IRAC bands with an integration time of 500s per band. The 5σ point source detection limits in the 3.6, 4.5, 5.8 and $8\mu\text{m}$ wavebands are respectively 1.3, 2.7, 18 and $22\mu\text{Jy}$. Fluxes through an aperture of diameter $3''$ were computed from total fluxes extracted by the Spitzer Science Centre pipeline (Gordon et al., 2005). All bands were brought to the same effective seeing (see Dye et al., 2008, for further details).

I set flux limits on the catalogues of $1.1\mu\text{Jy}$ for the $3.6\mu\text{m}$ and $4.5\mu\text{m}$ bands, $4.6\mu\text{Jy}$ for the $5.8\mu\text{m}$ and $8\mu\text{m}$ bands and $60\mu\text{Jy}$ for the MIPS $24\mu\text{m}$ catalogue.

The Multiband Imaging Photometer for Spitzer (MIPS) (Rieke et al., 2004) source catalogue is that of Ivison et al. (2007). The data reach a 5σ point source detection limit of $55\mu\text{Jy}$.

The photometric redshifts used in this paper are those of Dye et al. (2008) derived by cross-matching the IRAC sources to sources detected in B , R , I and z band images obtained with the Subaru telescope and K band images obtained with the wide field camera on the United Kingdom Infrared Telescope (UKIRT). Redshifts were estimated by applying the *HyperZ* redshift code (Bolzonella et al., 2000) to this nine-band photometry, resulting in an average fractional error of $\sigma_z/(1+z)$ of 0.06. Further details of this redshift estimation can be found in Dye et al. (2008).

3.3 Stacking Method

The aim of the stacking analysis was to determine the average flux per Spitzer source in the AzTEC LH map. Using the catalogues, I compiled a list of the Spitzer sources that were within the area of the LH field surveyed by AzTEC. As described in the previous chapter, the AzTEC reduction produces three final FITS files of the field, a signal map, a signal-to-noise map and a weight map (Austermann et al., 2010). This weight map is the estimate of the error in the flux of each corresponding pixel in the signal map. The AzTEC pipeline describes it as a weight map, it is the inverse of the noise estimate squared.

I extracted a segment from the signal and weight map with sides of approximately 150 arcsecs around the centre position of each Spitzer source. I then produced a weighted sum of these maps using Equation 3.1, in which $(f_k)_{ij}$ is the flux of the k^{th} map at pixel ij , $(w_k)_{ij}$ is the weight, with $(w_k)_{ij} = \frac{1}{\sigma^2}$. The flux at the centre of the stacked map is the sum of the 1.1mm fluxes of all the Spitzer sources and the average 1.1mm flux of the Spitzer sources is obtained by dividing this flux by the number of Spitzer sources. The resulting stacked images can be seen in Figure 3.1.

$$(f_w)_{ij} = \frac{\sum_{k=0}^n (f_k)_{ij} (w_k)_{ij}}{\sum_{k=0}^n (w_k)_{ij}} \quad (3.1)$$

The significance of the stacked peak was calculated using the root mean square (rms) deviation of the background in the stacked image, and the flux for each stacked image was taken from the pixel in the centre of the stacked image. Sources

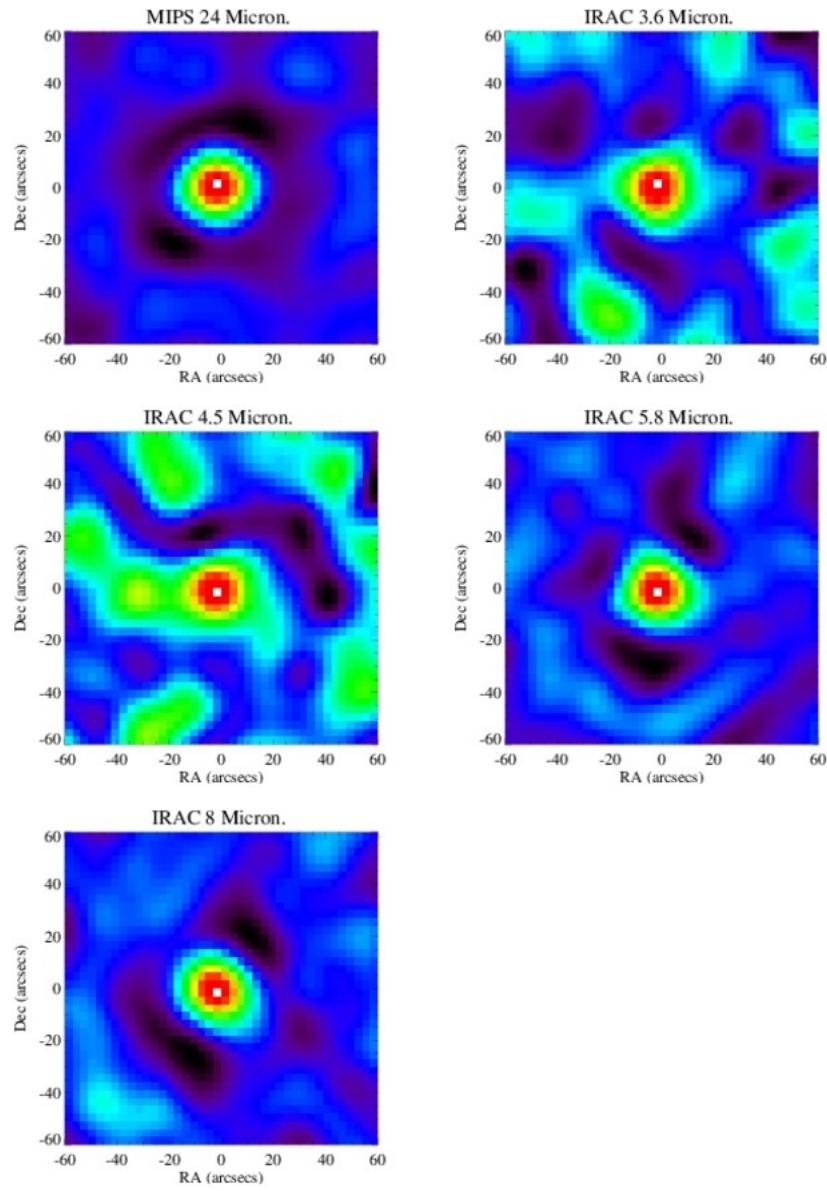


Figure 3.1: The plots of flux produced by stacking 1.1mm flux on catalogues of MIPS $24\mu\text{m}$, IRAC 3.6, 4.5, 5.8 and $8\mu\text{m}$ sources.

in the border of the map and sources in regions with uneven coverage were included in the analysis. With the use of the weighted flux per pixel, those sources that fall in regions of the map with relatively high noise contribute considerably less to the final flux values of the stacked image than those in regions of less noise. If there was 1.1mm emission at the Spitzer locations then it would be reasonable to expect a peak to be visible near the centre of the stacked images, which Figure 3.1 shows is the case. If there was no contribution from the Spitzer sources to the AzTEC map there should be no significant increase in the pixel values towards the centre of the stacked image. To confirm that the peaks in Figure 3.1 are not artefacts, the stacking analysis of the catalogues was repeated but this time a random shift was introduced in the positions of the sources, thereby creating a stacked image of random areas across the field. The stacked images had no discernible peaks in flux, showing that the peaks in Figure 3.1 are evidence that the Spitzer galaxies produce significant emission at 1.1mm.

3.4 Stacking the Full Catalogue

The initial stacking analysis was carried out on the full catalogues. The average 1.1mm flux values found for each of these catalogues can be found in Table 3.1; $N_{sources}$ is the number of sources in the catalogue, σ_{rms} is the noise level of the stacked image, S_{centre} is the average flux per Spitzer source in mJy and S/N is the Signal-to-Noise ratio.

Serjeant et al. (2008) carried out a similar stacking analysis using IRAC and MIPS catalogues on the SHADES 450 μ m and 850 μ m maps of the Lockman Hole field. Their measured mean 850 μ m flux is greater than the 1.1mm flux measured here.

Table 3.1: The average 1.1mm flux values found using the full catalogues.

Band	$N_{sources}$	σ_{rms} (mJy)	S_{centre} (mJy)	S/N
IRAC 3.6 μ m	8801	0.0118	0.064	5.37
IRAC 4.5 μ m	8580	0.0108	0.045	4.19
IRAC 5.8 μ m	4456	0.0142	0.163	11.50
IRAC 8 μ m	4280	0.0178	0.188	10.53
MIPS 24 μ m	6227	0.0150	0.257	17.00

This would be expected as the thermal radiation from dust enshrouded galaxies decreases with increasing wavelength past the wavelength of the peak in the dust spectrum. The two shortest IRAC wavelengths have the least significant detections ($5.4\sigma_{rms}$ for the 3.6 μ m and $4.2\sigma_{rms}$ for the 4.5 μ m) while the detections in the longer wavelength catalogues are the most significant.

3.4.1 Full Catalogue CIB Contribution

From the stacked images of the full catalogues the contribution that each of the Spitzer catalogues made to the 1.1mm background was determined and these results can be seen in Table 3.2. The CIB values of between $18JyDeg^{-2}$ and $24JyDeg^{-2}$ were taken from Scott et al. (2008) who sourced them from Puget et al. (1996) and Fixsen et al. (1998), with the lower value being taken from the former paper. There is a clear trend in the contributions with the MIPS 24 μ m sources contributing much more to the background than the shorter wavelength IRAC sources. This is to be expected since the 24 μ m emission is from dust whereas the 3.6 μ m emission is from stars. It is interesting that the stacking suggests the 4.5 μ m objects contribute less to the background than the 3.6 μ m galaxies while the contributions from the other bands increase with the wavelength of the band.

Table 3.2: Background contribution from the full catalogue stacking.

Band	Flux (JyDeg ⁻²)	Contrib _{min} (%)	Contrib _{max} (%)
IRAC 3.6 μ m	1.85	7.71	10.28
IRAC 4.5 μ m	1.28	5.35	7.13
IRAC 5.8 μ m	2.4	10.00	13.33
IRAC 8 μ m	2.65	11.05	14.74
MIPS 24 μ m	5.27	21.97	29.30

Scott et al. (2008) estimate the contribution from MIPS 24 μ m sources to the background using 1.1mm observations of the COSMOS field. They find that the contribution at 1.1mm from those 24 μ m sources that they detect with a signal-to-noise of 3.5 or greater in their 1.1mm image is between 5.3% and 7.1%. Without knowing the depth of their 24 μ m catalogue, it is difficult to compare their results with mine but it does suggest that a significant portion of the CIB at 1.1mm is from 24 μ m sources that are not detected individually by AzTEC.

Pascale et al. (2009) found that the contribution from their 24 μ m catalogue to the CIB at a redshift of 1.1 or greater decreased with wavelength. In their 500 μ m Balloon-borne Large-Aperture Submillimeter Telescope (BLAST) map they reported that the 24 μ m sources contributed 40% to the CIB. The fact that the 24 μ m contribution to the 1.1mm AzTEC is lower than this value, albeit for the full wavelength range, is encouraging as it agrees with the trend Pascale et al. (2009) discovered.

3.5 Stacking By Redshift

With photometric redshift information for 30% 24 μ m catalogues available to me courtesy of Dye et al. (2008) I performed an analysis to determine the redshift

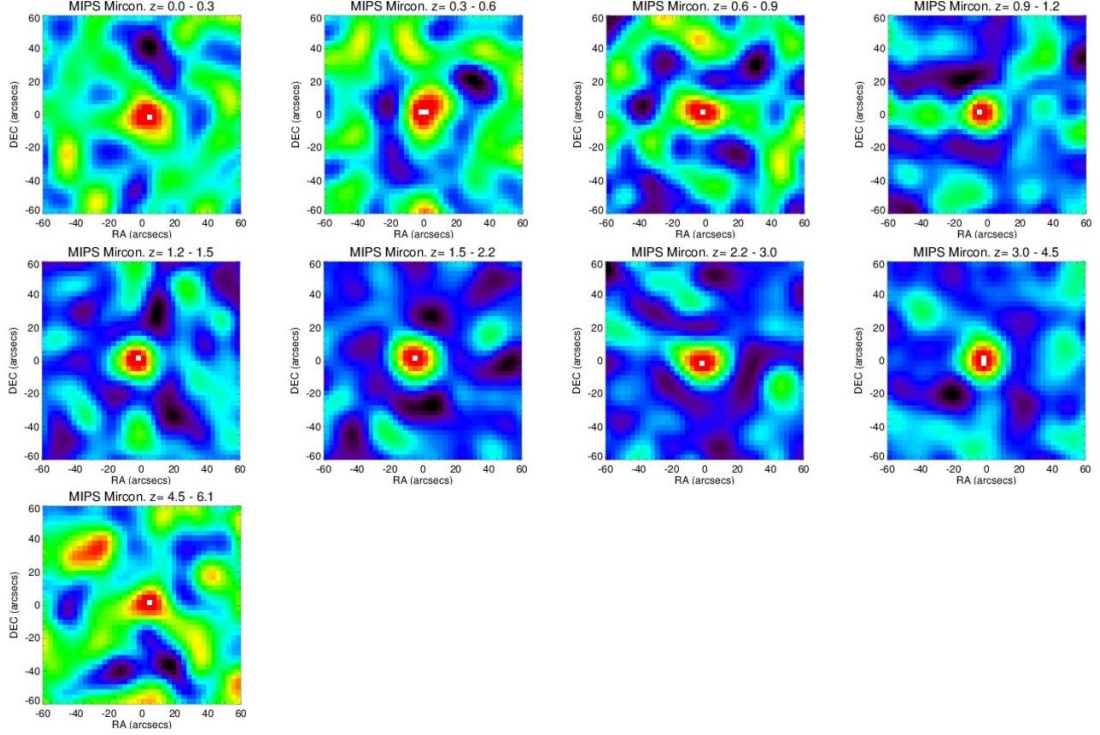


Figure 3.2: The plots of flux produced by stacking $24\mu\text{m}$ MIPS sources on the 1.1mm AzTEC image in redshift bins, from left to right $z= 0.0-0.3, 0.3-0.6, 0.6-0.9, 0.9-1.2, 1.2-1.5, 1.5-2.25, 2.25-3.0, 3.0-4.5, 4.5-6.1$.

dependence of the 1.1mm emission from the MIPS sources. The sources were split into nine redshift bins from 0.0 to 6.01 in redshift. The final bin extended to $z=6.1$ due to the fact that the most distant source had a redshift of 6.04. The stacking analysis described above was then repeated for each individual bin.

3.5.1 Redshift Dependence of Average Flux

The redshift stacked images can be seen in Figure 3.2 and Table 3.3 contains the average flux values associated with each image. The columns in the table are: the redshift bin (*Redshift Bin*), the number of sources contributing to the average flux (N_{sources}), the background noise level (σ_{rms}), the average flux in that bin (S_{centre})

Table 3.3: Redshift stacking data for MIPS 24 μ m.

Redshift Bin	$N_{sources}$	σ_{rms}	S_{centre} (mJy)	S/N
0.0–0.3	2194	0.025	0.086	3.34
0.3–0.6	634	0.043	0.151	3.54
0.6–0.9	298	0.057	0.194	3.42
0.9–1.2	887	0.034	0.159	4.72
1.2–1.5	710	0.037	0.214	4.61
1.5–2.25	548	0.060	0.323	5.39
2.25–3.0	217	0.085	0.417	4.91
3.0–4.5	347	0.080	0.448	5.57
4.5–6.1	88	0.139	0.371	2.67

and the signal-to-noise level of that flux value (S/N). There is a clear contribution seen in each redshift bin with the flux increasing out to the second last bin of 3.0–4.5.

The average contribution to the image increases with to the second last bin although the lower signal to noise and lower average flux in the last bin is possibly due to the low number of stacked sources. This is similar to the result seen by Pascale et al. (2009) in all but their 70 μ m data.

To see if there was any systematic difference between the objects with and without photometric redshifts, the stacking analysis was repeated first stacking only those without redshifts and then those with redshifts. There appeared to be no significant difference between the two samples.

3.5.2 CIB Contribution by Redshift

The contribution of the average flux in each of the redshift bins made to the background was calculated and can be seen in Table 3.4.

The results show that those galaxies that are in the lowest redshift band contribute more to the background than those with higher estimated redshifts. This is in agreement with the results of Pascale et al. (2009), who carried out a similar stacking analysis for the BLAST data at 250, 350 and 500 μ m. Ignoring that bin the contribution increases with redshift although there is a dip in the 2.25–3.0 bin.

3.5.3 Dust-Mass

With the contribution of the IRAC and MIPS sources to the millimetre image determined for each redshift bin, it is then possible to calculate the mass of dust that would be needed to produce this emission. The relation used to determine the dust mass in each redshift bin can be seen in Equation 3.2 with M_d being the mass of dust, S_ν the flux density, D the luminosity distance (with $H_0=71\text{km s}^{-1}\text{Mpc}^{-1}$, $\Omega_M=0.27$, $\Omega_\lambda = 0.73$), $\kappa_{\nu_{rest}}$ the dust mass-absorption coefficient at the rest frame frequency ν_{rest} , $B(\nu_{rest}, T_d)$ the value of the black-body function at ν_{rest} , the frequency of interest, and T_d the dust temperature, which is assumed to be 20K. This equation is based on the assumption that the mass of dust is optically thin (Eales & Edmunds, 1996).

$$M_d = \frac{S_\nu D^2}{(1+z)\kappa_{\nu_{rest}} B(\nu_{rest}, T_d)} \quad (3.2)$$

The luminosity distance was determined using the algorithm described in Wright (2006). The value of $\kappa_{\nu_{rest}}$ was extrapolated from the value found in James et al. (2002) at 850 μ m ($\kappa_{\nu_{850}} = 0.07 \pm 0.02\text{m}^2\text{kg}^{-1}$) using the relation given in Equation 3.3, with ν being the AzTEC frequency. The rest frame frequency was found

Table 3.4: The contribution to the background and dust mass within the individual redshift bins.

Redshift Bin	Flux (JyDeg ⁻²)	Contrib _{min} (%)	Contrib _{max} (%)	Dust Mass M _⊙
0.0–0.3	0.63	2.61	3.48	– 2.18x10 ⁷
0.3–0.6	0.32	1.32	1.76	3.82x10 ⁷ – 7.93x10 ⁷
0.6–0.9	0.19	0.8	1.06	1.02x10 ⁸ – 1.32x10 ⁸
0.9–1.2	0.47	1.94	2.59	1.08x10 ⁸ – 1.20x10 ⁸
1.2–1.5	0.50	2.09	2.79	1.62x10 ⁸ – 1.68x10 ⁸
1.5–2.25	0.58	2.43	3.24	2.54x10 ⁸ – 2.57x10 ⁸
2.25–3.0	0.30	1.24	1.66	3.32x10 ⁸ – 3.31x10 ⁸
3.0–4.5	0.51	2.14	2.85	3.56x10 ⁸ – 3.90x10 ⁸
4.5–6.1	0.11	0.45	0.60	3.23x10 ⁸ – 4.14x10 ⁸

using the familiar relation shown in Equation 3.4.

$$\kappa_{\nu_{rest}} = 0.07 \left(\frac{\nu}{350GHz} \right)^2 \quad (3.3)$$

$$z = \frac{\nu_{rest} - \nu}{\nu} \quad (3.4)$$

The dust mass is calculated for the maximum and minimum redshift for each bin and the values can be seen in the final column of Table 3.4. The analysis produces average dust masses for galaxies in the Spitzer catalogues using the stacked 1.1mm flux.

The dust masses calculated here are for the higher redshift sources are generally an order of magnitude greater than those estimated in Vlahakis et al. (2005) who measured the dust masses of an optically selected sample of galaxies in the local universe. They found a mean dust mass in their low redshift galaxy sample of $(2.34 \pm 0.36) \times 10^7 M_{\odot}$. In the two lowest redshift bins, however, the dust mass I

calculated seems to agree with their mean. Coppin et al. (2008) find dust masses for the galaxies seen in the SHADES data in the range 10^8 - $10^9 M_{\odot}$ with a median of $9 \times 10^8 M_{\odot}$. While the average dust masses calculated here are slightly lower, they are not wildly different. My stacking analysis shows that high dust masses are not just a feature of the most luminous submillimetre galaxies.

The general increase in the stacked dust mass with redshift would seem to agree with the investigation into the dust-mass function carried out by Eales et al. (2009). They find a strong evolution in the dust-mass function out to a redshift of 1 using data from the BLAST Redshift Survey, finding an increase in the space density of galaxies with large dust masses. Which agrees with the initial results derived from the Herschel Astrophysical Terahertz Large Area Survey (H-ATLAS) (Eales et al., 2010). Dunne et al. (2010) report that they see in the H-ATLAS data an increase in dust mass out a redshift of 0.5.

3.6 Summary

In this chapter I used stacking analysis to analyse the contribution Spitzer sources make to the 1.1mm AzTEC map of the LH field. The stacking of the catalogues for all four IRAC bands and the MIPS band show that there is a significant infrared contribution to the background at 1.1mm from the Spitzer galaxies. It has also been shown, when using the subset of objects with photometric redshifts, that while a significant proportion of the contribution to the CIB at 1.1mm is due to relatively low redshift sources the contribution in general increases with redshift. The contribution from the Spitzer sources to the CIB has been shown to be greater than that seen in Scott et al. (2008) although this is probably due to the fact they

summed the flux from those Spitzer sources actually detected at greater than 3.5σ at 1.1mm.

Chapter 4

Flux Ratio Analysis

4.1 Introduction

Eales et al. (2003) used the ratio of $850\mu\text{m}$ to $1200\mu\text{m}$ flux density to argue that some sources detected at 1.2mm by the Max-Planck Millimeter Bolometer (MAMBO) (Kreysa et al., 1998) detector on the Institut de Radioastronomie Millimétrique (IRAM) 30 meter telescope might be at very high redshift. Some of their estimates place objects at redshifts of 10. They make use of the fact that the ratio of $850\mu\text{m}$ flux to $1200\mu\text{m}$ flux is expected to change with redshift due to the increasing wavelength of the peak in the dust spectrum. In this chapter I use Spitzer IRAC (Fazio et al., 2004) observations of the field centred on Abell 2125 observed with MAMBO to test the conclusions of the Eales et al. (2003) paper. Two other possible explanations are that this anomalous flux ratio may be due to differing dust properties in the nearby, medium and high redshift universe or to technical problems with their flux measurements.

I also make use of the AzTEC Lockman Hole observations discussed in Chapter 2 to further this analysis, estimating the ratio of $850\mu\text{m}$ to 1.1mm flux in this field.

4.2 Estimating Redshifts

Eales et al. (2003) were interested in finding a method to estimate the redshifts to distant submillimetre sources because the ability to assign redshifts, and thus distances, to them is fundamental to the understanding of the development of galaxies. Redshifts of astronomical objects can be determined using a number of different approaches.

4.2.1 Spectroscopic Measurement

The traditional approach is to determine the actual wavelength shift of characteristic spectral lines in an observed spectrum. This technique however becomes increasingly difficult the fainter the object, due to intrinsically low luminosity or because of great distance. It is possible, with modern instruments, to determine spectroscopic redshifts for some relatively high redshift objects ($z \gtrsim 1$). However, for submillimetre sources with little optical flux, or for sources with no apparent optical identification, spectroscopically measuring the redshift is difficult, if not impossible.

4.2.2 Photometric Technique

With the exception of a small number of submillimetre galaxies that have spectroscopic redshifts, the spectra of the bulk of the submillimetre population can not be measured with sufficient accuracy to allow direct measurements of their redshift. Other approaches have been developed to try and determine redshifts for objects that are too faint to allow the spectroscopic technique. If an object has been imaged at multiple wavelengths, the flux measurements can be used to photometrically estimate the wavelength. By attempting to fit template SEDs to the observed data, making use of strong spectral features seen in the SEDs, this method can determine an approximate redshift. This approach has been used in chapters 3 and 5 with the aid of the photometric redshift package Hyper-Z (Bolzonella et al., 2000).

4.2.3 Submm to Radio Ratio

There have been a number of investigations into the possibility of using the ratio of radio to $850\mu\text{m}$ flux of a source to estimate its redshift. The technique assumes the tight correlation between radio and far infrared (IR) seen in nearby galaxies (for example: van der Kruit (1971); Condon et al. (1991)) is independent of redshift. This correlation and the different cosmological ‘K corrections’ in the submillimetre and the radio imply that the radio to sub-millimetre spectral index will depend on redshift. Carilli & Yun (1999) produced models of how the 1.4GHz to 350GHz spectral index ($\alpha_{1.4}^{350}$) for star-burst galaxies should vary with redshift. They concluded that a value of $\alpha_{1.4}^{350} \geq 0.5$ would be evidence that the source had a redshift ≥ 1 . They applied their method to the sources in the SCUBA image of the Hubble Deep Field in Hughes et al. (1998) to conclude that five of the sources in the deep

field are at $z \geq 1.5$ due to their spectral indices's being > 0.8 . This agrees with with the the photometric redshifts estimated for the optical counterparts, four of which are at $z > 2.0$ (Hughes et al., 1998). Rengarajan & Takeuchi (2001) also investigated the radio to sub-millimetre flux ratio in order to test how effective it is as a redshift indicator. They concluded that it is a useful tool in providing a crude estimate of the redshift. Smail et al. (2000), Ivison et al. (2002) and Ivison et al. (2007) also used this method to estimate redshifts for sub-millimetre sources detected in their respective observations and came to the conclusion that the median redshift for these sources is $\gtrsim 2.0$.

This method of estimating a submillimetre galaxy's redshift is clearly only useful for those sources that have secure radio identifications. This is a problem because a significant proportion of submillimetre galaxies do not have identifiable radio counterparts. Ivison et al. (2007), for instance, find that approximately one third of their catalogue does not have a robust 1.4GHz radio identification. A plausible explanation is that the submillimetre sources with no apparent radio emission may in fact be at much higher redshift than those that do have a radio identification, due to the rapid fall off in radio flux at higher redshifts ($\gtrsim 3.0$). This fall off in radio flux with increasing redshift can be seen in Figure 1.1, Chapter 1.

4.2.4 Submm to Millimetre Ratio

There has been less study into whether flux ratios within the millimetre and sub-millimetre bands can provide redshift estimates. Eales et al. (2003) attempted to address this using 1.2mm data from the MAMBO array coupled with SCUBA data at $850\mu\text{m}$. In their analysis they discovered high $1200\mu\text{m}$ to $850\mu\text{m}$ flux ratios and suggested two possible reasons for this: either the sources are at high redshift or

the properties of dust are evolving with redshift leading to significant differences between high and low redshift dust emission.

The advantage of the 1.1mm and 1.2mm bands over the radio 1.4GHz band is that these bands like the $850\mu\text{m}$ sample the galaxy's thermal dust emission (a modified black-body) whereas the 1.4GHz emission is synchrotron radiation. As stated above, the radio flux falls off dramatically with increasing redshift, imposing an upper limit on the maximum redshift attainable from the radio to submillimetre ratio method of approximately $z=3.0$. It is clear from Figure 1.1 that the 1.1mm and 1.2mm bands have a positive K-correction similar to the submillimetre. This suggests that the submillimetre to millimetre ratio method for estimating redshifts could be useful out to much greater distances.

An issue that arises when using the relationship between the radio and submillimetre/millimetre flux to estimate redshifts is that there is a degeneracy between the redshift of the galaxy and the temperature of the dust within the galaxy. This is related to the fact that the radio synchrotron emission is derived from shock heating of electrons while the submillimetre flux is derived from thermal emission from dust. If the dust was hotter or colder than is generally assumed, the submillimetre emission would change but the radio flux would not be directly effected. This suggests that for a given radio to submillimetre flux ratio a galaxy could either be at a high redshift with a dust temperature consistent with expectations or at a lower redshift but with a lower dust temperature than is normally assumed for submillimetre galaxies. The same degeneracy applies to the use of the submillimetre/millimetre ratio to estimate redshifts, since a high ratio of $1100\mu\text{m}$ to $850\mu\text{m}$ fluxes could be caused by a galaxy being at a very high redshift or by the galaxy being at a lower redshift containing cold-dust.

4.2.5 Spitzer IRAC Colours

Pascale et al. (2009) suggest a different method to determine approximate redshifts for galaxies that are detected in all 4 IRAC channels. They use IRAC colours of galaxies with known redshifts to estimate the redshift for those galaxies in their catalogue that are without redshifts.

4.3 Abell 2125 Observations

Data covering this field were available at 1.2mm (MAMBO), $850\mu\text{m}$ (SCUBA), 3.6, 4.5, 5.8, $8\mu\text{m}$ (IRAC) although the $5.8\mu\text{m}$ channel was unusable for reasons described below.

4.3.1 MAMBO

The MAMBO millimetre survey discussed in Eales et al. (2003) included three fields: the Lockman Hole (LH) field, the New Technology Telescope (NTT) Deep Field and a field centred on the Abell 2125 cluster. These observations were carried out during February and April of 1999 and from December 1999 to March 2000 and imaged a total area of approximately 300 square arc minutes to a 1σ level of 1mJy. Further details of the survey can be found in Bertoldi et al. (2002). MAMBO is a 1.2mm camera with 117 bolometers installed on the IRAM 30m telescope, which is situated at an altitude of 2850 metres on the Pico Veleta mountain in the Sierra Nevada mountain range. A total of 33 sources above a signal to noise ratio of 4.0 were included in this catalogue. These sources were used as targets for the SCUBA follow up observations using SCUBA's photometry mode. In photometry mode a

single bolometer is placed over the position of the source and its flux measured.

4.3.2 SCUBA

The SCUBA observations of these sources were taken over 14 nights between May 2001 and February 2002 and are discussed in Eales et al. (2003). These observations were in photometry mode, with a single bolometer pointed at the position of a MAMBO detection. The data were reduced using the standard method with the SCUBA User Reduction Facility (SURF) software package (Jenness & Lightfoot, 1997). The SCUBA detections used here are those primarily seen in the $850\mu\text{m}$ band due to the fact that only two of the MAMBO sources are detected in the $450\mu\text{m}$ observations (A2125-MM28 and A2125-MM11).

4.3.3 IRAC

The IRAC observations of Abell 2125 were publicly available in the Spitzer Data Archive. The observations were scheduled to observe this field as part of the follow up to the MAMBO survey and so covered the areas where the $1200\mu\text{m}$ and $850\mu\text{m}$ sources were detected. The New Technology Telescope deep field and the Lockman Hole field did not have Spitzer observations that overlapped the $1200\mu\text{m}$ and $850\mu\text{m}$ source positions. The Abell 2125 IRAC observations were taken on the 16th December 2004. They were taken in High Dynamic Range (HDR) mode with a five point Gaussian dither pattern and frame times of 30 seconds and 1.2 seconds. In HDR mode Spitzer takes two sets of observations, short exposure observations, 1.2 seconds in this case, and longer exposures, 30 seconds in this case. This dual exposure approach ensures that any over exposed pixels due to the bright cluster

will be identified and taken into account during the mosaicking process described below. I converted these data into a large image (§4.3.4).

4.3.4 IRAC Image Production

The IRAC Basic Calibrated Data (BCD) products for Abell 2125 were obtained from the Spitzer Data Archive using the Leopard retrieval program. This program along with Spot, the observation planning tool, is part of the *Spitzer Pride* package (<http://ssc.spitzer.caltech.edu/warmmission/propkit/spot/>). Post-BCD images were also retrieved from the archive. These are images that have been produced without using the full reduction pipeline and so are not suitable for use in scientific analysis. I used them to determine if the observed area overlapped with the MAMBO/SCUBA sources. Using Leopard and the post-BCD data, I discovered that the publicly available observations of the Lockman Hole field and the NTT field did not overlap with the submillimetre/millimetre sources but that the Spitzer observations of the Abell 2125 did cover the area of the MAMBO survey.

Artefact Mitigation

IRAC BCDs which have been calibrated using pipeline software earlier than version S18.0 have not normally had proper artefact removal performed on them. The different artefacts that can manifest themselves in IRAC data are described in the Spitzer IRAC Instrument Handbook (http://ssc.spitzer.caltech.edu/irac/iracinstrumenthandbook/IRAC_Instrument_Handbook.pdf). Removing these artefacts requires the use of third party contributed reduction tools available from the

Spitzer website (<http://ssc.spitzer.caltech.edu/dataanalysis/tools/contributed/irac/iracartifact/>). These tools can eliminate or reduce the magnitude of the common artefacts seen in IRAC images:

- mux-bleed or multiplexer bleed: a horizontal line of repeating bright patches in line with a bright source.
- column pull-down: a reduction in the intensity of the pixels in the same column as a bright source or cosmic ray artefact.
- banding: this artefact affects both rows and columns that contain a bright source. It produces vertical and horizontal lines of increased brightness that intersect the source.

These tools are individual programs, which are run in the correct sequence using a script provided. I discovered, however, that the script did not always reliably reduce the data and that it was often necessary to run the individual programs manually to ensure they executed correctly. The end result of the artefact correction are a set of image files (*over_cpr_sfx_SPITZER_I[1-4]....bcd.fits*), uncertainty files (*cor_sfx_SPITZER_I[1-4]....bunc.fits*) and bad pixel mask files (*SPITZER_I[1-4]....bimsk.fits*) that have been corrected for the artefacts mentioned above and have had their background levels adjusted so that when mosaicked together the final image will have a consistent background. As the data were taken in High Dynamic Range (HDR) mode there were extra steps in the process to account for the short and long exposures (Non-HDR IRAC imaging is the other observational mode and it produces a single set of exposures for each channel).

Mosaicking

IRAC produces a series of small individual images or frames when observing an area larger than the field of view of the telescope. These have to be combined to produce the final large image of the region being observed. To do this, the Spitzer instrument team has provided a software pipeline package. This package, the MOsaicker and Point source EXtractor (MOPEX), consist of a series of scripts and IDL programs that can be configured and run using a Java front end user interface. It allows the user to perform background matching on individual frames and perform both temporal and spatial outlier rejection to reduce or remove the effects of cosmic rays and other transient/instrument artefacts that are not handled by the contributed software tools. The end result is a mosaicked image, a coverage map indicating the number of individual observations that make up different portions of the mosaic, and a noise map showing the statistical uncertainty associated with each pixel value in the mosaic.

Initially an attempt was made to produce a mosaic using the method suggested on the Spitzer MOPEX website for dealing with medium to high coverage data. This produced a mosaic in which some of the artefacts remaining after the initial mitigation were exaggerated. An investigation pointed to the problem being a relatively low coverage dataset, with a coverage of less than 10 frames per pixel. A second more successful attempt to produce mosaics used the default values presented by MOPEX which are more suited to fields with lower overall coverage.

The production of a mosaic involves several processing steps. The first step uses the overlap correction module to correct for background differences between the different individual images. This is not completely necessary when using the contributed artefact mitigation code as that also carries out overlap correction and its

author suggests the results are comparable to those obtained with MOPEX. The MOPEX module first interpolates the exposures onto a common grid and then it minimises the differences in the overlapped regions pixel by pixel.

With the overlap correction determined, the next stage in the MOPEX pipeline is the mosaic module. This module carries out a number of different operations on the data prior to mosaicking. The main purpose of these is to detect artefacts in the images and flag them so that they can be masked in the final mosaicked image. The background is initially subtracted using median filtering to aid the detection of significant artefacts and the individual images are once again interpolated onto a common grid as in the overlap correction module (this is because the mosaic and overlap modules are independent). The modules *detect*, *dual outlier* and *mosaic projection* then perform outlier rejection using both spatial and temporal information. All the information about outliers within the images are combined into an *R-mask* which is then used by the *re-interpolate module* to reject the detected outliers.

Finally the individual images are combined using *Mosaic CoAdder* into larger image tiles which are then combined in *Mosaic Combine* into the final single image along with the corresponding uncertainty and coverage maps.

The IRAC 5.8 μ m image was badly effected by the *first frame effect* artefact leading to a strong gradient across the image rendering it unusable without further correction. Unlike the non-HDR observations described in Chapter 5 there was no software in the pipeline to remove this effect. Due to time constraints an algorithm to rectify this was not developed and this channel was not used in the analysis below.

4.3.5 Counterparts

Figures 4.1, 4.2 and 4.3 show postage stamps for each of the 11 sources that Eales et al. (2003) observed in the Abell 2125 field. The circles (and images) are centred on the positions reported in Eales et al. (2003) and are 5'' in radius, while the images are 40''x40''. All the positions except for A2125-MM29 were determined using 1.4GHz Very Large Array (VLA) observations. The position of A2125-MM29 position was determined using the Plateau de Bure millimetre interferometer.

Source extraction within the IRAC images was carried out using the SExtractor program (Bertin & Arnouts, 1996). For the three IRAC bands the detection threshold was set at twice the noise level. SExtractor detected a total of 24803, 11193 and 5062 sources in the 3.6 μ m 4.5 μ m and 8 μ m fields respectively. Using the positions of the sources detected by SExtractor and those of the 11 joint SCUBA/MAMBO sources reported in Eales et al. (2003) I determined that there was a possible IRAC source in at least one of the bands for eight of the SCUBA/MAMBO sources. The angular separations between the nearest IRAC sources and the SCUBA/MAMBO positions can be seen in Table 4.1. Those that have angular separations $\lesssim 1$ arcsec are considered to be possible counterparts. The AB magnitudes of those that are considered counterparts can be seen in Table 4.2. The positions reported by Eales et al. (2003) are radio positions for potential counterparts and so are comparatively accurate (sub arc-second accuracy compared to SCUBA or MAMBO derived positions which are accurate at most to several arc-seconds). Therefore, an in-depth analysis of the chance of a coincidence is not needed, unlike in Chapter 5 where the large beam associated with SCUBA observations introduced a large uncertainty in positions. The probability that an IRAC source falls within 1 arcsec of a SCUBA/MAMBO source by chance is: $P_{3.6\mu m}(<1'')=0.018$, $P_{4.5\mu m}(<1'')=0.008$,

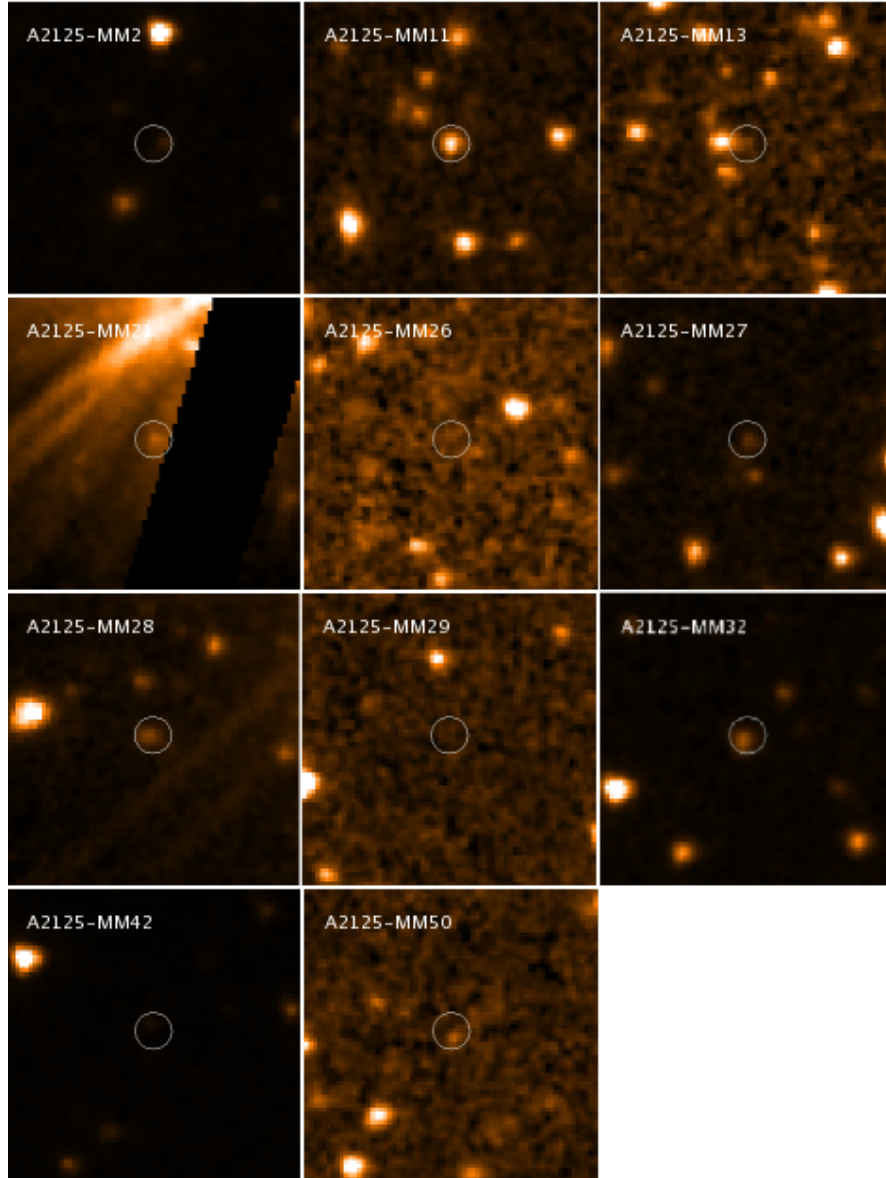


Figure 4.1: Abell 2125 3.6 μm postage stamps (40''x40'') with 5'' circles centered on the 1.4GHz VLA/Plateau de Bure position reported in Eales et al.(2003)

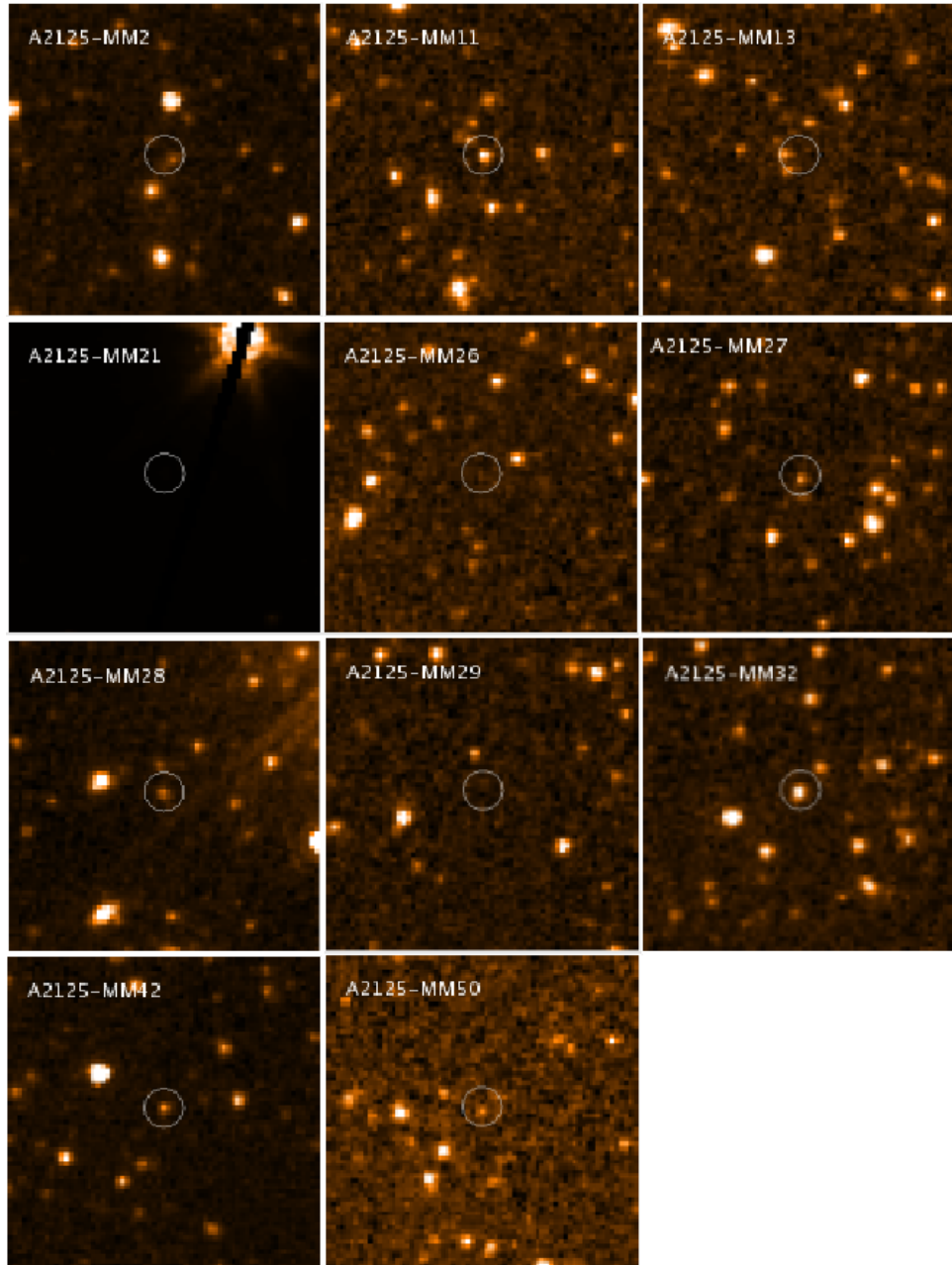


Figure 4.2: Abell 2125 $4.5\mu\text{m}$ postage stamps ($40''\times 40''$) with $5''$ circles centred on the 1.4GHz VLA/Plateau de Bure position reported in Eales et al.(2003).

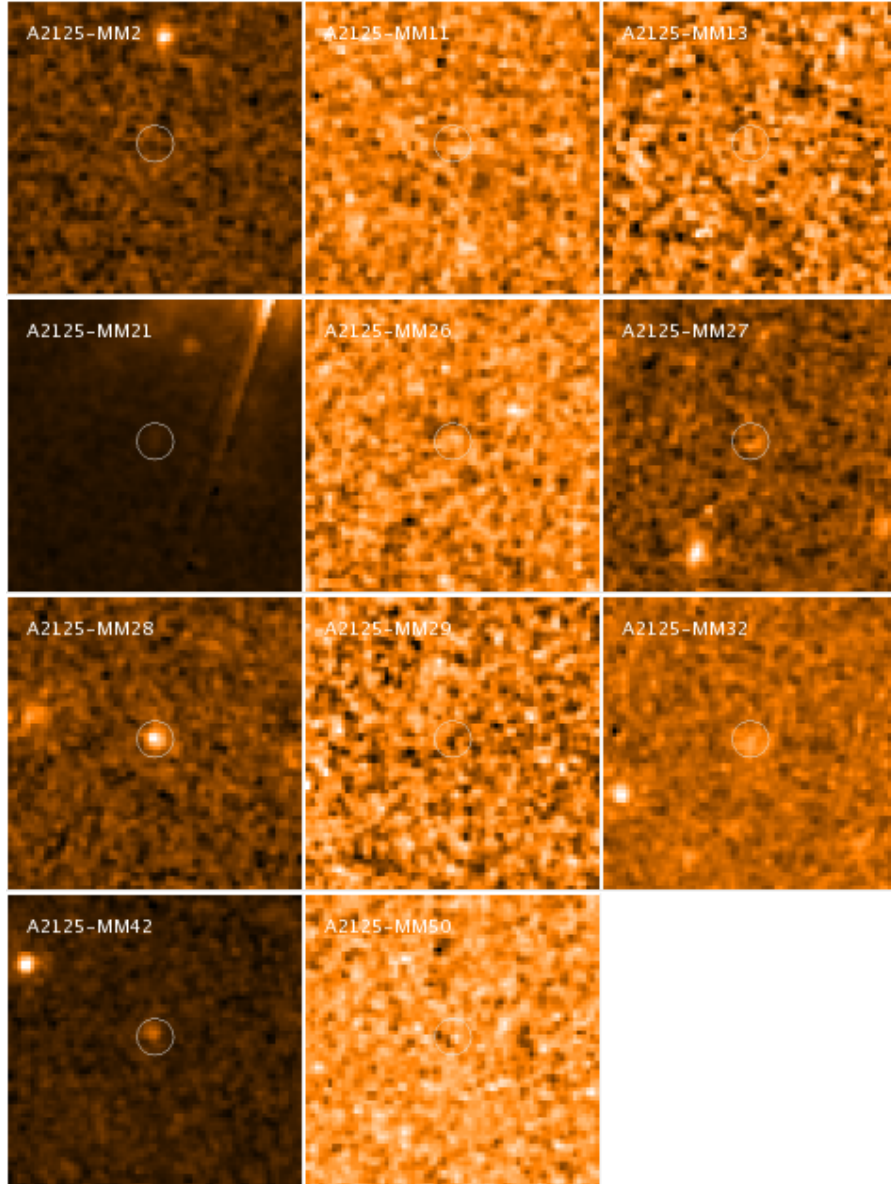


Figure 4.3: Abell 2125 $8\mu\text{m}$ postage stamps ($40''\times 40''$) with $5''$ circles centred on the 1.4GHz VLA/Plateau de Bure position reported in Eales et al.(2003).

Table 4.1: IRAC associations for SCUBA/MAMBO sources.

ID	RA_{Radio}	Dec_{Radio}	Sep _{3.6} (")	Sep _{4.5} (")	Sep ₈ (")	Counterpart
mm2	15:39:58.10	+66:13:36.9	2.9	1.2	—	*
mm11	15:40:47.19	+66:15:51.8	0.3	0.1	—	*
mm13	15:40:49.42	+66:20:15.1	4.2	4.1	—	
mm21	15:41:17.85	+66:22:33.7	—	—	0.6	*
mm26	15:41:26.9	+66:14:37.3	3.2	—	—	
mm27	15:41:27.29	+66:16:17.0	0.1	0.2	—	*
mm28	15:41:28.78	+66:22:03.7	0.4	0.6	0.3	*
mm42	15:42:10.66	+66:21:13.0	1.3	1.1	1.0	*
mm50	15:42:20.27	+66:07:16.0	0.5	0.7	—	*
mm32	15:41:42.83	+66:05:59.0	1.0	1.0	0.8	*
mm29	15:41:38.18	+66:08:01.2	—	—	—	

and $P_{8\mu m}(<1'')=0.004$. So there is at most a $\sim 2\%$ chance that one of the IRAC sources within 1 arcsec of a submillimetre source is a chance association rather than being a true counterpart to it.

4.3.6 Flux Ratios

Eales et al. (2003) produced estimates of the redshifts for the objects in their survey using the ratio of $1200\mu m$ MAMBO to $850\mu m$ SCUBA flux and templates taken from the SCUBA local universe galaxy survey (SLUGS) (Dunne & Eales, 2001). Table 4.3 is taken from that paper and shows the estimated redshifts using both 1.4GHz to $1200\mu m$ flux ratios (z_{radio}) and $1200\mu m$ to $850\mu m$ ratios ($z_{1.2mm/850\mu m}$). It is clear from this table that the estimated redshifts from the submillimetre to millimetre flux ratio do have rather large error estimates. What is equally clear, however, is that the redshifts are also large when compared to the radio estimates and to the median redshifts other surveys have determined, $z_{median} \sim 2$ (Chapman et al., 2003, 2005; Aretxaga et al., 2007; Wardlow et al., 2010).

Table 4.2: The Magnitudes of the IRAC counterparts to the Eales et al. (2003) sources.

ID	Mag _{3.6}	Mag _{4.5}	Mag ₈
mm2	20.4 ± 0.6	21.3 ± 0.9	—
mm11	19.9 ± 0.5	21.6 ± 1.1	—
mm21	—	—	19.3 ± 0.4
mm27	21.4 ± 0.5	21.9 ± 1.3	—
mm42	20.8 ± 0.9	21.6 ± 1.1	19.5 ± 0.4
mm32	19.7 ± 0.47	20.9 ± 0.8	19.7 ± 0.5
mm50	22.2 ± 1.48	22.9 ± 2.0	—

Ideally I would have used the IRAC colours and the method described by Pascale et al. (2009) to estimate the redshifts of the counterparts and compare these with the redshifts estimated by Eales et al. (2003). However, the contamination of the $5.8\mu\text{m}$ image made this impossible. Instead, I have used the magnitudes themselves to see if the high redshifts in Table 4.3 are plausible.

A useful dataset with which to compare the Abell 2125 dataset is the SHADES survey of the Lockman Hole (LH) for which Dye et al. (2008) have estimate photometric redshifts from the optical and infrared photometry of the counterparts. Figure 4.4 shows, for each IRAC band (from the top: $3.6\mu\text{m}$, $4.5\mu\text{m}$ and $8\mu\text{m}$), the IRAC magnitudes plotted against the photometric redshifts determined by Dye et al. (2008) for the sources they describe as having reliable radio counterparts (blue stars) in the area of the Lockman Hole field surveyed by the SHADES consortium. Also plotted in this figure are the magnitudes for those Abell 2125 SCUBA/MAMBO sources that have nearby IRAC sources plotted against the redshift Eales et al. (2003) estimated using the 1.4GHz to 1.2mm flux ratio technique (green triangles).

All three sub-figures show the radio to millimetre or submillimetre redshift estimation method produces redshifts for the sources that place them in the same area of the magnitude redshift diagram as those with photometric estimates from Dye

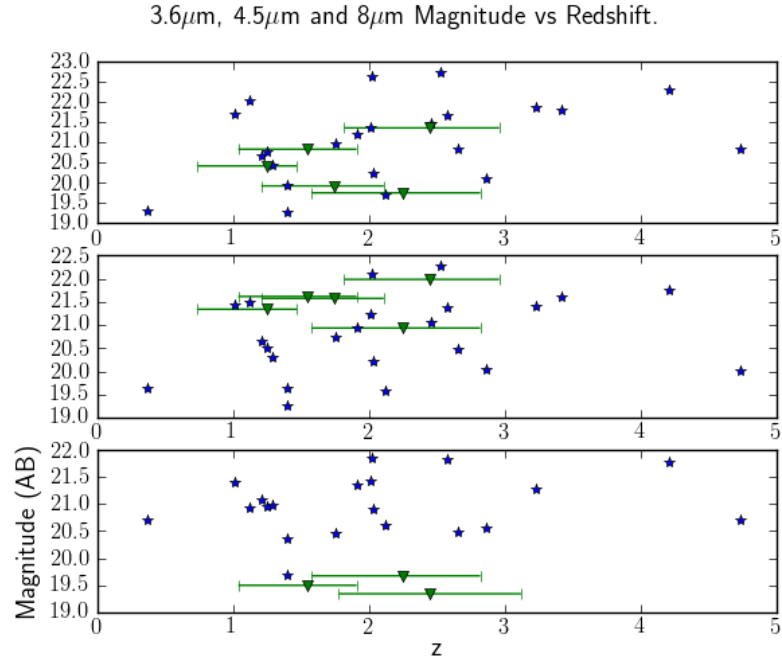


Figure 4.4: From the top to the bottom image: 3.6 μ m 4.5 μ m 8 μ m IRAC AB magnitude vs the redshift estimated by Dye et al. (2008) (blue stars), 1.2mm to 850 μ m flux ratio (red squares) and 1.4Ghz to 1.2mm flux ratios (green triangles)

et al. (2008). This comparable set of magnitudes would suggest that the Abell 2125 sources are at moderate redshift rather than the higher redshifts suggested by Eales et al. (2003).

4.4 Lockman Hole Observations

The fact that the galaxies from Eales et al. (2003) appear to be at moderate redshift raises the question of whether their high values of 1200 μ m/850 μ m flux ratio are genuine or whether they were caused by technical issues associated with the observations. To address this question, I used the AzTEC and SCUBA images of the LH field to carry out a new investigation of the 850 μ m to 1.1mm flux ratio.

Table 4.3: Taken from Eales et al. (2003) (part of their Table 3). Redshift estimates using 1.4GHz/1200 μ m and 1200 μ m/850 μ m flux ratios.

Name	z_{radio}	$z_{1.2mm/850\mu m}$
A2125-MM2	$1.25^{+0.51}_{-0.22}$	$10.35^{+\infty}_{-6.04}$
A2125-MM11	$1.75^{+0.54}_{-0.36}$	>9.65
A2125-MM13	$2.05^{+0.64}_{-0.72}$	$1.55^{+5.11}_{-1.55}$
A2125-MM21	$2.45^{+0.67}_{-0.67}$	$3.95^{+8.44}_{-2.83}$
A2125-MM26	$2.25^{+0.63}_{-0.51}$	$1.85^{+1.92}_{-1.61}$
A2125-MM27	$2.45^{+0.63}_{-0.51}$	<1.0
A2125-MM28	$0.55^{+0.22}_{-0.28}$	$3.45^{+\infty}_{-3.45}$
A2125-MM42	$1.55^{+0.51}_{-0.36}$	>3.65
A2125-MM50	$3.15^{+0.85}_{-1.0}$	$10.15^{+\infty}_{-8.10}$
A2125-MM32	$2.25^{+0.67}_{-0.57}$	$9.85^{+\infty}_{-7.53}$

4.4.1 AzTEC

Chapter 2 describes the 1.1mm observations of this field with the AzTEC camera on the JCMT and the subsequent reduction of those observations. The observations mapped an area of 0.31 square degrees largely centred on the area surveyed by the SHADES survey at 850 μ m. For consistency the officially released AzTEC maps and catalogue of this field (Austermann et al., 2010) were used in this analysis rather than those produced in chapter 2. The map has a noise level of between 0.9mJy and 1.4mJy.

4.4.2 SCUBA

The 850 μ m source catalogue was taken from SCUBA 850 μ m observations of the Lockman Hole taken as part of the SHADES survey. These observations covered an area of 485 square arc minutes centred on $10^h 52^m 26.7^s$ in right ascension and $57^\circ 24' 12.6''$ in declination. This set of observations produced maps with an rms noise level of ~ 2 mJy. The survey is described in detail in several papers:

Mortier et al. (2005); Coppin et al. (2006); Ivison et al. (2007); Aretxaga et al. (2007); Takagi et al. (2007); Coppin et al. (2008); Dye et al. (2008); Serjeant et al. (2008). The $850\mu\text{m}$ fluxes from the LH SHADES catalogue are the corrected fluxes as determined by Coppin et al. (2006) using the de-boosting method described in Coppin et al. (2005).

The production of the $850\mu\text{m}$ catalogue used in this analysis is discussed in detail in Coppin et al. (2006). The catalogue contains 60 sources with a signal to noise ratio ≥ 3 . As part of the source extraction, Coppin et al. (2006) found $24\mu\text{m}$ and 1.4GHz counterparts for these sources in an attempt to assign more accurate positions to the SCUBA sources using a statistical method to find the probability that the coincident $24\mu\text{m}$ and 1.4GHz sources are not associated the submillimetre source. They considered a source to have a *robust* counterpart if the probability (P) of it being a false coincidence was ≤ 0.05 and it was within $8''$ of the SCUBA position; they classified those sources within $8''$ of the SCUBA position but with a $P > 0.05$ as *non-robust*. The method for finding P is similar to the Monte Carlo analysis described in §5.3.

4.4.3 Flux Ratios

Two possible remaining explanations of the low $850\mu\text{m}/1200\mu\text{m}$ ratios found by Eales et al. (2003) are instrumental effects produced by combining point photometry at $850\mu\text{m}$ with imaging at $1200\mu\text{m}$ or evolution in the dust properties. Although Eales et al. (2003) made exhaustive checks in order to rule out the first possibility it is still possible this is the case. It is also worth noting that galaxies detected in 1.2mm observations are likely to be a higher redshifts than those submillimetre selected galaxies that have radio identifications due to the fact that there is a fall

Table 4.4: SCUBA detections with robust radio identifications from Dye et al. (2008) with corresponding 1.1mm pixel values.

ID	RA	Dec	S/N _{1.1}	S _{1.1} (mJy)	S ₈₅₀ (mJy)	Z _{photo}	S _{1.1} /S ₈₅₀
LOCK 850.1	10:52:01.25	+57:24:45.76	5.5	5.2	8.85	4.21 ^{+0.24} _{-1.80}	1.70±0.37
LOCK 850.2	10:52:57.08	+57:21:02.82	7.2	7.0	13.45	3.32 ^{+0.02} _{-0.56}	1.92±0.40
LOCK 850.3	10:52:38.30	+57:24:35.76	4.5	4.3	10.95	1.21 ^{+0.04} _{-0.09}	2.55±0.72
LOCK 850.4	10:52:04.08	+57:26:58.52	5.9	5.5	10.65	2.66 ^{+0.19} _{-0.41}	1.94±0.47
LOCK 850.6	10:52:04.01	+57:25:24.20	3.5	3.1	6.85	2.01 ^{+1.17} _{-0.20}	2.21±0.76
LOCK 850.7	10:53:00.96	+57:25:52.06	1.9	1.8	8.55	—	>3.04
LOCK 850.9	10:52:15.64	+57:25:04.26	0.6	0.6	5.95	1.62 ^{+0.08} _{-0.25}	>2.07
LOCK 850.10	10:52:48.99	+57:32:56.26	2.4	2.1	9.15	—	>3.50
LOCK 850.12	10:52:27.58	+57:25:12.46	2.3	2.2	6.15	2.03 ^{+0.30} _{-0.20}	>2.15
LOCK 850.15	10:53:19.27	+57:21:08.45	5.1	4.3	13.25	2.53 ^{+0.41} _{-0.45}	3.08±1.07
LOCK 850.16	10:51:51.69	+57:26:36.09	0.4	0.4	5.85	1.25 ^{+0.13} _{-0.20}	>2.38
LOCK 850.17	10:51:58.02	+57:18:00.27	2.7	2.7	4.75	1.12 ^{+0.26} _{-0.12}	>1.61
LOCK 850.18	10:52:27.78	+57:22:18.18	2.5	2.4	6.05	—	>2.07
LOCK 850.24	10:52:00.45	+57:20:40.16	1.0	0.9	2.75	1.40 ^{+0.09} _{-0.15}	>0.98
LOCK 850.26	10:52:40.70	+57:23:09.96	0.9	0.9	5.85	2.86 ^{+0.33} _{-1.02}	>1.97
LOCK 850.30	10:52:07.49	+57:19:04.01	1.2	1.2	4.75	2.06 ^{+0.50} _{-0.21}	>1.57
LOCK 850.31	10:52:15.99	+57:16:19.34	2.6	2.5	6.05	2.12 ^{+0.17} _{-0.19}	>2.08
LOCK 850.33	10:51:55.47	+57:23:12.77	3.4	3.2	3.85	2.58 ^{+0.40} _{-0.60}	1.20±0.47
LOCK 850.34	10:52:14.20	+57:33:28.30	5.7	5.0	14.05	3.42 ^{+0.27} _{-0.27}	2.81±0.78
LOCK 850.37	10:51:24.34	+57:23:36.18	0.4	0.3	7.55	—	>2.94
LOCK 850.40	10:52:01.72	+57:19:17.00	1.3	1.3	3.05	2.02 ^{+0.06} _{-0.15}	>1.02
LOCK 850.41	10:52:59.76	+57:24:24.94	1.6	1.5	3.85	1.01 ^{+0.10} _{-0.19}	>1.34
LOCK 850.52	10:52:45.81	+57:31:19.86	4.1	3.7	3.95	1.24 ^{+0.06} _{-0.09}	1.07±0.55
LOCK 850.63	10:51:54.26	+57:25:02.55	2.3	2.1	3.65	4.73 ^{+0.16} _{-0.11}	>1.30
LOCK 850.71	10:52:19.09	+57:18:57.87	3.6	3.6	3.95	1.91 ^{+0.16} _{-0.15}	1.10±0.52
LOCK 850.73	10:51:41.99	+57:22:17.52	1.5	1.4	3.55	1.40 ^{+0.10} _{-0.09}	>1.24
LOCK 850.77	10:51:57.15	+57:22:09.58	1.5	1.4	3.25	1.76 ^{+0.12} _{-0.08}	>1.12
LOCK 850.87	10:51:53.37	+57:17:30.05	3.3	3.3	3.45	2.46 ^{+0.35} _{-0.34}	1.05±0.51

off in radio flux at high redshift ($z \sim 3.0$). To test this further I used the AzTEC data for the LH field along with published SCUBA $850\mu\text{m}$ results for the same field.

A difficulty in measuring source fluxes in submillimetre and millimetre maps is a phenomenon known as flux boosting. This is an effect that leads to the upward biasing of fluxes measured for sources detected in submillimetre and millimetre images due to source confusion and other sources of noise in the images. Eales et al. (2000) modelled this effect using Monte Carlo simulations of an image taken as part of the Canada UK Deep Submillimetre Survey (Eales et al. (1999), further details of this survey can be found in Chapter 5). They determined that their flux measurements are on average 1.44 times the true source flux. Scott et al. (2002) did a similar analysis for the SCUBA 8-mJy survey data and concluded that flux boosting could lead to over-estimates of source flux by approximately 15%. The disparity in these two results suggests that the amount of flux boosting is dependent on a number of factors (survey depth, survey area etc.) and that simulations would be needed to determine the correct boosting factor for different fields and surveys.

If we use a submillimetre/millimetre image to measure the flux of a galaxy found from a survey in a different waveband (for example optical), the error on the flux is equally likely to be positive as negative. We can therefore partially overcome the problem of flux boosting by measuring the 1.1mm flux at the exact position of the radio counterpart because there is then no bias in the flux. I have therefore measured the 1.1mm fluxes of the SHADES sources in the Lockman Hole field at the co-ordinates of what Dye et al. (2008) describe as their robust radio identifications. I determined the signal to noise values by reading the pixel value at the same position in the AzTEC 1.1mm S/N map. This assumes that the ra-

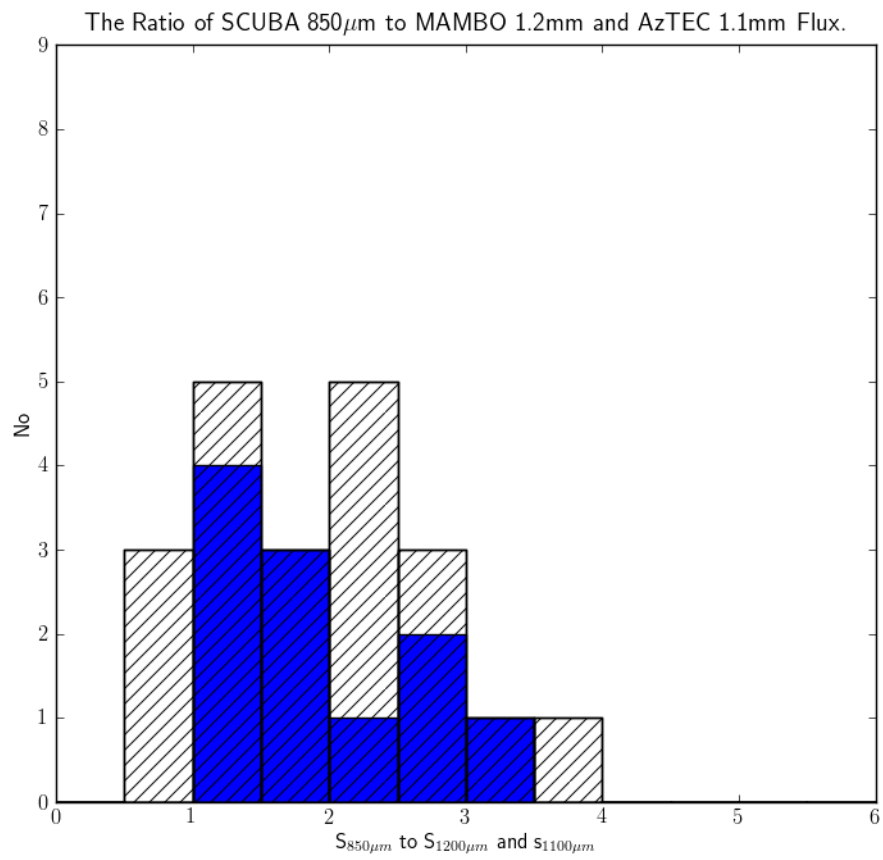


Figure 4.5: A histogram of the $850\mu\text{m}$ to 1.2mm flux ratio found in Eales et al. (2003) (hatched histogram) and the $850\mu\text{m}$ to 1.1mm flux ratio (blue histogram).

radio identifications are the correct counterparts for the SCUBA sources and that the astrometry in the AzTEC images is correct (Austermann et al. (2010) use a stacking analysis with 1.4GHz source positions to show that there is no systematic offset in the AzTEC astrometry in the LH field). The columns of Table 4.4 are as follows: the name given to the source in Coppin et al. (2006) (ID), its radio position (RA, Dec), the 1.1mm signal to noise ratio ($S/N_{1.1}$), the flux at 1.1mm ($S_{1.1}$), the 850 μ m deboosted SCUBA flux (S_{850}) as given in Coppin et al. (2006), the photometric redshift estimate provided by Dye et al. (2008) (z_{photo}), and the ratio of the SCUBA 850 μ m flux to the AzTEC 1100 μ m flux ($S_{1.1}/S_{850}$). Those sources that were found to have a signal to noise in the 1.1mm map of less than three have their flux ratios calculated using three sigma upper limits to produce a lower limit on the flux ratio.

From this table it is clear that there is significant levels of 1.1mm flux detected at the radio positions for many of the SCUBA galaxies. 11 of the 28 sources have a signal to noise ratio greater than three. This does imply a large number of SCUBA galaxies remain undetected in the 1.1mm image. If the unusual flux ratios were due to high redshifts then it is possible that the objects that are undetected at 1.1mm are at lower redshifts.

Figure 4.5 shows a histogram of the SCUBA 850 μ m to AzTEC 1.1mm flux for the sources listed in Table 4.4 (blue bars) and the ratio of SCUBA to MAMBO flux (hatched histogram) as shown in Eales et al. (2003) Figure 6. These two histograms appear to be similar although the SCUBA 850 μ m to AzTEC histogram has less extreme values. A two sided Kolmogorov-Smirnov (KS) test determined that the two samples have a probability of 99.6% of being drawn from the same distribution. This probability is supported by the visual similarity. The Eales et al. (2003) data cover a slightly larger range of flux ratios although this could just be due to their

larger sample. One interesting fact to note is that Eales et al. (2003) find 3 sources with $850\mu\text{m}$ to $1200\mu\text{m}$ ratios less than one whereas with the $850\mu\text{m}$ to $1100\mu\text{m}$ data I find no sources with a ratio of unity or lower. With 21 sources from Eales et al. (2003) and 11 sources described here these are relatively small samples.

4.5 Discussion

The primary aim of the analysis in this chapter was to investigate the use of $850\mu\text{m}/1200\mu\text{m}$ flux ratio to estimate redshifts. Eales et al. (2003) used the ratio of $850\mu\text{m}/1200\mu\text{m}$ flux to estimate the redshift of submillimetre galaxies. Their estimates placed those galaxies at high redshift, several with a redshift estimate of $\gtrsim 10.0$. If these estimates are correct these objects would be very interesting objects for further study.

Eales et al. (2003) relied on point source photometry of objects with SCUBA at $850\mu\text{m}$ detected in the MAMBO $1200\mu\text{m}$ image. Their low ratios of submillimetre to millimetre flux could be explained for instance, by a pointing drift during the photometry observations. Through careful analysis of their pointing observations they concluded that the low flux ratios they detected were astronomical cause rather than being due to instrument related problems. My analysis of the flux ratios in the LH field allows me to test the possibility that the flux ratios found by Eales et al. (2003) were actually due to combining the MAMBO maps with the $850\mu\text{m}$ photometry.

It is clear that I did not detect a large number (17) of SCUBA $850\mu\text{m}$ objects in the AzTEC image of the LH field. However, those SCUBA galaxies that are detected have relatively low $850\mu\text{m}/1100\mu\text{m}$ flux ratios. Seven of the 11 detected have a

flux ratio between one and two. The ratios I determined and the ratios Eales et al. (2003) found are visually similar and a KS-test supports this viewpoint. This supports Eales et al. (2003) in their conclusion that the low flux ratios are real phenomena. However, if you look at the photometric redshifts that Dye et al. (2008) found for these galaxies it is clear that they are at relatively moderate redshifts. The median redshift of the 3σ detections is $2.53^{+0.41}_{-0.45}$ and the maximum redshift is $4.21^{+0.24}_{-1.80}$. The fact that the $850\mu\text{m}$ to $1100\mu\text{m}$ ratios do not extend below unity suggests that the objects Eales et al. (2003) found with such low ratios are extreme objects, and so, possibly rare objects or potentially objects with inaccurate flux measurements.

In the first part of this chapter I investigated the 11 sources in the Abell 2125 field that Eales et al. (2003) found low $850\mu\text{m}/1100\mu\text{m}$ flux ratios for. Having determined their IRAC magnitudes I concluded that the flux ratios were not likely to be due to high redshift. The conclusion I came to in the second part of this chapter also suggests that these objects are at a redshift that is lower than would be expected if the low $850\mu\text{m}/1100\mu\text{m}$ flux ratios were due to redshift effects. It does, however, reproduce, in Lockman Hole (LH) field, the low ratios Eales et al. (2003) found in the Abell 2125 field.

Chapter 5

CUDSS Source Identifications

5.1 Introduction

Submillimetre galaxies represent an important element in theories of galaxy formation. Fully investigating these objects requires accurate positions in order for the targeting of follow up observations. However, one of the problems submillimetre observations pose is the large beam size associated with instruments in this waveband. For instance, SCUBA at $850\mu\text{m}$ had a beam size of 15 arcseconds. This limits the accuracy of source positions measured from submillimetre maps. Deep radio imaging is regularly used to improve the accuracy of these positions. This is because the surface density of radio sources is generally low enough that a given radio source can be statistically shown to be an identification of a submillimetre object. This can clearly only be applied to those submillimetre sources which are also radio sources. This technique is useful due to the much higher resolution of interferometric radio observations, which are generally sub-arcsecond, when compared with submillimetre observations, which can have an error of several arcseconds.

The more accurate radio position can then be used to identify the optical galaxy that is producing the submillimetre emission. Not all submillimetre galaxies are detected at radio wavelengths and a related problem is that a submillimetre galaxy with radio emission could be at relatively high redshift ($z \gtrsim 3.0$). In this case the lack of a negative K-correction at radio wavelengths could render the galaxy too faint to detect, thereby limiting the use of this technique to relatively low redshift objects.

Submillimetre galaxies often have red optical-near-infrared colours. Therefore, it seems likely that if one does not have radio observations and is forced to try to identify submillimetre sources using optical or near-infrared images, one will get the most reliable results with near-infrared images. Clements et al. (2004) (here after C04), for instance, used near-infrared K-band data to identify nine of the 27 submillimetre sources in the CUDSS 3-hour field. At even longer wavelengths, Younger et al. (2007) used Spitzer $3.6\mu\text{m}$ data to identify counterparts for all seven AzTEC 1.1mm sources detected in the COSMOS field. In this chapter, I am going to try the approach of using Spitzer IRAC data to identify the counterparts to the 27 submillimetre sources detected in the CUDSS 3-hour field and I hope to compare these with the identifications C04 found.

5.2 Observations

5.2.1 SCUBA Observations

The CUDSS survey was carried out at $450\mu\text{m}$ and $850\mu\text{m}$ using the Submillimetre Common User Bolometer Array (SCUBA) (Holland et al., 1999) on the JCMT

on Mauna Kea in Hawaii. The survey and results derived from it are discussed in a series of papers: Eales et al. (1999); Lilly et al. (1999); Eales et al. (2000); Webb et al. (2003a,b,c); Clements et al. (2004). It imaged 3 fields centred on approximately $03^h 00^\circ$, $10^h 25^\circ$ and $14^h 52^\circ$. However this chapter focuses on the first field, the so-called 3 hour field. This field covers an area of 60 square arcminutes to a depth of between 0.77mJy and 1.4mJy at $850\mu\text{m}$. Within the 3 hour field a total of 27 sources were detected with a signal to noise ratio of 3.0 or higher (15 of those have a S/N of >3.5).

C04 used images at other wavelengths (1.4GHz radio, K & K' band infrared, U B V & I optical) in an attempt to identify counterparts to the submillimetre detections in the 3 hour field. They found that nine submillimetre sources had secure identifications in at least one of the bands.

5.2.2 Optical and Near-Infrared Observations

CFDF Data

For the photometric redshift calculations in §5.4.4 the optical photometry was provided by Mark Brodwin in a private communication. It was obtained as part of the Canada-France Deep Fields (CFDF) survey (McCracken et al., 2001). The aim of this investigation was to measure the angular correlation function $\omega(\theta)$. One of the fields observed coincides with the CUDSS 3 Hour field and so photometry of the potential counterparts was available. The V band data were obtained using the Canada-France-Hawaii Telescope (CFHT) University of Hawaii 8 Kilo-pixel (UH8K) detector, while the B, R,I and Z data were obtained using Canada-France-Hawaii 12 Kilo-pixel (CFH12K) detector, with U band observations taken at the

Kitt Peak 4 metre telescope. The survey reached a limiting magnitude of 25 in I_{AB} . More information on the optical photometry can be found in Brodwin et al. (2006).

CUDSS Data

As part of the CUDSS survey, near-IR observations in the K band were obtained using the CFHT's CFHT-IR detector. However information about the original photometric calibration had been lost, and therefore I used the magnitudes listed in C04 to determine the zero point for further photometric measurements. The K band magnitudes listed in C04 are Vega magnitudes. I converted to the AB magnitude system using the relation in Equation 5.1 (Blanton et al., 2005):

$$K_{AB} = K_{Vega} + 1.85 \quad (5.1)$$

5.2.3 Spitzer IRAC Observations

The IRAC observations used in this chapter were centred on a right ascension of $3^h 02^m 44.82^s$ and declination of $0^\circ 07' 52.3''$. There are a total of 90 individual pointings for the 3.6, 4.5 and $5.8\mu\text{m}$ bands and 180 images for the $8\mu\text{m}$ band. The $8\mu\text{m}$ observations had an integration time of 50s for each exposure while the other three bands had an integration time of 100 seconds per exposure. I mosaicked the observations for each of these bands into large images using the Spitzer program MOPEX (Makovoz & Khan, 2005). This process is similar to the process described in Chapter 4 for the production of the Abell 2125 IRAC images. The observations differed slightly as they were not HDR observations, so

the extra steps needed to reduce HDR data were not needed. After the mosaicking it was obvious that the $5.8\mu\text{m}$ field was badly affected by the *first frame effect* artefact leading to a strong gradient across the image rendering it unusable without further correction. The *repeat_delta_dark* program created by Sean Carey and available from the Spitzer contributed software web-page (<http://ssc.spitzer.caltech.edu/dataanalysis/tools/contributed/irac/>) largely corrected the problem. The $3.6\mu\text{m}$ image was effected by the *mux bleed* effect although this was largely mitigated using the IRAC artefact mitigation software package which was also developed by Sean Carey and available from the Spitzer contributed software web-page. Source extraction was carried out on the remaining images using the SExtractor program (Bertin & Arnouts, 1996). This detected 3389, 2375 sources above $3.0 \sigma_{rms}$ in the $3.6\mu\text{m}$ and $4.5\mu\text{m}$ fields respectively. The numbers of objects detected in the two longer wavelength bands was an order of magnitude lower and so these two catalogues were ignored in the subsequent identification analysis. The reduced images can be seen in figures 5.1, 5.2, 5.3 and 5.4. The IRAC detectors have two slightly different fields of view, with the 3.6 and $5.8\mu\text{m}$ detectors imaging the same region of sky and the 4.5 and $8\mu\text{m}$ detectors imaging a slightly different but overlapping area.

The combined catalogue used in §5.5 contained 1422 sources with a signal to noise of 3 or greater. These sources were detected in both the $3.6\mu\text{m}$ and $4.5\mu\text{m}$ images using the Astronomical Point source EXtractor for MOPEX (APEX) program that is part of the MOPEX data reduction package.

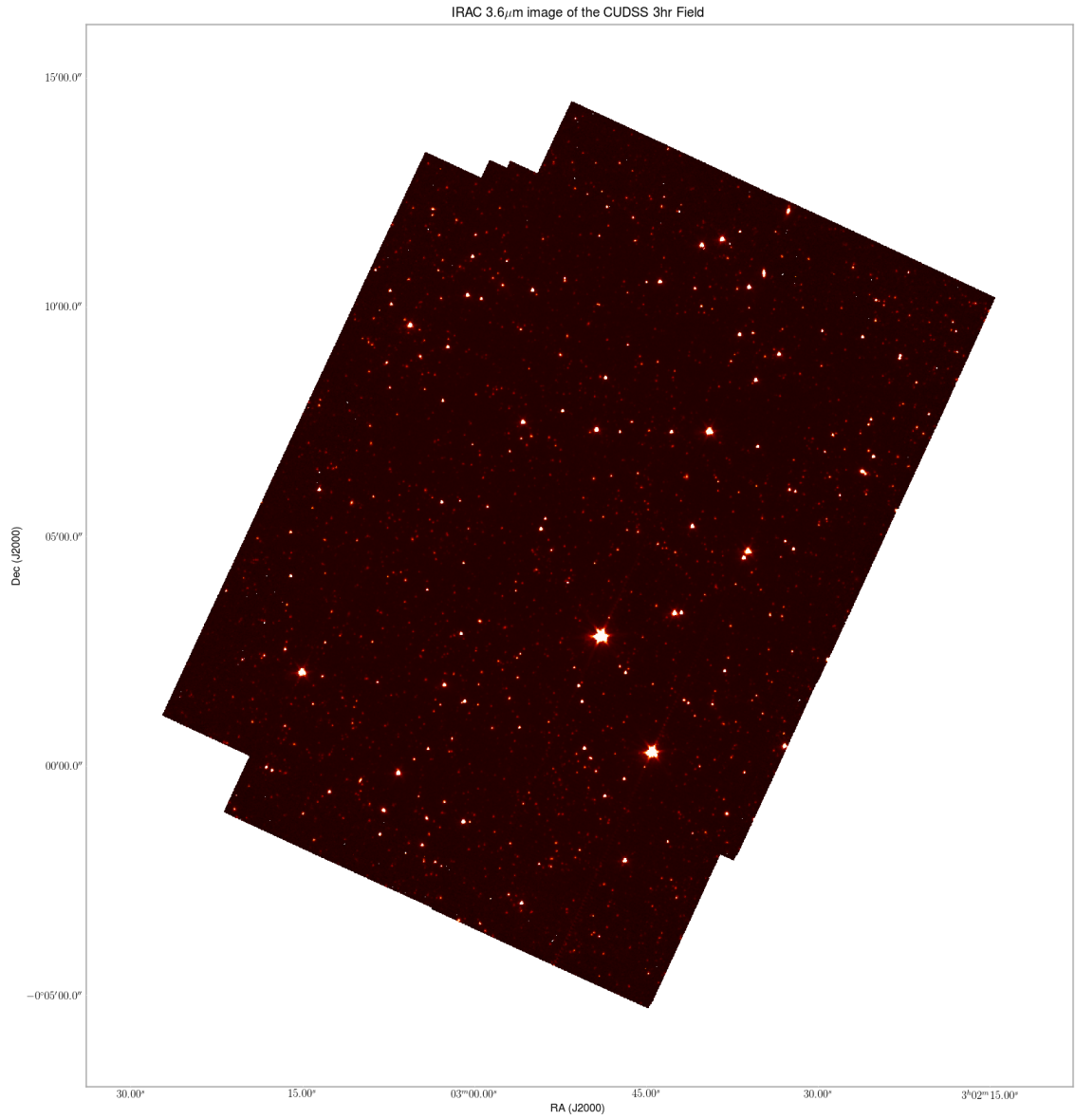


Figure 5.1: IRAC 3.6 μ m image of the CUDSS 3hr field.

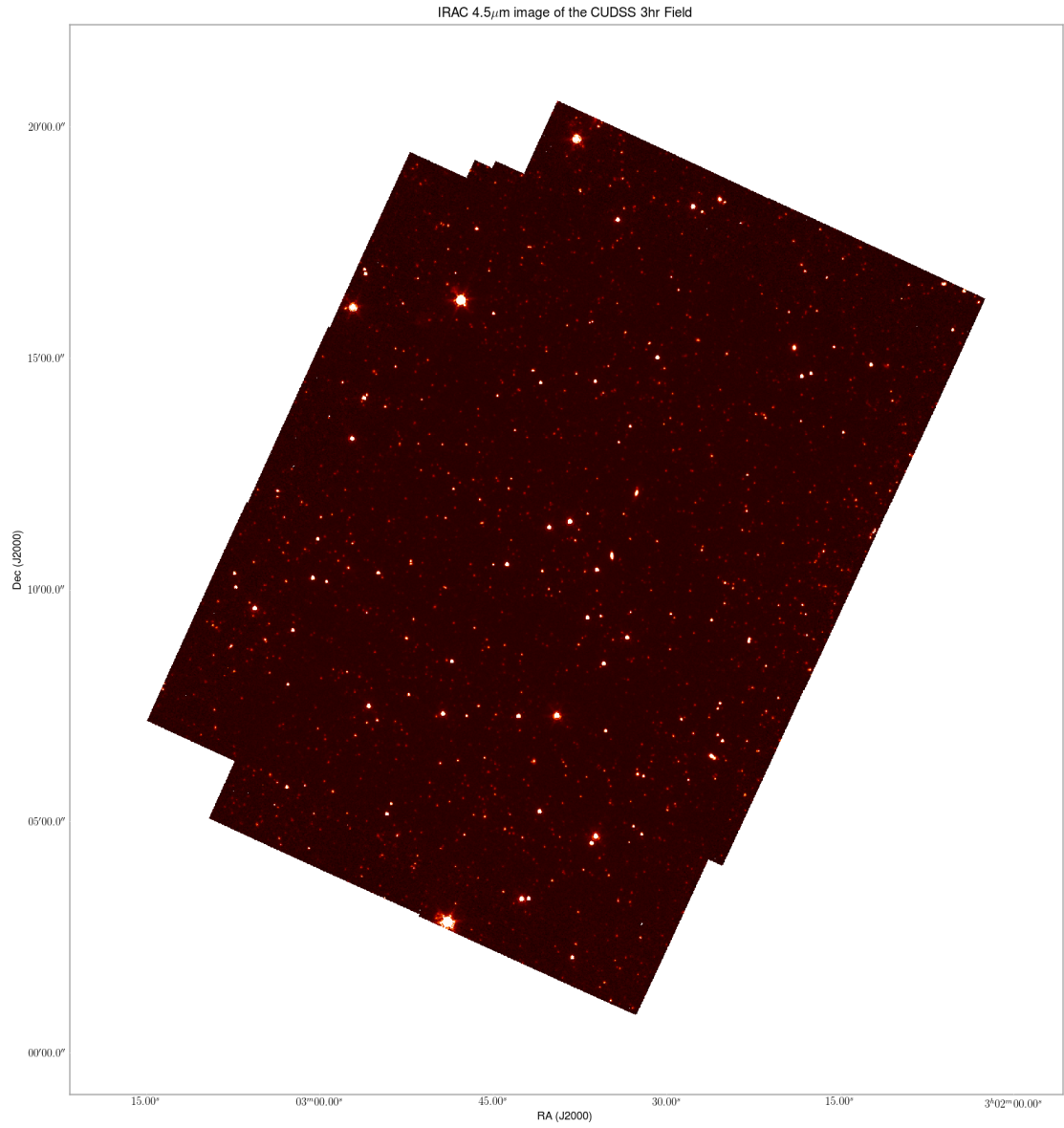


Figure 5.2: IRAC 4.5 μ m image of the CUDSS 3hr field.

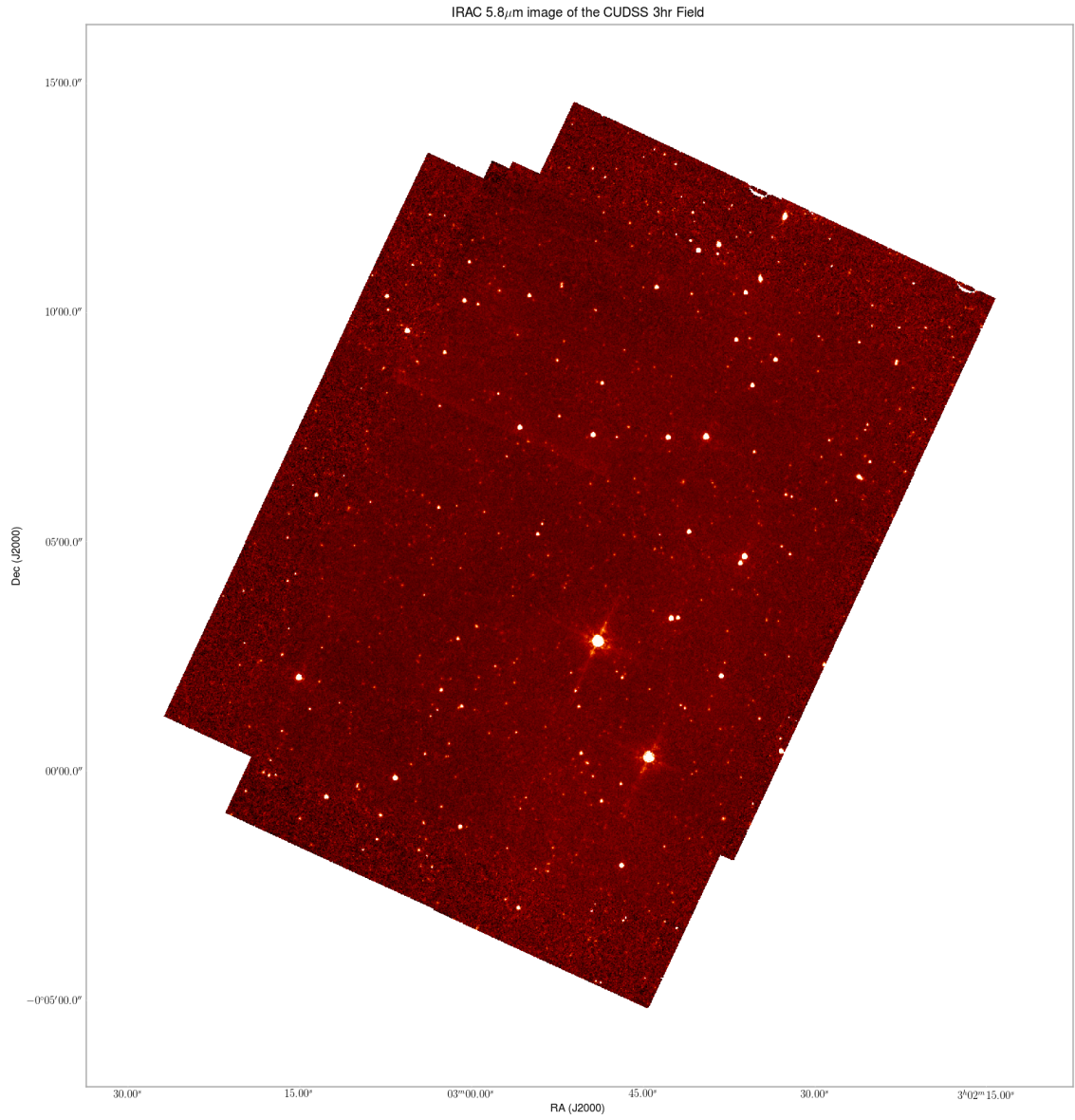


Figure 5.3: IRAC 5.8 μ m image of the CUDSS 3hr field.

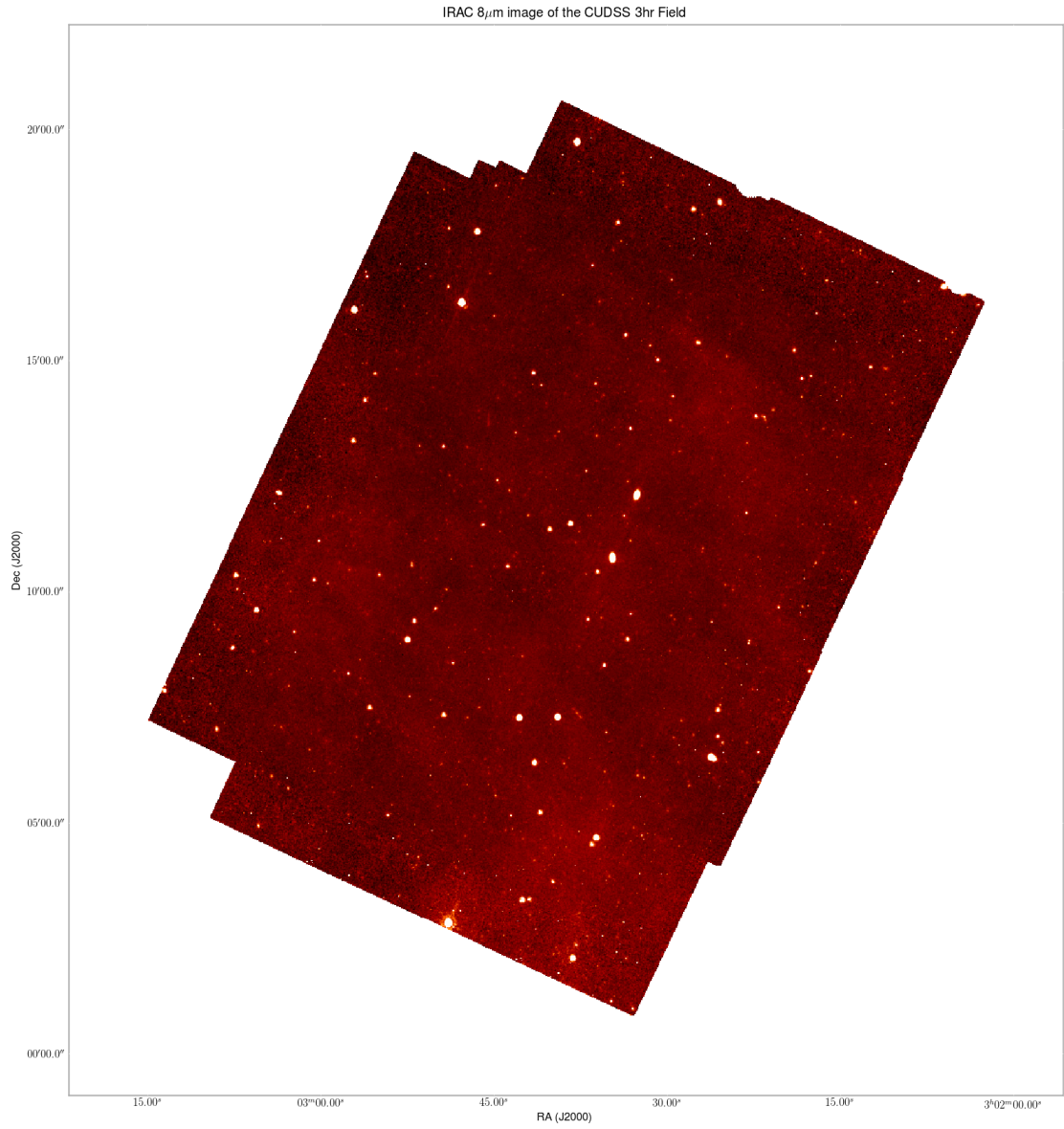


Figure 5.4: IRAC 8 μ m image of the CUDSS 3hr field.

5.3 Counterpart Identification

When attempting to securely identify objects detected with SCUBA (and other non-interferometric submillimetre/millimetre instruments) in other wavelength bands one of the most significant sources of uncertainty is the large beam associated with the instrument ($\sim 15''$). This, combined with a population of unresolved background sources, can move the peak of the emission well away from the real source location. There have been several studies of the effects of confusion and beam size on the positional accuracy of source detections (e.g. Hogg, 2001; Scott et al., 2002). Scott et al. (2002) find that the positions of the SCUBA detections could be off by as much as $4''$ in the fields they observed. One approach to finding the correct identifications for submillimetre sources in different bands is to use a frequentist technique to determine a statistical probability that a given coincidence between a submillimetre source and, for instance, an optical source occurs by chance. Lilly et al. (1999) used this approach to identify optical and radio counterparts for the first 12 sources detected in the CUDSS fields. Dye et al. (2009) used the same approach to find counterparts to BLAST sources. C04 also use this method to identify counterparts to the sources in the 3-hour field.

I used the same approach to find counterparts in the IRAC images to the SCUBA sources this method is as follows:

1. The minimum value S is found for each of the 27 sources in Webb et al. (2003a) in which S is defined as:

$$S = \pi d^2 n(> S_{3.6}) \quad (5.2)$$

d is the angular separation between the CUDSS detection and an IRAC source.

$n(> S_{3.6})$ (or $n(> S_{4.5}), n(> S_{5.8}), n(> S_8)$) is the surface number density of $3.6\mu\text{m}$ (or $4.5\mu\text{m}, 5.8\mu\text{m}, 8\mu\text{m}$) IRAC sources with a flux greater than that of the object under test. I only considered IRAC sources up to a maximum distance of 20 arcsec.

2. One million random positions were generated within the IRAC image and the minimum value of S was determined for each position.
3. The results of step number two produce a distribution of S values, $f(S)$, which was used to find the probability ($P(<S)$) that the IRAC source and SCUBA source are a random coincidence. If S_i is the minimum value of S for a given SCUBA source, the probability of the SCUBA and Spitzer sources being so close by chance is given by:

$$P(< S_i) = \frac{1}{N} \int_0^{S_i} f(S) dS. \quad (5.3)$$

in which N is the number of random positions.

I only considered counterparts as being secure if $P(< S_i) < 0.1$. Figures 5.5 and 5.6 show the CUDSS sources for which there is a Spitzer counterpart with $P(< S_i)$ less than 0.1.

To investigate how the colour of the IRAC sources impacts the identification of SCUBA objects I created a catalogue of objects common to both the $3.6\mu\text{m}$ and $4.5\mu\text{m}$ images. I then found the ratio of $3.6\mu\text{m}$ to $4.5\mu\text{m}$ flux for each of these objects and then further split the catalogue into smaller sub-catalogues. These sub-catalogues stretched from a flux ratio of zero to three in increments of 0.3. I then used the method described above to find the most likely counterparts in each sub-catalogue. The results of this analysis can be seen in section 5.5. The

advantage of this extra step is that submillimetre galaxies are often seen to be extremely red objects and so if there were two potential identifications of a SCUBA galaxy and one of them had a low flux ratio that object is more likely to be the secure identification of the SCUBA galaxy.

5.4 Results, All Channels

In this section the results of the Monte Carlo analysis on each of the individual bands are described. § 5.4.1 describes those sources that are detected in the IRAC images which have $P < 0.1$ and individually discusses each source. §5.4.2 compares the number of identifications I found with those C04 found and §5.4.3 mentions those SCUBA sources that do not have secure identifications in the C04 paper but are found to have secure identifications in this current analysis. §5.4.4 describes the photometric redshift analysis and the resulting photometric redshifts which I performed using the extra photometric data available to me. The images for each band can be seen in Figures 5.1, 5.2, 5.3, 5.4

One fact that is immediately clear is that the $3.6\mu\text{m}$ and $4.5\mu\text{m}$ IRAC channels have more identifications than the other two channels. The $5.8\mu\text{m}$ and $8\mu\text{m}$ bands have a less uniform background than the $3.6\mu\text{m}$ and $4.5\mu\text{m}$ bands which interfered with the source detection. The resulted in fewer objects in the two longer waveband catalogues.

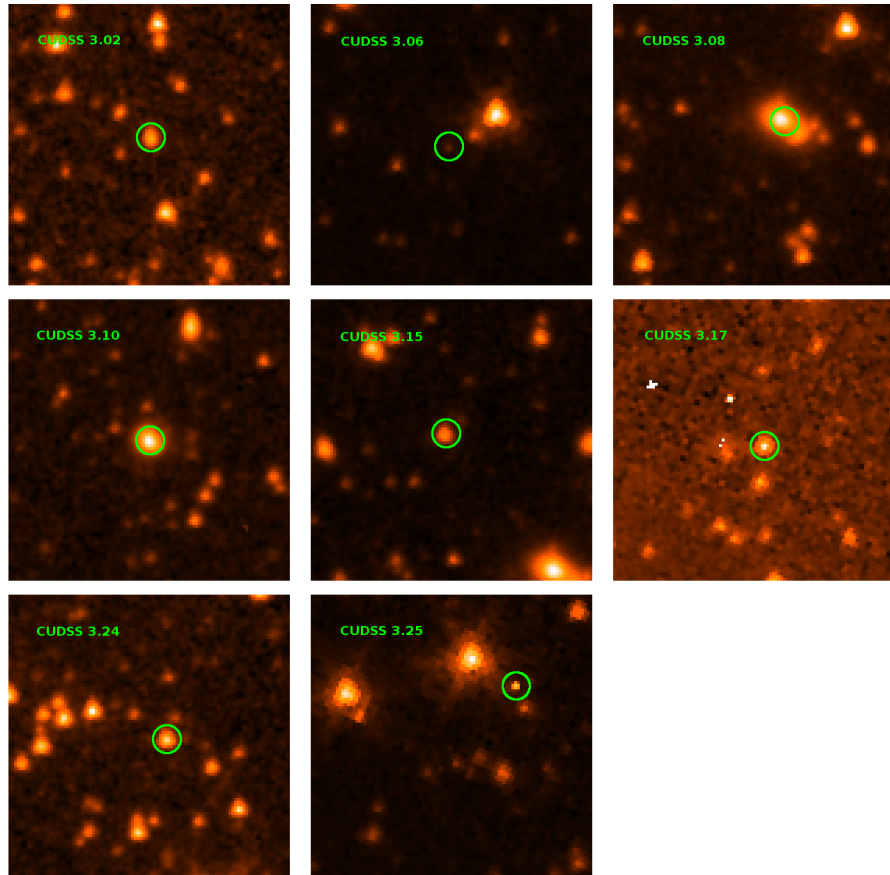


Figure 5.5: $60'' \times 60''$ Postage stamp images centred on the Webb et al. (2003a) SCUBA position, with the $P<0.1$ IRAC $3.6\mu\text{m}$ counterpart circled. The circles are approximately $5''$ in diameter.

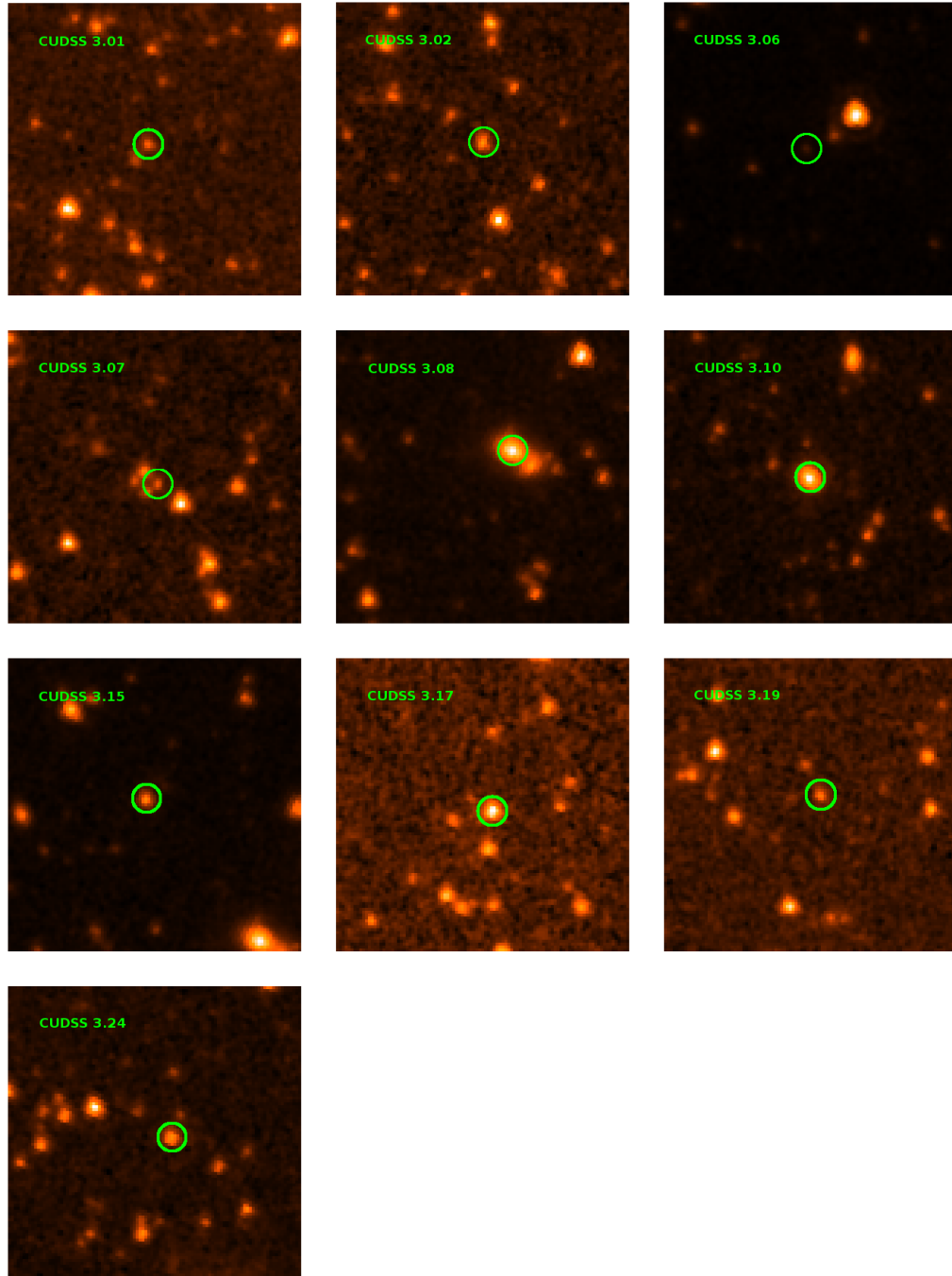


Figure 5.6: $60'' \times 60''$ Postage stamp images centred on the Webb et al. (2003a) SCUBA position, with the $P < 0.1$ IRAC $4.5\mu\text{m}$ counterpart circled.

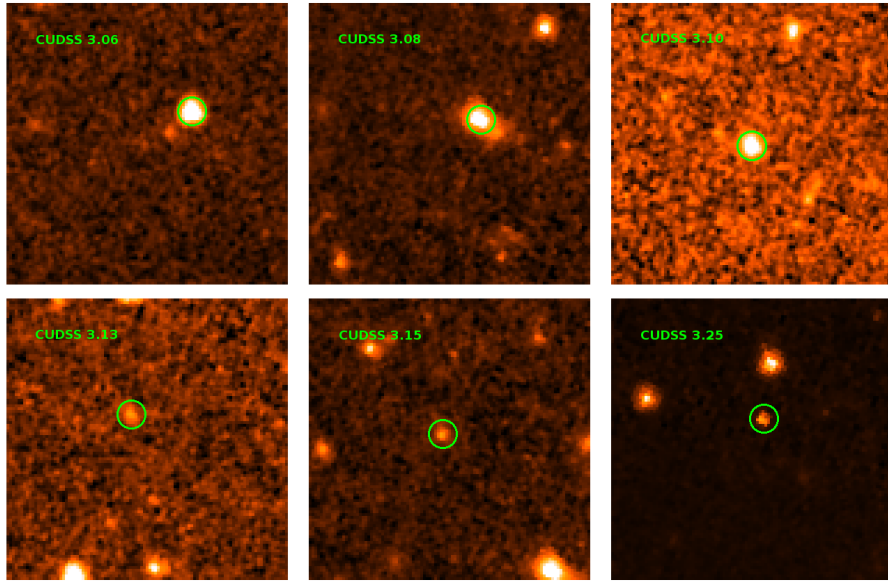


Figure 5.7: $60'' \times 60''$ Postage stamp images centred on the Webb et al. (2003a) SCUBA position, with the $P < 0.1$ IRAC $5.8\mu\text{m}$ counterpart circled.

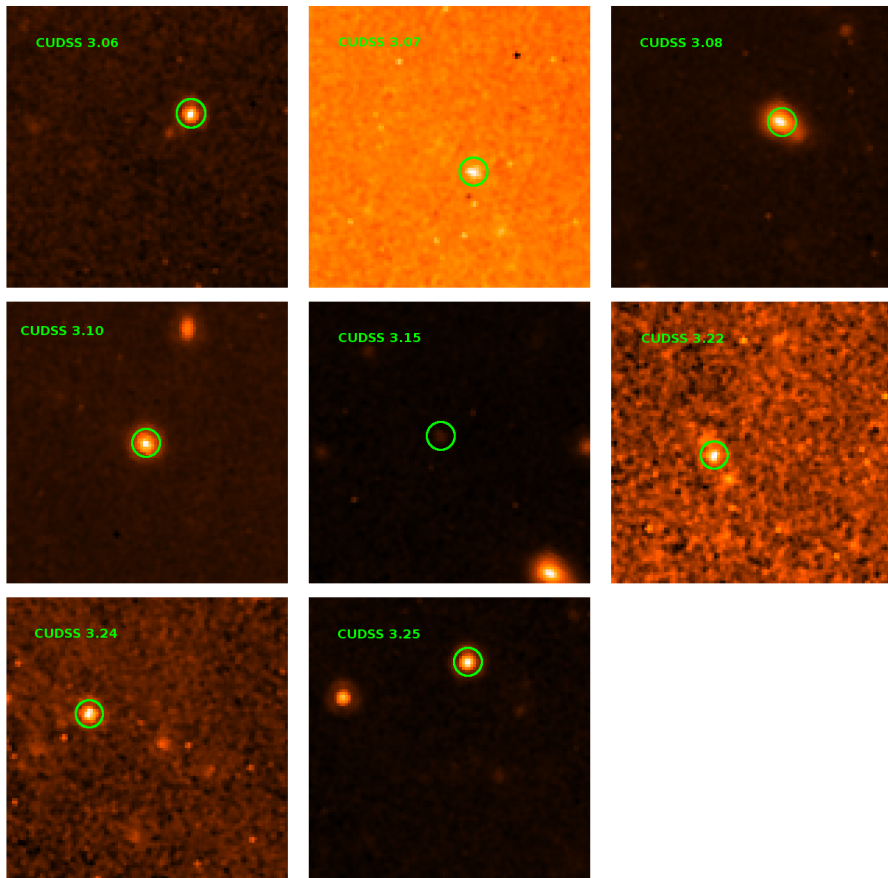


Figure 5.8: $60'' \times 60''$ Postage stamp images centred on the Webb et al. (2003a) SCUBA position, with the $P < 0.1$ IRAC $8\mu\text{m}$ counterpart circled.

Table 5.1: Counterparts to the Webb et al 2003 sources in the IRAC fields. Secure and suspect identifications are in bold. Sources in plain text are detections of the secure or suspect source in one of the other IRAC bands. Those entries with *Coi* indicate sources that for some reason I have deemed to be coincidental associations.

ID	Band	RA _{irac}	Dec _{irac}	Mag (AB)	P	Sep ($''$)	Status
3.01	3.6 μ m	03:02:44.66	+00:06:35.21	22.38 \pm 1.57	0.11	1.85	–
"	4.5 μ m	03:02:44.67	+00:06:35.36	21.81 \pm 1.21	0.073	2.00	Sec
3.02	3.6 μ m	03:02:42.81	+00:08:02.70	21.17 \pm 0.90	0.033	1.21	Sec
"	4.5 μ m	03:02:42.82	+00:08:02.69	21.40 \pm 1.00	0.026	1.22	Sec
3.06	3.6 μ m	03:02:36.15	+00:08:16.91	22.26 \pm 1.49	0.043	0.99	Sec
"	4.5 μ m	03:02:36.16	+00:08:16.91	22.01 \pm 1.32	0.031	1.07	Sec
3.06	5.8 μ m	03:02:35.47	+00:08:23.87	17.59 \pm 0.17	0.035	11.43	Coi
"	8 μ m	03:02:35.48	+00:08:24.01	18.36 \pm 0.25	0.037	11.41	Coi
3.07	3.6 μ m	03:02:35.81	+00:06:08.75	22.20 \pm 1.45	0.151	2.42	–
"	4.5 μ m	03:02:35.74	+00:06:09.40	22.06 \pm 1.36	0.061	1.61	Sec
"	8 μ m	03:02:35.44	+00:06:05.49	20.27 \pm 0.60	0.064	7.19	Coi
3.08	3.6 μ m	03:02:26.11	+00:06:23.56	17.56 \pm 0.17	0.046	7.97	Sec
"	4.5 μ m	03:02:26.17	+00:06:24.14	17.81 \pm 0.19	0.034	7.71	Sec
"	5.8 μ m	03:02:26.13	+00:06:23.87	18.11 \pm 0.22	0.032	7.95	Sec
"	8 μ m	03:02:26.15	+00:06:24.00	16.66 \pm 0.11	0.0070	7.81	Sec
3.10	3.6 μ m	03:02:52.51	+00:08:56.85	19.02 \pm 0.33	0.0090	0.66	Sec
"	4.5 μ m	03:02:52.51	+00:08:56.91	19.22 \pm 0.37	0.0028	0.61	Sec
"	5.8 μ m	03:02:52.51	+00:08:56.79	19.44 \pm 0.41	0.0020	0.73	Sec
"	8 μ m	03:02:52.52	+00:08:56.95	17.30 \pm 0.15	0.0003	0.64	Sec
3.13	3.6 μ m	03:02:36.07	+00:09:58.34	19.78 \pm 0.48	0.133	6.30	–
"	4.5 μ m	03:02:36.07	+00:09:58.42	20.26 \pm 0.59	0.12	6.35	–
"	5.8 μ m	03:02:36.06	+00:09:58.27	20.54 \pm 0.68	0.087	6.14	Sec

Table 5.1: Continued

ID	Band	RA _{irac}	Dec _{irac}	Mag (AB)	P	Sep (^{''})	Status
3.15	3.6μm	03:02:27.72	+00:06:53.54	19.85 \pm 0.49	0.027	2.09	Sec
"	4.5 μ m	03:02:27.74	+00:06:53.48	19.71 \pm 0.46	0.014	2.27	Sec
"	5.8 μ m	03:02:27.73	+00:06:53.44	20.11 \pm 0.55	0.013	2.15	Sec
"	8 μ m	03:02:27.76	+00:06:53.63	20.13 \pm 0.56	0.013	2.60	Sec
3.17	3.6μm	03:02:31.52	+00:10:28.69	20.47 \pm 0.65	0.063	2.64	Sec
"	4.5 μ m	03:02:31.53	+00:10:28.80	20.95 \pm 0.81	0.057	2.50	Sec
3.19	3.6 μ m	03:02:43.85	+00:09:53.65	22.47 \pm 1.64	0.151	2.25	—
"	4.5 μ m	03:02:43.84	+00:09:53.72	22.00 \pm 1.32	0.10	2.34	Sec
3.22	3.6 μ m	03:02:38.75	+00:06:11.29	19.75 \pm 0.47	0.23	9.74	Coi
"	4.5 μ m	03:02:38.75	+00:06:11.37	20.18 \pm 0.57	0.20	9.70	Coi
"	5.8 μ m	03:02:38.96	+00:06:16.25	20.34 \pm 0.62	0.12	8.99	Coi
"	8 μ m	03:02:38.97	+00:06:16.44	20.09 \pm 0.55	0.078	9.06	Sec
3.24	3.6μm	03:02:56.58	+00:08:06.89	20.52 \pm 0.67	0.095	3.45	Sec
"	4.5 μ m	03:02:56.59	+00:08:06.95	20.62 \pm 0.70	0.067	3.35	Sec
"	8 μ m	03:02:57.65	+00:08:13.08	19.04 \pm 0.34	0.070	13.75	Coi
3.25	3.6 μ m	03:02:38.39	+00:11:27.83	15.34 \pm 0.06	0.033	16.30	Coi
"	4.5 μ m	03:02:38.40	+00:11:27.88	15.92 \pm 0.08	0.03	16.32	Coi
"	5.8 μ m	03:02:38.51	+00:11:15.89	17.78 \pm 0.19	0.010	4.44	Coi
"	8 μ m	03:02:38.40	+00:11:27.94	17.26 \pm 0.15	0.032	16.36	Coi

5.4.1 Secure IRAC detections

I describe an IRAC counterpart as a secure identification of a SCUBA $850\mu\text{m}$ source if the probability of it being a chance association is less than 0.1 in at least one of the four IRAC wavebands. I decided any galaxy with a separation from the submillimetre position of >10 arcseconds was likely to be a chance coincidence. Of the 27 sources detected by SCUBA, 12 secure identifications are seen in total. Ten of these have a P value below the cut-off in the $4.5\mu\text{m}$ band, seven in the $3.6\mu\text{m}$ band, four in the $5.8\mu\text{m}$ band and four in the $8\mu\text{m}$ band. This would appear at first glance to be a similar identification rate when compared to the number of identifications C04 reported.

Table 5.1 shows those sources that I found found in the IRAC images that have the lowest P values. The table lists the name Webb et al. (2003a) give the source (*ID*), the IRAC band the data corresponds to (*Band*), the co-ordinates of the counterpart in the IRAC data (Ra_{IRAC}, Dec_{IRAC}), its AB magnitude (*Mag*), the probability it is a chance coincidence (*P*), its distance from the SCUBA position (*Sep*) and whether it is believed to be an identification or not (*Status*). *Sec* indicates a robust identification and *Coi* indicates a source that is believed to be a chance coincidence rather than an identification. A row with a dash in this column indicates data for a secure or suspect ID in another IRAC band.

CUDSS 3.01

A source is detected in the $3.6\mu\text{m}$ and $4.5\mu\text{m}$ images near the position of this SCUBA source. At $3.6\mu\text{m}$ the source has a P value of 0.11 which is just above the cut-off of 0.1. The P value for the source at $4.5\mu\text{m}$ is 0.073. The low P value for

the source at $4.5\mu\text{m}$ leads me to believe that this is a secure identification. C04 did not find a secure identification and did not detect the Spitzer source in their K-band data.

CUDSS 3.02

This counterpart is detected in both the $3.6\mu\text{m}$ and $4.5\mu\text{m}$ fields with P values below the cut-off. I conclude that this is a secure identification. This is the same object detailed by C04 and they also concluded that it was a secure identification.

CUDSS 3.06

There is an object one arc-second from the SCUBA position with $P < 0.1$ in both the $3.6\mu\text{m}$ and $4.5\mu\text{m}$ bands. C04 also detect this object and they describe it as a secure identification. For these reasons I conclude that this is a secure IRAC identification of the SCUBA source.

CUDSS 3.07

A source is detected in the $4.5\mu\text{m}$ image with a P of 0.061. This source is also seen in the $3.6\mu\text{m}$ image but it has a P value above the cut-off. This would lead me to conclude that this is a secure identification. This object is part of a group of four sources that can also be seen in C04's K-band image. They, however, find that a different member of this *trapezium*, as they have dubbed it, is the securely identified counterpart to the SCUBA source. The K-band object they describe as a securely identified counterpart has a P value of 0.19, which is above their cut-off.

The reason they conclude it is a secure identification is due to radio emission that is coincident with the K-band object. In their postage stamp images there is a suggestion of radio emission at the position of my identification also, although it does not appear as significant. The IRAC identification and the C04 object are at similar distances from the SCUBA galaxy. The stronger radio emission at the position of the K-band object might suggest that that detection is more likely to be the true counterpart to the SCUBA source.

CUDSS 3.08

This source has a detection in all 4 IRAC bands with a P value below the cut-off and the detections in the four bands appear to coincide with each other. The source appears to be extended although this is possibly due to 2 sources sources being blended together. This adds some uncertainty as to whether or not it is a secure identification as does the relatively large offset between the ID and the SCUBA position. Given though that it has a low P in all 4 bands I conclude that it is a secure identification. This same object is also detected by C04 in their radio and K-band data and they describe it as a secure identification.

CUDSS 3.10

This CUDSS source has a counterpart detected in all 4 IRAC bands with an angular separation of less than $1''$ between these positions and the SCUBA source. This SCUBA source is clearly securely identified it in the IRAC bands. C04 detect an object in their K-band and radio data at the same position as the IRAC object and they also conclude it is a secure identification of the SCUBA galaxy.

CUDSS 3.13

This source is detected with a P value less than 0.1 in the $5.8\mu\text{m}$ IRAC image. It is also detected in the $3.6\mu\text{m}$ and $4.5\mu\text{m}$ images although the probability of being a chance coincidence is found to be above the cut-off in these two wavebands. However, as it is detected in three bands with a value for P below cut-off in one of them, I conclude that this is a secure identification even though it is at a relatively large offset of six arcseconds. C04 did not find a secure identification although in their I-band they detected a source coincident with the IRAC object with a P value of 0.11, which is just above their cut-off.

CUDSS 3.15

This object is detected in all 4 bands with a P value below the cut-off. It is also relatively close to the SCUBA position. These two facts suggest that this is a secure identification of the submillimetre object. C04 found an object in both their radio and K-band data at this position which they also described as a secure identification.

CUDSS 3.17

I detected this counterpart with a low P value in the $3.6\mu\text{m}$ and $4.5\mu\text{m}$ images but not in the $5.8\mu\text{m}$ and $8\mu\text{m}$ images although there is some emission in these bands visible at the position of the $3.6\mu\text{m}$ and $4.5\mu\text{m}$ source. The $3.6\mu\text{m}$ detection may coincide with an artefact in the image, possibly caused by a cosmic ray strike, as its centre pixels are very luminous and there are other apparent artefacts nearby. Supporting the assertion that this object is a secure identification is the fact that

while it is possible the $3.6\mu\text{m}$ detection is an artefact it has a similar magnitude to the $4.5\mu\text{m}$ detection and is only two and a half arcseconds from the Webb et al. (2003a) position.

C04 found a radio source which they describe as a secure identification of this object. The radio position is not coincident with the IRAC position and is at a similar distance from the submillimetre position. They also detected a K-band object which is coincident with the Spitzer data. As both my identification and C04's identification are at similar distance from the submillimetre object it is difficult to decide which one has more merit.

CUDSS 3.19

This object is detected with a P on the threshold in the $4.5\mu\text{m}$ image and so should be described as a non-identification. However, as it is also detected in $3.6\mu\text{m}$ with a P value only slightly above the cut-off I conclude that this object is securely identified. C04 do not detect a counterpart for this SCUBA galaxy.

CUDSS 3.22

This source has a low P detection at $8\mu\text{m}$. This counterpart was detected by Gilbank et al. (2003). They report it as being a disk galaxy with a total K magnitude of 19.52 ± 0.16 and a red I-K colour of 4.16 ± 0.12 . This source is $\sim 9''$ from the SCUBA source. It is also detected in the $5.8\mu\text{m}$ image. The $3.6\mu\text{m}$ and $4.5\mu\text{m}$ data suggest a different object as a possible identification although with a P value above the cutoff in both. This counterpart was detected by Hammer et al. (1995) as part of their redshift survey and has an I band magnitude (AB) of 20.49 and a

V-I colour of 1.94 with a redshift of 0.618.

As it is within 10 arcseconds and has a P value below the cut-off I conclude that the $8\mu\text{m}$ identification is a secure identification. C04 did not identify a counterpart for this object.

CUDSS 3.24

A possible counterpart with $P < 0.1$ has been identified in both the $3.6\mu\text{m}$ and $4.5\mu\text{m}$ postage stamp images for this submillimetre source at a distance of approximately three and a half arcseconds from the submillimetre position. C04 also found a secure identification in their radio and K-band data at this position.

CUDSS 3.25

This submillimetre source has potential identifications in all four IRAC channels. However the $4.5\mu\text{m}$ and $8\mu\text{m}$ detections are some distance from the submillimetre object and are apparently a foreground object. The SDSS have observed this object (SDSS J030238.38+001127.7) and classified it a star.

The $5.8\mu\text{m}$ detection is considerably closer to the SCUBA position but it appears on inspection to be an artefact. This is supported by the fact that it is not seen in the other IRAC bands. The $3.5\mu\text{m}$ detection is close to the 4.5 and $8\mu\text{m}$ detections. However it also appears to be an artefact in the image. This hypothesis is supported by the fact that the object does not appear in the other bands.

In this case although all four bands have objects with low probabilities of chance associations none of the detections can be classed as a secure or suspect identifi-

cation. This conclusion is supported by the fact that none of the objects coincide with the secure identification C04 suggested from both their radio and K-band data. I do not detect the C04 counterpart.

5.4.2 Comparison with C04

In their analysis of the SCUBA sources, C04 concluded that they had securely identified nine. Using the IRAC data I have securely identified 12 SCUBA sources. Of these 12 secure identifications, eight are for SCUBA sources C04 have previously securely identified. In all but two of these, CUDSS 3.07 and CUDSS 3.17, the counterparts from C04 and this chapter are the same, that is I agree with the C04 classification. CUDSS 3.07 is the unusual *trapezium* of sources which C04 suggest may be associated with each other. If this is true, it is not surprising that there is some confusion relating to the identification. C04 have two possibilities for a secure identification for CUDSS 3.17. They chose the radio object presumably because it is slightly closer to the submillimetre galaxy and has a lower P value. Their K band object, which is coincident with the IRAC identification, is also below their probability cut-off however. They note that the radio object is not visible in their K and I-band images which is probably why it is not seen in the IRAC data.

C04 also found four identifications that they described as suspect. I did not find secure identifications for these SCUBA galaxies in the IRAC images. This would reinforce the suspect designation C04 gave their identifications.

5.4.3 IDs from the IRAC data only

Of the 27 SCUBA sources detected in the CUDSS 3 hour field, C04 find secure or suspect identifications for 13. Of the remaining 14 SCUBA sources not securely identified by C04, three have a secure identification in the IRAC images. C04 detected counterparts for CUDSS 3.13 but their analysis lead them to believe that their detection was not an identification of the SCUBA galaxy. CUDSS 19 and CUDSS 3.22 were not detected by C04 at all.

5.4.4 Photometric Redshift Analysis

Without spectroscopic observations an effective way to estimate redshifts of objects is to attempt to fit a SED to the available data points. In this instance I used the HyperZ package to estimate redshifts to the identifications determined from the analysis above. In order to estimate the redshifts optical data was obtained from the CFDF survey (McCracken et al., 2001). This added U, B, V, R, I and Z bands to the IRAC data for the secure and suspect identifications and where possible, the K band data from C04. The data available allowed for a maximum of 11 photometric bands to be included in the redshift fit although not all objects were detected in each band. The photometry for each IRAC identification can be seen in Table 5.2. The table lists the name of the SCUBA source (*ID*), the separation between the Spitzer location and the optical source (*Sep*) and then the AB magnitudes for each band.

Several objects are not seen in multiple bands, and the lower the number of bands the less reliable the photometric fit. Another concern is that the optical data for some of the objects is a significant distance from the Spitzer position. For this

Table 5.2: Multiband Photometry (AB Magnitudes) for the Redshift Analysis.

ID	Sep	3.6 μ m	4.5 μ m	5.8 μ m	8 μ m	U	B	V	R	I	Z	K
3.01	0.8	22.38 \pm 1.57	21.81 \pm 1.21	—	21.22 \pm 0.93	—	—	—	26.64 \pm 0.93	27.68 \pm 2.36	27.57 \pm 4.62	—
3.02	0.4	21.17 \pm 0.90	21.40 \pm 1.00	—	—	—	—	—	21.98 \pm 0.05	21.63 \pm 0.05	21.46 \pm 0.05	20.49 \pm 0.02
3.06	1.7	22.26 \pm 1.49	22.01 \pm 1.32	—	—	—	—	—	—	—	26.5 \pm 1.73	23.33 \pm 0.21
3.07	0.9	22.20 \pm 1.45	22.06 \pm 1.36	—	—	—	—	—	26.41 \pm 0.75	27.11 \pm 1.39	—	—
3.08	0.3	17.56 \pm 0.17	17.81 \pm 0.19	18.11 \pm 0.22	16.66 \pm 0.11	20.24 \pm 0.05	19.34 \pm 0.05	18.45 \pm 0.05	17.92 \pm 0.05	17.59 \pm 0.05	17.3 \pm 0.05	16.41 \pm 0.01
3.10	0.5	19.02 \pm 0.33	19.22 \pm 0.37	19.44 \pm 0.41	17.30 \pm 0.15	21.38 \pm 0.05	20.81 \pm 0.05	20.12 \pm 0.05	19.82 \pm 0.05	19.41 \pm 0.05	19.24 \pm 0.05	18.16 \pm 0.01
3.13	1.1	19.78 \pm 0.48	20.26 \pm 0.59	20.54 \pm 0.68	21.36 \pm 1.00	25.73 \pm 0.37	25.37 \pm 0.19	23.70 \pm 0.06	22.34 \pm 0.05	20.84 \pm 0.05	20.75 \pm 0.05	—
3.15	0.4	19.85 \pm 0.49	19.71 \pm 0.46	20.11 \pm 0.55	20.13 \pm 0.56	24.38 \pm 0.10	23.82 \pm 0.05	23.41 \pm 0.05	22.72 \pm 0.05	22.10 \pm 0.05	21.62 \pm 0.05	20.18 \pm 0.02
3.17	0.6	20.47 \pm 0.65	20.95 \pm 0.81	20.37 \pm 0.61	21.54 \pm 1.08	24.68 \pm 0.14	24.42 \pm 0.08	23.85 \pm 0.07	23.23 \pm 0.05	22.05 \pm 0.05	21.80 \pm 0.05	21.00 \pm 0.19
3.19	1.3	22.47 \pm 1.64	22.00 \pm 1.32	—	—	—	—	—	—	27.30 \pm 1.65	—	—
3.22	0.3	19.75 \pm 0.47	20.18 \pm 0.57	20.44 \pm 0.65	20.08 \pm 0.51	24.47 \pm 0.11	23.55 \pm 0.05	22.45 \pm 0.05	21.20 \pm 0.05	20.31 \pm 0.05	20.18 \pm 0.05	19.90 \pm 0.10
3.24	0.2	20.52 \pm 0.67	20.62 \pm 0.70	—	20.71 \pm 0.73	25.74 \pm 0.37	25.19 \pm 0.16	25.03 \pm 0.22	24.42 \pm 0.12	23.48 \pm 0.05	23.03 \pm 0.07	21.11 \pm 0.07

reason I decided to ignore redshifts for source for which the optical position was greater than 1.2 arcseconds, or two IRAC pixel widths, from the IRAC position.

The results of the redshift estimation can be seen in Table 5.3. The columns are: *ID*, the CUDSS name for the source, and z_{phot} , the photometric redshift estimate with the errors. It is immediately apparent from the results that setting an upper limit on the separation between the optical and the mid-infrared positions was a reasonable step as the two objects, CUDSS 3.06 and CUDSS 3.19, that are above this limit have very large errors associated with their redshift estimate suggesting HyperZ could not find a reliable fit to the data.

The maximum redshift of those sources identified with IRAC is $2.89^{+5.28}_{-0.00}$ (although this object, CUDSS 3.07, is only detected at 3.6 μ m and 4.5 μ m and in R and I). The minimum is $0.10^{+0.02}_{-0.10}$ although this object, CUDSS 3.01, is only seen in six of the 11 possible bands. The median redshift is 0.53 which is relatively low for submillimetre objects. However C04 also estimated photometric redshifts for some of their objects in the three hour field and found a median of 0.73. This is higher than the median my analysis found but still relatively low when compared with other estimates of the median redshift of submillimetre objects (for example, Chapman et al. (2005)). The results suggest that identifying submillimetre objects using infrared data preferentially identifies those submillimetre galaxies that are relatively nearby rather than the higher redshift galaxies other surveys have found.

5.5 Results, 3.6 μ m and 4.5 μ m Combined

In this section the results of the Monte Carlo analysis on the combined 3.6 μ m and 4.5 μ m catalogue is described. §5.5.1 describes those sources that are detected in

Table 5.3: Photometric Redshifts for the IRAC Identifications.

ID	z_{phot}
3.01	$0.10^{+0.02}_{-0.10}$
3.02	$0.490^{+0.001}_{-0.003}$
3.06	$2.12^{+4.54}_{-2.12}$
3.07	$2.89^{+2.39}_{-2.89}$
3.08	$0.19^{+0.002}_{-0.002}$
3.10	$0.120^{+0.073}_{-0.079}$
3.13	$0.510^{+0.009}_{-0.003}$
3.15	$1.120^{+0.004}_{-0.003}$
3.17	$0.880^{+0.001}_{-0.060}$
3.19	$0.41^{+2.99}_{-0.28}$
3.22	$0.530^{+0.002}_{-0.002}$
3.24	$1.11^{+0.01}_{-0.02}$

the combined catalogue which have $P < 0.1$ and individually discusses each source. §5.5.2 compares the number of identifications I found with those C04 found and §5.5.3 mentions those SCUBA sources that do not have secure identifications in the C04 paper but are found to have secure identifications in this current analysis.

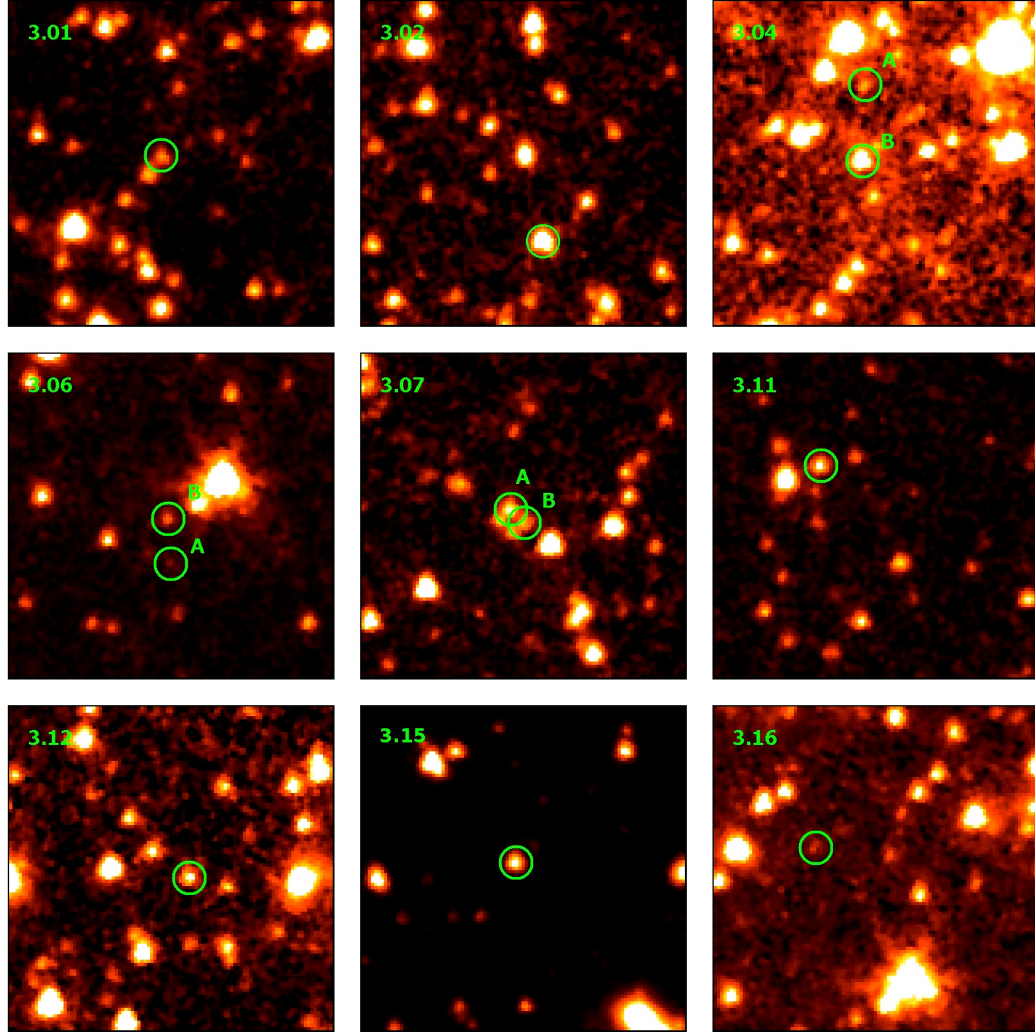


Figure 5.9: $60'' \times 60''$ Postage stamp images centred on the Webb et al. (2003a) SCUBA position, with the $P < 0.1$ IRAC $3.6\mu\text{m}$ counterpart circled. The circles are approximately $5''$ in diameter.

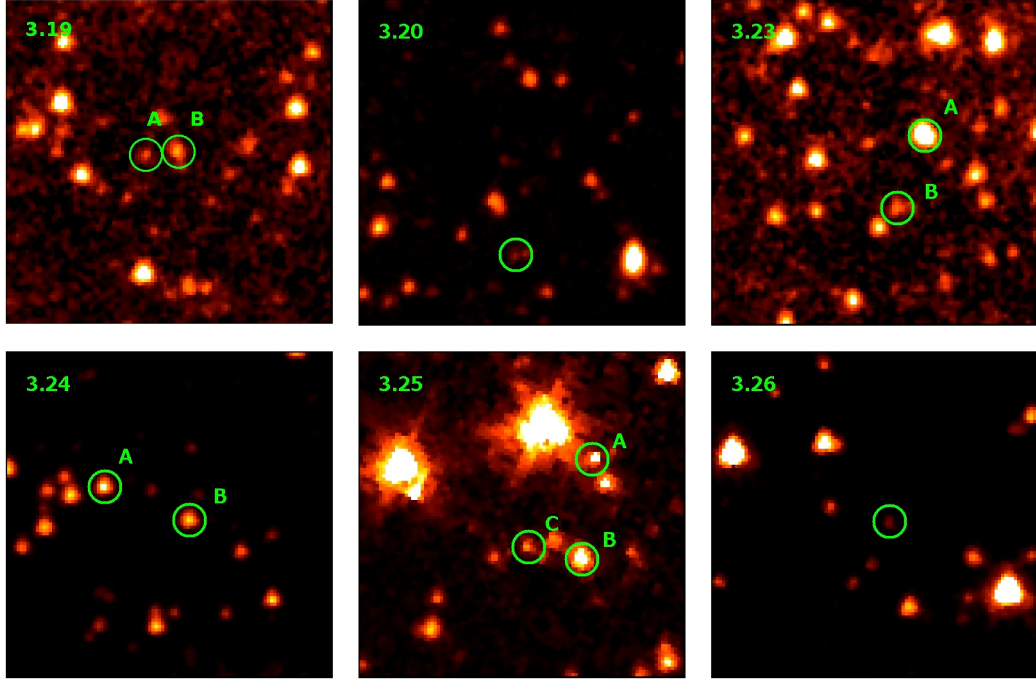


Figure 5.9: Continued

5.5.1 Secure IRAC detections

I describe an IRAC $3.6\mu\text{m}4.5\mu\text{m}$ counterpart as a secure identification of a SCUBA $850\mu\text{m}$ source if the probability of it being a chance association is less than 0.1 and only if it has a $3.6\mu\text{m}$ to $4.5\mu\text{m}$ flux ratio less than one. If it has a ratio of one or greater but a P value below the cut-off I describe it as a suspect identification. As in the earlier section I decided any galaxy with a separation from the submillimetre position of >10 arcseconds was likely to be a chance coincidence as I deemed the 20 arcsecond limit I used in the actual Monte Carlo analysis overly large. Of the 27 sources detected by SCUBA, nine secure identifications are seen in total along with three suspect identifications. This again would appear at first glance to be a similar identification rate when compared to the number of identifications C04 reported and similar to the number of identifications I found using each individual IRAC band.

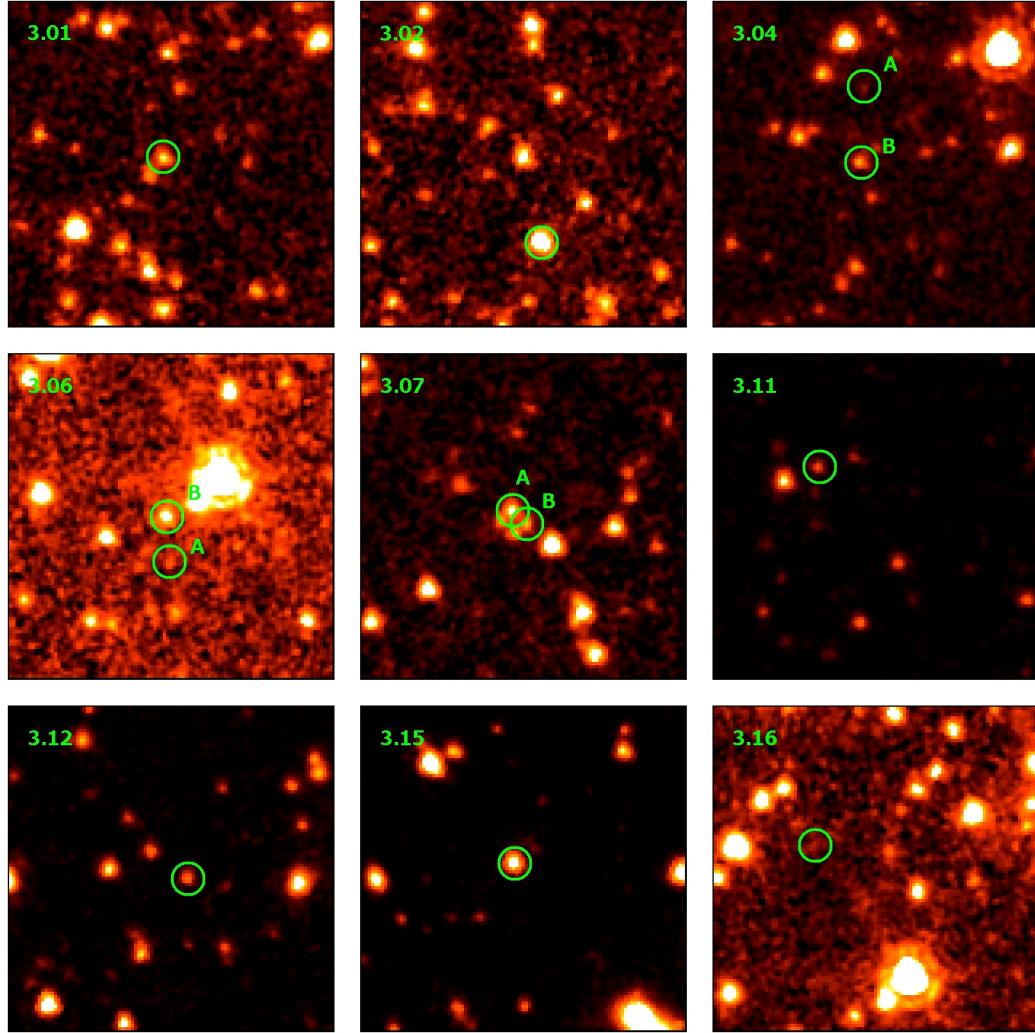


Figure 5.10: $60'' \times 60''$ Postage stamp images centred on the Webb et al. (2003a) SCUBA position, with the $P < 0.1$ IRAC $4.5\mu\text{m}$ counterpart circled.

Table 5.4: Counterparts to the Webb et al 2003 sources in the IRAC fields. Secure identifications are in bold while sources in italics are suspect identifications. Sources in plain text are detections with a low P value but are deemed coincidences.

ID	RA _{3.6μm}	Dec _{3.6μm}	Mag _{3.6μm} (AB)	Mag _{4.5μm} (AB)	P	Ratio $S_{3.6}/S_{4.5}$	Sep (")	Status
3.01	03:02:44.68	+00:06:35.68	22.13 \pm 0.08	21.31 \pm 0.17	0.001	0.47 \pm 0.02	2.23	Sec
3.02	03:02:42.59	+00:07:46.65	20.08 \pm 0.02	19.92 \pm 0.03	0.049	0.86 \pm 0.01	15.18	Coi
3.04a	03:02:44.57	+00:07:09.28	22.89 \pm 0.20	23.69 \pm 0.28	0.013	2.10 \pm 0.52	14.51	Coi
<i>3.04b</i>	<i>03:02:44.60</i>	<i>+00:06:55.00</i>	<i>21.01 \pm 0.03</i>	<i>21.25 \pm 0.05</i>	<i>0.021</i>	<i>1.25 \pm 0.38</i>	<i>2.93</i>	<i>Sus</i>
3.06a	03:02:36.12	+00:08:08.47	23.07 \pm 0.23	23.62 \pm 0.31	0.099	1.66 \pm 0.37	9.03	Coi
3.06b	03:02:36.15	+00:08:16.84	21.84 \pm 0.08	21.49 \pm 0.11	0.006	0.72 \pm 0.03	1.05	Sec
3.07a	03:02:35.91	+00:06:12.00	21.16 \pm 0.05	20.88 \pm 0.07	0.016	0.77 \pm 0.02	2.64	Sec
3.07b	03:02:35.74	+00:06:09.50	21.41 \pm 0.06	21.55 \pm 0.08	0.018	1.14 \pm 0.05	1.52	Coi
3.11	03:02:53.60	+00:11:30.98	20.75 \pm 0.04	21.22 \pm 0.05	0.077	1.55 \pm 0.05	13.78	Coi
3.12	03:02:38.49	+00:10:24.09	21.36 \pm 0.08	21.07 \pm 0.08	0.034	0.76 \pm 0.03	3.73	Sec
3.14	03:02:25.81	+00:09:04.19	23.63 \pm 0.51	22.24 \pm 0.64	0.005	0.28 \pm 0.06	3.34	Sec
3.15	03:02:27.73	+00:06:53.36	19.26 \pm 0.01	19.16 \pm 0.02	0.002	0.91 \pm 0.01	2.15	Sec
3.16	03:02:36.66	+00:08:48.89	22.53 \pm 0.19	23.46 \pm 0.21	0.009	2.35 \pm 0.50	12.01	Coi
3.19a	03:02:44.24	+00:09:52.96	22.78 \pm 0.31	23.21 \pm 0.27	0.089	1.48 \pm 0.30	4.47	Coi
3.19b	03:02:43.83	+00:09:53.59	22.01 \pm 0.10	21.49 \pm 0.15	0.026	0.62 \pm 0.03	2.38	Sec
3.20	03:02:53.39	+00:09:22.24	22.77 \pm 0.16	22.10 \pm 0.31	0.076	0.54 \pm 0.05	17.81	Coi
3.23a	03:02:53.41	+00:06:19.99	20.02 \pm 0.02	20.38 \pm 0.03	0.041	1.39 \pm 0.05	9.91	Coi
3.23b	03:02:53.75	+00:06:06.41	22.72 \pm 0.17	22.05 \pm 0.30	0.037	0.54 \pm 0.03	9.82	Sec
3.24a	03:02:57.64	+00:08:13.05	19.77 \pm 0.02	19.25 \pm 0.03	0.016	0.62 \pm 0.01	13.63	Coi
<i>3.24b</i>	<i>03:02:56.58</i>	<i>+00:08:06.77</i>	<i>20.00 \pm 0.02</i>	<i>20.05 \pm 0.03</i>	<i>0.014</i>	<i>1.04 \pm 0.02</i>	<i>3.48</i>	<i>Sus</i>
3.25a	03:02:37.80	+00:11:21.75	20.78 \pm 0.11	21.37 \pm 0.05	0.097	1.72 \pm 0.10	16.08	Coi
3.25b	03:02:37.93	+00:11:03.02	19.12 \pm 0.03	19.24 \pm 0.01	0.024	1.12 \pm 0.02	14.02	Coi
3.25c	03:02:38.59	+00:11:05.36	20.99 \pm 0.09	20.68 \pm 0.05	0.060	0.75 \pm 0.03	6.70	Sec
<i>3.26</i>	<i>03:02:34.93</i>	<i>+00:09:10.70</i>	<i>21.12 \pm 0.06</i>	<i>21.09 \pm 0.07</i>	<i>0.045</i>	<i>0.97 \pm 0.04</i>	<i>3.11</i>	<i>Sus</i>

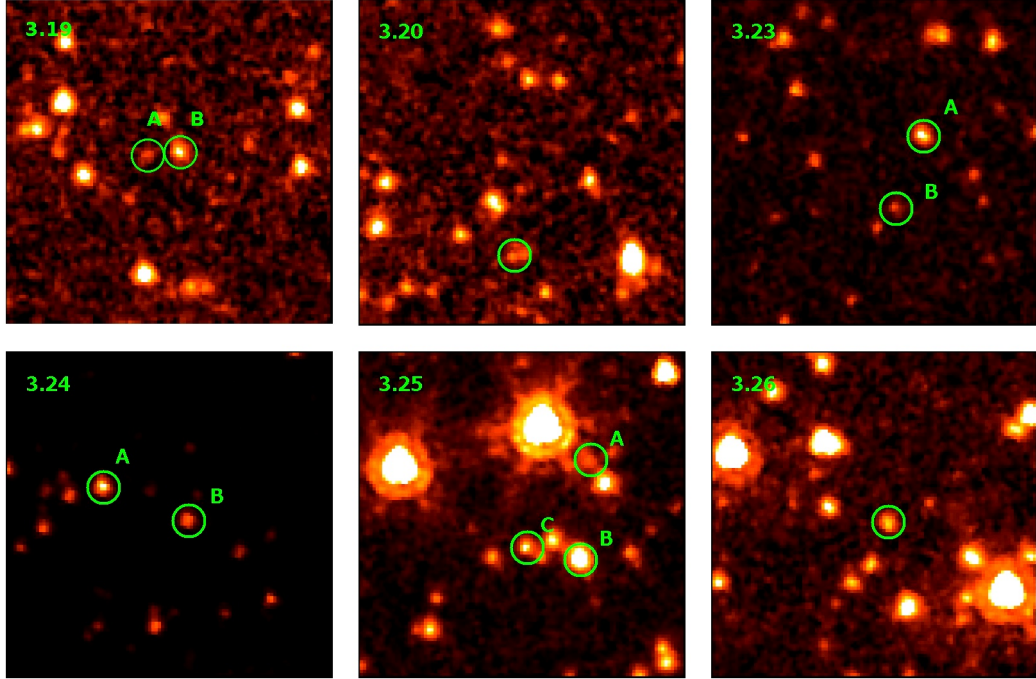


Figure 5.10: Continued

Table 5.1 shows those sources that I found found in the IRAC images that have the lowest P values. The table lists the name Webb et al. (2003a) give the source (ID), the co-ordinates of the counterpart in the IRAC data (Ra_{IRAC}, Dec_{IRAC}), its AB magnitude in the 3.6 and 4.5 μ m bands ($Mag_{3.6\mu m}$ and $Mag_{4.5\mu m}$), the probability it is a chance coincidence (P), the ratio of 3.6 μ m to 4.5 μ m flux ($Ratio$), its distance from the SCUBA position (Sep) and whether it is believed to be an identification or not ($Status$). *Sec* indicates a robust identification, *Sus* indicates an identification that is not robust and *Coi* indicates a source that is believed to be a chance coincidence rather than an identification.

CUDSS 3.01

A source is detected in the 3.6 μ m and 4.5 μ m images near the position of this SCUBA source. It has a P value of 0.001 and the low flux ratio suggests the object

is red. These two facts leads me to declare this object a secure identification of the SCUBA source. This object is also detected at 5.8 μ m and 8 μ m. C04 did not find a secure identification and did not detect the Spitzer source in their K-band data. This object is also identified in §5.4.

CUDSS 3.02

This counterpart is detected in both the 3.6 μ m and 4.5 μ m images and has a P value below the cut-off. I conclude that this is not a secure identification as it is 15.18 arcseconds from the SCUBA source. C04 identified an object much closer to the submillimetre position.

Using the individual catalogues I identified a counterpart for this object which is much closer to the SCUBA galaxy.

CUDSS 3.04

There are two objects with a P below the cut-off. However one source is 14.51 arcseconds from the SCUBA position. The flux ratio for this objects suggests that it is not very red. The second object (3.04b) is much closer to the submillimetre source and has a lower P value. It is also detected in the two longer IRAC bands. The flux ratio for this source also suggests that it might be blue in colour. Due to this I conclude this is a suspect identification. In the initial analysis I do not determine an identification for this source.

C04 find a suspect identification at the same position as my suspect identification.

CUDSS 3.06

There are two potential identifications for this SCUBA source with a P value below 0.1. However the second potential identification is closer to the SCUBA source, has a lower P value and its flux ratio suggests that it is the redder of the two. Because of this I conclude this object 3.06b is a secure identification of the submillimetre source. Unlike 3.06a this object is also detected at $5.8\mu\text{m}$. This object is also identified in § 5.4.

This IRAC object coincides with a Radio and K band source that C04 describe as a secure identification.

CUDSS 3.07

Two sources are detected with low P values for this submillimetre object. They are both part of a group of four sources that can also be seen in C04's K-band image. The object with the lowest P value also has the lower flux ratio implying it is the redder of the two. It is however slightly further from the SCUBA source. This issue aside the remaining evidence suggests that 3.07a is a secure identification. This is a different member of the quartet of sources than the object I securely identified using the individual catalogues.

3.07a coincides with the radio and K band object that C04 determined was a secure identification of the submillimetre object. C04 suggest that this set of 4 sources or 'trapezium' as they have dubbed it might be a cluster of high redshift objects.

CUDSS 3.12

This object has a P value below the cut-off and has a flux ratio below one indicating it is red although it is probably not an extremely red object. I also detected this object at 5.8 μ m and 8 μ m. I therefore conclude that this object is a secure identification of the SCUBA source. C04 did not find a secure identification for this SCUBA source. I also did not securely identify this galaxy using the individual catalogues.

CUDSS 3.14

I detected this object in the 3.6 μ m, 4.5 μ m and 8 μ m bands. The P value is 0.005 suggesting a reliable identification and it is also very red with a flux ratio of 0.28. These factors lead me to conclude that it is a secure identification of the submillimetre object. C04 found an object that had a P value above their cut-off (although they described it as a suspect identification) that does not coincide with my identification. I also did not securely identify this galaxy using the individual catalogues.

CUDSS 3.15

This object is detected in all 4 bands and has a P value below the cut-off. It is also relatively close to the SCUBA position. These two facts suggest that this is a secure identification of the submillimetre object even though it does not have a low flux ratio. C04 found an object in both their radio and K-band data at this position which they also described as a secure identification. This object is also identified in § 5.4.

CUDSS 3.19

There are two objects detected in the IRAC images that have a P value below the cut-off. 3.19a is further from the SCUBA source and has a flux ratio greater than unity, while 3.19b is closer to the submillimetre object and has a flux ratio of 0.62. Because of this I conclude that the second object is the securely identified counterpart. I also detected 3.19b at 8 μ m. C04 did not record a magnitude for this object. This object is also identified in § 5.4.

CUDSS 3.23

I detected two objects for this submillimetre galaxy and found that they had a P value below the cut-off. They are both some distance from the SCUBA source, just inside the 10 arcsecond limit. 3.23a has a large flux ratio suggesting that this object is unlikely to be the IRAC counterpart to the submillimetre galaxy. The second source does, however, have a flux ratio of 0.54 thus I conclude that this object is the true counterpart of the submillimetre galaxy. It is, however, not seen in the two longer IRAC bands. This object is also identified in § 5.4.

C04 detected an object in their K band image which is not coincident with my identification. The P value they found was 2.0 and so they did not consider it an identification.

CUDSS 3.24

Two possible counterparts for this submillimetre galaxy are seen with a P value below the cut-off. One of these 3.24a is above the 10 arcsecond cut-off. The

other source, 3.24b, has a lower P value but a flux ratio of unity. It is only 3.5 arcseconds from the SCUBA source. Because this object has a relatively high flux ratio I conclude that it is a suspect identification of the submillimetre galaxy. I concluded in § 5.4 that this object was a secure identification.

C04 also found a secure identification in their radio and K-band data at this position.

CUDSS 3.25

There are 3 potential identifications of this source in the IRAC data. Two are outside the 10 arcsecond cut-off. The final source, 3.25c, is within 7 arcseconds of the SCUBA galaxy. It has a P value of 0.06 and a flux ratio of 0.75. This leads me to conclude that this object, 3.25c, is a secure counterpart for the submillimetre galaxy.

This conclusion is reinforced by C04 who found an object in both their radio and K-band data at that position that they concluded was a secure identification. I did not find a secure identification for this object using the individual catalogues.

CUDSS 3.26

I find a source with a P value below the cut-off at approximately 3.11 arcseconds from the SCUBA position. This object, however, has a flux ratio of approximately unity. Due to this I conclude that it is a suspect identification. It does coincide with a detection C04 recorded. They concluded it was not an identification due to its high P value.

5.5.2 Comparison with C04

In their analysis of the SCUBA sources, C04 concluded that they had securely identified nine. Using the IRAC data I have also securely identified nine SCUBA sources. Of these nine secure identifications, four are for SCUBA sources C04 have previously securely identified. These four identifications coincide with the C04 identifications. Two more of the submillimetre sources C04 found secure counterparts for have P values below the cut-off in my analysis. CUDSS 3.02 is clearly not identified in my analysis as it is 15.18 arcseconds from the SCUBA source, while the C04 identification is 1.1 arcseconds away from the submillimetre galaxy. However, the second object, CUDSS 3.24, is an object I described as a suspect identification due to its flux ratio. It does however coincide with the C04 secure ID.

This leaves 3 submillimetre galaxies that C04 identified in their data that I have not detected a possible counterpart for, whether secure or suspect, CUDSS 3.8, CUDSS 10 and CUDSS 17. CUDSS 3.17 is a radio only identification so it is perhaps not surprising that I do not find an ID for it.

C04 also found four identifications that they described as suspect, CUDSS 3.4, CUDSS 3.5, CUDSS 3.14, CUDSS 3.27. I did not find counterparts for CUDSS 3.27 nor did I identify CUDSS 3.5. I concluded that the source I detected for CUDSS 3.04 is suspect. This compares favourable with the C04 result, they determined that there was a suspect K-band identification at the same position. C04 found a suspect ID for CUDSS 3.14 whereas I concluded that the source I found was in fact a secure identification of the SCUBA galaxy.

5.5.3 IDs from the IRAC data only

Of the 27 SCUBA sources detected in the CUDSS 3 hour field, C04 find secure or suspect identifications for 13. Of the remaining 14 SCUBA sources not securely identified by C04, four have a secure identification from the combined catalogues. C04 detected counterparts for CUDSS 3.01 and CUDSS 3.23 but the P values they determined were above their cut-off. Their detections are not coincident with the identifications I found. C04 did not record detections for CUDSS 3.12 and CUDSS 3.19

5.6 Discussion

5.6.1 Individual Catalogues

In this chapter I set out to determine counterparts for submillimetre sources discovered in the Canada-UK Deep Submillimetre Survey using SCUBA. Of the 27 SCUBA sources in this field, my analysis discovered secure identifications for 12. These identifications are considered secure due to a P value of 0.1 or less in at least one of the IRAC wavebands.

C04 determine optical and radio identifications to the SCUBA sources. In some cases the identifications in this study differ from those suggested by C04, but a large proportion of them are the same one found by C04. Six of the nine secure identifications in C04 are within $1''$ of an IRAC identification. This clearly reinforces the secure identifications. This agreement between two different studies using catalogues of sources from different bands suggests that the Monte Carlo

method for identifying submillimetre galaxies using IRAC imaging is a sound and reliable method.

I have found new identifications for three SCUBA objects that C04 did not identify including two for which C04 did not detect a possible counterpart. Four sources C04 suggested as suspect identifications were not detected in the IRAC images. However on the whole the agreement between the identification C04 found and my identifications would suggest that using the IRAC bands to identify submillimetre galaxies is viable.

A photometric redshift analysis indicates that these objects are largely at relatively low redshifts. Previous studies of submillimetre objects have determined that the median redshift for their sources is ~ 2.4 (Chapman et al., 2005; Aretxaga et al., 2007) while the objects in this study have a median of 0.53. The low photometric redshifts are supported by the similar analysis of C04. The median photometric redshift they found is 0.73 and they quote spectroscopic redshifts for several objects which agree with my estimates from HyperZ.

5.6.2 Combined Catalogue

I also completed a second ID analysis using the $3.6\mu\text{m}$ to $4.5\mu\text{m}$ flux ratio as an extra element. This analysis also securely identified 9 objects using a P value cut-off of 0.1 and a flux ratio cut-off of less than one suggesting that they are red objects, three further SCUBA galaxies have suspect identifications. Four of these objects, CUDSS 3.01, 3.06, 3.15 and 3.19 are the same objects identified in the initial analysis. A further identification from the original analysis, CUDSS 3.24, is considered a suspect identification in the second approach as it has a flux ratio

greater than one.

Four of the nine identifications C04 described as secure are coincident with an object securely identified in the combined catalogue. I have found new identifications for four SCUBA objects that C04 did not identify including two for which C04 did not detect a possible counterpart. Four sources C04 suggested as suspect identifications were not identified using the combined catalogue and three of these were not detected in the combined catalogue.

Chapter 6

Conclusion

6.1 Introduction

In this thesis I set out to add to the knowledge surrounding the formation and evolution of luminous submillimetre galaxies seen at high redshift over the past decade. I have used a number of different techniques to investigate these unusual occupants of the early universe. In chapter 2, after describing the reduction of 1.1mm AzTEC maps, I detail a direct extraction of luminous objects in 1.1mm observations that I used to produce a catalogue of those objects with significant emission. In chapter 3 I described a stacking analysis of objects in 1.1mm observations that I then used to quantify the contribution that fainter sources might make to the image. Part of this analysis also determined the total contribution these galaxies make to the Cosmic Infrared Background in this waveband and the average dust content of these galaxies. I then, in chapter 4, described an investigation of the results of Eales et al. (2003) that seemed to imply the existence of some very high redshift submillimetre galaxies was undertaken using these 1.1mm images and

IRAC images of the Abell 2125 field. And finally a I performed a Monte Carlo analysis to determine secure identifications for bright submillimetre galaxies found in the Canada UK Deep Submillimetre Survey 3 hour field. This analysis enabled me to determine redshifts to these objects using photometric redshift estimation techniques.

The results of these different analysis are summarised below.

6.2 AzTEC Observations and Analysis

One of my initial tasks as a PhD student was to take part in the 1.1 millimetre AzTEC observations of the Lockman Hole and Subaru XMM-Newton Deep Field fields. These observations occurred during the winter of 2005/2006. In parallel with the instrument team at the University of Massachusetts Amherst, I reduced this data to produce two scientifically useful images.

The aim of this reduction was to produce an independent check of the maps to confirm the results. The two reductions produced maps with similar areas and noise levels. A source extraction carried out on the maps produced for this work largely agreed with the catalogue produced by the instrument team.

The catalogue I compiled contained more detections than the catalogue AU10 published. This larger number of detections can be largely explained by the extra steps AU10 took to ensure that their catalogue contained real sources. The fluxes of the sources seen in both catalogues are slightly lower in the AU10 catalogue than mine. This is probably due to slight differences in the input observations.

These conclusions suggest that the results of my reduction largely agree with those

published in Austermann et al. (2010). It was decided that further analysis of the objects contained within these fields should be carried out using the maps as published in AU10 as these were the SHADES consortium deemed these the official maps.

The reason these two fields had been observed was that they had previously been observed by the SCUBA instrument and had been shown to contain submillimetre galaxies. While I had compiled a catalogue of the sources visible in the image with significant emission, it was decided to attempt to access how much of a contribution fainter sources were making, if any, to the background.

6.3 Stacking Analysis

I performed a stacking analysis using catalogues of infrared sources extracted from Spitzer IRAC observations of the LH field. This showed that these objects made, on average, a non-negligible contribution to the so-called CIB at 1.1mm. The primary purpose of this work was to determine through use of a stacking technique if there was positive 1.1mm flux at the positions of sources with known Spitzer MIPS and IRAC flux.

Prominent peaks were visible at the centre of each stacked postage stamp for each of the catalogues and a clear peak was seen in at least one of the individual bins when the data was stacked according to redshift. This clearly shows that though these sources may not be individually detectable in the AzTEC image there is still some non-negligible 1.1mm flux associated with them.

When stacked according to redshift bins, the data shows that the amount of mil-

limetre flux is seen to increase out to high redshift. This implies that there is a significant amount of hidden star formation occurring in galaxies at relatively high redshifts ($3.0 < z < 4.5$) and it highlights the need for a greater focus on the fainter portion of the high redshift submillimetre galaxy population.

The contribution to the CIB that I found due to these Spitzer galaxies is seen to largely agree with other studies. Although when compared with AzTEC COSMOS data it does suggest that there is a large contribution to the CIB from infrared galaxies not detected at 1.1mm. An interesting future comparison will be the contribution these sources make to Herschel observations. The contribution to the 1.1mm background from Spitzer sources does appear to peak at relatively low redshifts.

The estimated dust masses that I determined from the average stacked fluxes are seen to increase with redshift up to the third redshift bin for each Spitzer band. This is in agreement with studies that have shown an increase in the number of massive dusty galaxies a greater redshift. It also suggests that there is a peak in the dust-mass function with galaxies at redshifts past the redshift third bin having on average less dust.

6.4 Eales et al. 2003; High z or Cold Dust

Eales et al. (2003) produced results from their analysis of the ratio of $1200\mu\text{m}$ flux to $850\mu\text{m}$ flux that if true would suggest that at least some submillimetre galaxies are at very high redshifts. If true this would open the possibility that luminous dusty submillimetre galaxies were in place very early in the history of the universe. I investigated this result using the AzTEC observations of the Lockman Hole and

Spitzer IRAC observations of an area around the Abell 2125 cluster.

6.4.1 Lockman Hole 1.1mm Observations

The 1.1mm data from the AzTEC observations opened up the possibility of testing the millimetre to submillimetre fluxes in a different field as the 1.2mm MAMBO sources were primarily found in the Abell-2125 and NTT fields. The 1.1mm Lockman Hole field was observed as part of the SHADES survey which meant that there was a catalogue of $850\mu\text{m}$ sources available.

With this catalogue I found the flux at the positions of the SCUBA objects in the 1.1mm image. I then calculated the 1.1mm to $850\mu\text{m}$ flux ratios and compared them to the 1.2mm to $850\mu\text{m}$. The data are visually similar and a two sided KS test suggests that there is a high probability they two populations agree. This however does not determine if these flux ratios are due to very high redshift sources. The data suggests that the less extreme flux ratios Eales et al. (2003) found are possibly correct although photometric redshifts for the LH data would suggest these objects are at medium redshifts.

6.4.2 Abell 2125 IRAC Observations

I tried a second approach to this problem using Spitzer infrared data. This was possible as follow up IRAC observations of the Abell 2125 field were undertaken as part of the investigation into the MAMBO survey data. I determined infrared counterparts to these objects using the radio positions reported in Eales et al. (2003). I then compared measurements of the magnitudes of these objects in the

IRAC bands with data from Dye et al. (2008), who observed SCUBA sources with IRAC and also determined photometric redshifts to their objects. A comparison of this data in the magnitude redshift plane suggests that these MAMBO objects are more likely to be located at what would be considered a normal area of the plane rather than at the much higher redshifts as suggested by Eales et al. (2003).

6.4.3 Unusual but not at Extreme Redshift

The data presented in chapter 4 then supports the result found in Eales et al. (2003) that some submillimetre galaxies have unusual ratios of 1.2mm and 1.1mm flux to $850\mu\text{m}$ flux and that these ratios are not due to measurement problems. My analysis, however, suggests that these ratios are probably due to differing dust properties rather than extreme redshifts.

6.5 CUDSS Identifications

In chapter 5 I used IRAC observations of the CUDSS 3 hour field to determine secure identifications for SCUBA objects detected as part of the survey. In this analysis I made use of a Monte-Carlo method to determine the probability that a given object in the IRAC images within $20''$ of a SCUBA object position was a chance coincidence. If the object with the lowest probability of being a chance coincidence had a probability less than the cut-off ($P < 0.1$) in at least the one IRAC band and was not a significant distance from the SCUBA position ($\lesssim 10''$) I considered it a secure identification. Those objects that did not fit these criteria I described as chance associations.

In all there are 12 secure identifications from the IRAC data. These identifications were then compared to optical and radio identifications carried out by C04 and it was determined that a significant number identified sources at similar locations. Six of the secure identifications from C04 are within $1''$ of a secure or suspect IRAC identification.

A photometric analysis was carried out using extra optical data. When compared to photometric redshift estimates in C04 an agreement was seen. The photometric estimates of the IRAC identifications agree within errors with 3 spectroscopic redshifts they obtained. This suggests that the photometric analysis was, at least in the case of those sources with detections in multiple bands, accurate. It is interesting to note however that when Webb et al. (2003a) estimated the redshifts to the SCUBA objects using the 1.4GhZ to $850\mu\text{m}$ flux ratio method they obtained much higher redshifts. The median being double that suggested by the data presented here and in C04. This possibly adds weight to the suggestion from chapter 4 that there may be a confounding factor affecting the flux from submillimetre galaxies. Although it has to be said that the flux ratio method has been shown to provide useful redshift estimates in the past.

I also carried out an identification analysis on a combined IRAC $3.6\mu\text{m}$ and $4.5\mu\text{m}$ catalogue using the ratio of those two fluxes to add another level to the analysis. If those objects that have low P values also had red colours they are more likely to be identifications of submillimetre galaxies. This is because submillimetre galaxies are often associated with extremely red objects. With this approach I securely identified 9. Four of these coincide with the previous identifications from the individual IRAC catalogues. Four of my secure identifications also coincide with those C04 identified.

This analysis showed that it is possible to find counterparts to submillimetre galaxies in Spitzer IRAC data. As I found a similar number of secure identifications when compared with Clements et al. (2004) using their data with optical, near-infrared and radio data it is not unreasonable to suggest that mid-infrared data is as effective at identifying submillimetre galaxies as radio and optical data.

6.6 A Complex Picture

These results present a complex picture of the submillimetre galaxy population. While the stacking analysis and the flux ratio investigation seem to agree with the general consensus. That is submillimetre galaxies can be found at high redshifts. The photometric redshifts I calculated for the CUDSS identifications seem to suggest there are also submillimetre galaxies at much lower redshifts. This result is supported by the photometric redshifts of other investigations of these CUDSS galaxies. These different results may be due to the limited numbers of galaxies in each survey or they could be due to the different methods probing different parts of the submillimetre galaxy population.

6.7 Future Work

6.7.1 1.1mm Flux Deboosting

In chapter 2 sources are extracted from the reduced 1.1mm AzTEC maps of the Lockman Hole field and the Subaru XMM-Newton Deep Field regions. The measurements of the flux of these sources are subject to flux boosting. This is the well

known phenomenon which causes an upward bias in the measured flux from sources in this portion of the electromagnetic spectrum. In order to fully account for this the data has to be *deboosted*. That is an estimate on the fraction of the measured flux from the source that is due to positive noise in the map has to be produced.

This procedure was performed by AU10 in their analysis of the two fields and so deboosting the fluxes found in chapter 2 for the detected sources would provide another direct comparison between the catalogue in this thesis and that produced by AU10. The estimated level of boosting in the different reductions would also be useful for comparison.

6.7.2 Sample Size

While the numbers of detected submillimetre galaxies has been increasing steadily over the last decade the statistics of surveys are to an extent compromised by small number. It may be that the properties and characteristics of submillimetre galaxies that have been deduced from these studies are representative of the larger population. Although it is equally possible that this subset, which is largely the higher luminosity end of the population, are abnormal.

This uncertainty can really only be answered definitively with larger samples. The advent of the Herschel space telescope and the legacy surveys currently being observed by it will provide invaluable data to help resolve this problem especially if the early results are indicative of what can be expected.

6.7.3 IRAC Colour Analysis

In chapter 4 the possibility that some dusty submillimetre galaxies are at a substantially higher redshift than is commonly believed is investigated. As mentioned in that chapter 1 method that has been used to estimate the redshifts to faint galaxies is to analyse the position of the galaxy in an IRAC colour-colour plot. This could not be carried out using the data available in chapter 4 due to the problems in reducing the $5.8\mu\text{m}$ data. If the artefacts in the $5.8\mu\text{m}$ data were to be removed this would allow an additional redshift estimate to be found.

Bibliography

- Alexander, D. M., Bauer, F. E., Chapman, S. C., Smail, I., Blain, A. W., Brandt, W. N., & Ivison, R. J. 2005, *Astrophys. J.*, 632, 736
- Aretxaga, I., et al. 2007, *Mon. Not. R. Astr. Soc.*, 379, 1571
- Austermann, J. E., et al. 2010, *Mon. Not. R. Astr. Soc.*, 401, 160
- Baugh, C. M. 2006, *Reports on Progress in Physics*, 69, 3101
- Bertin, E., & Arnouts, S. 1996, *Astr. Astrophys. Suppl.*, 117, 393
- Bertoldi, F., Menten, K. M., Kreysa, E., Carilli, C. L., & Owen, F. 2002, *Highlights of Astronomy*, 12, 473
- Blain, A. W., & Longair, M. S. 1993, *Mon. Not. R. Astr. Soc.*, 264, 509
- Blain, A. W., Smail, I., Ivison, R. J., Kneib, J., & Frayer, D. T. 2002, *Phys. Rept.*, 369, 111
- Blanton, M. R., et al. 2005, *Astron. J.*, 129, 2562
- Bogges, N. W., et al. 1992, *Astrophys. J.*, 397, 420
- Bolzonella, M., Miralles, J.-M., & Pelló, R. 2000, *Astron. Astrophys.*, 363, 476
- Brodwin, M., Lilly, S. J., Porciani, C., McCracken, H. J., Le Fèvre, O., Foucaud, S., Crampton, D., & Mellier, Y. 2006, *Astrophys. J. Suppl.*, 162, 20

- Carilli, C. L., & Yun, M. S. 1999, *Astrophys. J. Letters*, 513, L13
- Chapman, S. C., Blain, A. W., Ivison, R. J., & Smail, I. R. 2003, *Nature*, 422, 695
- Chapman, S. C., Blain, A. W., Smail, I., & Ivison, R. J. 2005, *Astrophys. J.*, 622, 772
- Chapman, S. C., Smail, I., Windhorst, R., Muxlow, T., & Ivison, R. J. 2004, *The Astrophysical Journal*, 611, 732
- Clements, D., et al. 2004, *Mon. Not. R. Astr. Soc.*, 351, 447
- Clements, D. L., et al. 2008, *Mon. Not. R. Astr. Soc.*, 387, 247
- Colless, M. 1999, in *Large-Scale Structure in the Universe*, ed. G. Efstathiou & et al., 105–116
- Condon, J. J., Anderson, M. L., & Helou, G. 1991, *Astrophys. J.*, 376, 95
- Conselice, C. J., Chapman, S. C., & Windhorst, R. A. 2003, *Astrophys. J. Letters*, 596, L5
- Coppin, K., Halpern, M., Scott, D., Borys, C., & Chapman, S. 2005, *Mon. Not. R. Astr. Soc.*, 357, 1022
- Coppin, K., et al. 2006, *Mon. Not. R. Astr. Soc.*, 372, 1621
- . 2008, *Mon. Not. R. Astr. Soc.*, 384, 1597
- Dole, H., et al. 2006, *Astron. Astrophys.*, 451, 417
- Downes, D., & Solomon, P. M. 1998, *Astrophys. J.*, 507, 615
- Duncan, W. D., Robson, E. I., Ade, P. A. R., Sandell, G., & Griffin, M. J. 1990, *Mon. Not. R. Astr. Soc.*, 243, 126

- Duncan, W. D., Robson, I., Ade, P. A. R., & Church, S. E. 1995, in *Astronomical Society of the Pacific Conference Series*, Vol. 75, *Multi-Feed Systems for Radio Telescopes*, ed. D. T. Emerson & J. M. Payne, 295–+
- Dunne, L., & Eales, S. A. 2001, *Mon. Not. R. Astr. Soc.*, 327, 697
- Dunne, L., Eales, S. A., & Edmunds, M. G. 2003, *Mon. Not. R. Astr. Soc.*, 341, 589
- Dunne, L., et al. 2010, Submitted MNRAS.
- Dye, S., Eales, S. A., Ashby, M. L. N., Huang, J.-S., Egami, E., Brodwin, M., Lilly, S., & Webb, T. 2007, *Mon. Not. R. Astr. Soc.*, 375, 725
- Dye, S., et al. 2006, *Astrophys. J.*, 644, 769
- . 2008, *Mon. Not. R. Astr. Soc.*, 386, 1107
- . 2009, *Astrophys. J.*, 703, 285
- Eales, S., Bertoldi, F., Ivison, R., Carilli, C., Dunne, L., & Owen, F. 2003, *Mon. Not. R. Astr. Soc.*, 344, 169
- Eales, S., Lilly, S., Gear, W., Dunne, L., Bond, J. R., Hammer, F., Le Fèvre, O., & Crampton, D. 1999, *Astrophys. J.*, 515, 518
- Eales, S., Lilly, S., Webb, T., Dunne, L., Gear, W., Clements, D., & Yun, M. 2000, *Astron. J.*, 120, 2244
- Eales, S., et al. 2009, *Astrophys. J.*, 707, 1779
- . 2010, *Publs. Astr. Soc. Pacif.*, 122, 499
- Eales, S. A., & Edmunds, M. G. 1996, *Mon. Not. R. Astr. Soc.*, 280, 1167

- F. Murtagh & A. Heck, ed. 1987, *Astrophysics and Space Science Library*, Vol. 131, *Multivariate Data Analysis*, ed. F. Murtagh & A. Heck
- Fazio, G. G., et al. 2004, *Astrophys. J. Suppl.*, 154, 10
- Fixsen, D. J., Dwek, E., Mather, J. C., Bennett, C. L., & Shafer, R. A. 1998, *Astrophys. J.*, 508, 123
- Gilbank, D. G., Smail, I., Ivison, R. J., & Packham, C. 2003, *Mon. Not. R. Astr. Soc.*, 346, 1125
- Gordon, K. D., et al. 2005, *Publs. Astr. Soc. Pacif.*, 117, 503
- Hammer, F., Crampton, D., Le Fevre, O., & Lilly, S. J. 1995, *Astrophys. J.*, 455, 88
- Hauser, M. G., et al. 1998, *Astrophys. J.*, 508, 25
- Hill, M. D., & Shanks, T. 2010, *Mon. Not. R. Astr. Soc.*, 1506
- Hogg, D. W. 2001, *Astron. J.*, 121, 1207
- Holland, W. S., et al. 1999, *Mon. Not. R. Astr. Soc.*, 303, 659
- Hughes, D. H., et al. 1998, *Nature*, 394, 241
- Ivison, R. J., et al. 2002, *Mon. Not. R. Astr. Soc.*, 337, 1
- . 2007, *Mon. Not. R. Astr. Soc.*, 380, 199
- James, A., Dunne, L., Eales, S., & Edmunds, M. G. 2002, *Mon. Not. R. Astr. Soc.*, 335, 753
- Jenness, T., & Lightfoot, J. 1997, *Starlink User Note*, 216

- Kaercher, H. J., & Baars, J. W. 2000, in Society of Photo-Optical Instrumentation Engineers (SPIE) Conference Series, Vol. 4015, Society of Photo-Optical Instrumentation Engineers (SPIE) Conference Series, ed. H. R. Butcher, 155–168
- Kreysa, E., et al. 1998, in Society of Photo-Optical Instrumentation Engineers (SPIE) Conference Series, Vol. 3357, Society of Photo-Optical Instrumentation Engineers (SPIE) Conference Series, ed. T. G. Phillips, 319–325
- Laurent, G. T., et al. 2005, *Astrophys. J.*, 623, 742
- Lilly, S. J., Eales, S. A., Gear, W. K. P., Hammer, F., Le Fèvre, O., Crampton, D., Bond, J. R., & Dunne, L. 1999, *Astrophys. J.*, 518, 641
- Makovoz, D., & Khan, I. 2005, in Astronomical Society of the Pacific Conference Series, Vol. 347, Astronomical Data Analysis Software and Systems XIV, ed. P. Shopbell, M. Britton, & R. Ebert, 81
- Mancone, C. L., Gonzalez, A. H., Brodwin, M., Stanford, S. A., Eisenhardt, P. R. M., Stern, D., & Jones, C. 2010, *Astrophys. J.*, 720, 284
- Mather, J. C., Fixsen, D. J., & Shafer, R. A. 1993, in Society of Photo-Optical Instrumentation Engineers (SPIE) Conference Series, Vol. 2019, Society of Photo-Optical Instrumentation Engineers (SPIE) Conference Series, ed. M. S. Scholl, 168–179
- Mauskopf, P. D., Bock, J. J., Castillo, H. D., Holzapfel, W. L., & Lange, A. E. 1997, *Appl. Opt.*, 36, 765
- McCracken, H. J., Le Fèvre, O., Brodwin, M., Foucaud, S., Lilly, S. J., Crampton, D., & Mellier, Y. 2001, *Astron. Astrophys.*, 376, 756
- Mortier, A. M. J., et al. 2005, *Mon. Not. R. Astr. Soc.*, 363, 563

- Naylor, D. A., Davis, G. R., Gom, B. G., Clark, T. A., & Griffin, M. J. 2000, *Mon. Not. R. Astr. Soc.*, 315, 622
- Pascale, E., et al. 2009, *Astrophys. J.*, 707, 1740
- Peacock, J. A., et al. 2000, *Mon. Not. R. Astr. Soc.*, 318, 535
- Perera, T. A., et al. 2008, *Mon. Not. R. Astr. Soc.*, 391, 1227
- Pilbratt, G. L., et al. 2010, *Astron. Astrophys.*, 518, L1+
- Pope, A., et al. 2006, *Mon. Not. R. Astr. Soc.*, 370, 1185
- Puget, J., Abergel, A., Bernard, J., Boulanger, F., Burton, W. B., Desert, F., & Hartmann, D. 1996, *Astron. Astrophys.*, 308, L5+
- Rengarajan, T. N., & Takeuchi, T. T. 2001, *Publ. Astron. Soc. Japan*, 53, 433
- Rieke, G. H., et al. 2004, *Astrophys. J. Suppl.*, 154, 25
- Scott, K. S., et al. 2008, *Mon. Not. R. Astr. Soc.*, 385, 2225
- Scott, S. E., et al. 2002, *Mon. Not. R. Astr. Soc.*, 331, 817
- Scoville, N., et al. 2007, *Astrophys. J. Suppl.*, 172, 1
- Serjeant, S., et al. 2004, *Astrophys. J. Suppl.*, 154, 118
- . 2008, *Mon. Not. R. Astr. Soc.*, 386, 1907
- Silverberg, R. F., Hauser, M. G., Boggess, N. W., Kelsall, T. J., Moseley, S. H., & Murdock, T. L. 1993, in *Society of Photo-Optical Instrumentation Engineers (SPIE) Conference Series*, Vol. 2019, Society of Photo-Optical Instrumentation Engineers (SPIE) Conference Series, ed. M. S. Scholl, 180–189
- Smail, I., Ivison, R. J., & Blain, A. W. 1997, *Astrophys. J. Letters*, 490, L5+

- Smail, I., Ivison, R. J., Owen, F. N., Blain, A. W., & Kneib, J. 2000, *Astrophys. J.*, 528, 612
- Springel, V., et al. 2005, *Nature*, 435, 629
- Sunyaev, R. A., & Zeldovich, I. B. 1980, *Ann. Rev. Astron. Astrophys.*, 18, 537
- Swinbank, A. M., Chapman, S. C., Smail, I., Lindner, C., Borys, C., Blain, A. W., Ivison, R. J., & Lewis, G. F. 2006, *Mon. Not. R. Astr. Soc.*, 371, 465
- Takagi, T., et al. 2007, *Mon. Not. R. Astr. Soc.*, 381, 1154
- Thomas, D., Maraston, C., Bender, R., & Mendes de Oliveira, C. 2005, *Astrophys. J.*, 621, 673
- van der Kruit, P. C. 1971, *Astron. Astrophys.*, 15, 110
- Vlahakis, C., Dunne, L., & Eales, S. 2005, *Mon. Not. R. Astr. Soc.*, 364, 1253
- Wardlow, J. L., et al. 2010, Submitted MNRAS.
- Waskett, T. J., et al. 2003, *Mon. Not. R. Astr. Soc.*, 341, 1217
- Webb, T. M., et al. 2003a, *Astrophys. J.*, 587, 41
- . 2003b, *Astrophys. J.*, 582, 6
- Webb, T. M. A., Lilly, S. J., Clements, D. L., Eales, S., Yun, M., Brodwin, M., Dunne, L., & Gear, W. K. 2003c, *Astrophys. J.*, 597, 680
- Wilson, G. W., et al. 2008, *Mon. Not. R. Astr. Soc.*, 386, 807
- Wright, E. L. 2006, *Publs. Astr. Soc. Pacif.*, 118, 1711
- Younger, J. D., et al. 2007, *Astrophys. J.*, 671, 1531